Imaging and 3D reconstruction of membrane protein complexes by cryo-electron microscopy and single particle analysis

Inauguraldissertation

zur

Erlangung der Würde eines Doktors der Philosophie

vorgelegt der

Philosophisch-Naturwissenschaftlichen Fakultät

der Universität Basel

von

Marco Gregorini

aus

Mesocco GR

Basel, 2006

Genehmigt von der Philosophisch-Naturwissenschaftlichen Fakultät

auf Antrag von

Prof. Dr. Andreas Engel & Prof. Dr. Nicolas Boisset

Basel, 2. Mai 2006

Prof. Dr. Hans-Jakob Wirz

Dekan

Abstract

Cryo-electron microscopy (cryo-EM) in combination with single particle image processing and volume reconstruction is a powerful technology to obtain medium-resolution structures of large protein complexes, which are extremely difficult to crystallize and not amenable to NMR studies due to size limitation. Depending on the stability and stiffness as well as on the symmetry of the complex, three-dimensional reconstructions at a resolution of 10-30 Å can be achieved. In this range of resolution, we may not be able to answer chemical questions at the level of atomic interactions, but we can gain detailed insight into the macromolecular architecture of large multi-subunit complexes and their mechanisms of action. In this thesis, several prevalently large membrane protein complexes of great physiological importance were examined by various electron microscopy techniques and single particle image analysis. The core part of my work consists in the imaging of a mammalian V-ATPase, frozen-hydrated in amorphous ice and of the completion of the first volume reconstruction of this type of enzyme, derived from cryo-EM images. This ubiquitous rotary motor is essential in every eukaryotic cell and is of high medical importance due to its implication in various diseases such as osteoporosis, skeletal cancer and kidney disorders. My contribution to the second and third paper concerns the volume reconstruction of two bacterial outer membrane pore complexes from cryo-EM images recorded by my colleague Mohamed Chami. PulD from *Klebsiella oxytoca* constitutes a massive translocating pore capable of transporting a fully folded cell surface protein PulA through the membrane. It is part of the Type II secretion system, which is common for Gram-negative bacteria. The second volume regards ClyA, a pore-forming heamolytic toxin of virulent *Escherichia coli* and *Salmonella enterica* strains that kill target cells by inserting pores into their membranes. To the last two papers, I contributed with cryo-negative stain imaging of the cell division protein DivIVA from *Bacillus subtilis* and with image processing of the micrographs displaying the siderophore receptor FrpB from *Neisseria meningitidis*.

Acknowledgements

I would like to thank my advisor Andreas Engel for his great help and support throughout my PhD and, last but not least, for facilitating my 'sabbatical' in La Jolla in the first year of my thesis. I'm also thankful to Ron Milligan and Geoffrey Chang for hosting me in their labs during my exchange year and for their great support during this time.

I would further like to thank Kitaru Suda for his continous great help in the wet-lab and for sharing his wisdom and huge experience with me. Thanks a lot also to Mohamed Chami and Hervé Rémigy for enlightening discussions and the good team work on several projects.

I am thankful to Nora Eifler, Wanda Kukulski, Thomas Kaufmann, Myriam Duckely, Paul Werten, Andreas Schenk and Ansgar Philippsen for their help with various wet-lab and computer issues and to all the members of the Engel group for their friendship and for contributing to the good working atmosphere in the lab.

Thanks also to the SPIDER cracks Nicolas Boisset and Michael Radermacher for their precious hints and advices concerning single particle processing.

During this thesis work I had the pleasure to collaborate with some great research groups: thanks to Xiao-Song Xie, Helmut Wieczorek, Tony Pugsley, Rudi Glockshuber, Henning Stahlberg, Imrich Barák, Jan Tommassen and the members of their teams.

A very special thank goes to my parents and to Teba for their huge support throughout the ups and downs that come along with a PhD, for cheering me up and always being there for me.

Table of Contents

List of Figures

List of Tables

Chapter 1

Introduction

1.1 The post-genomic era: structural proteomics

The publication of the sequencing of the human genome (Lander et al., 2001; Venter et al., 2001) represents a milestone in the process of understanding the architecture of life at the molecular level. This relatively concise code of three billion base pairs contains all the information nature requires for the genesis of a human being. Research in the field of genomics provided the blueprint for the understanding of synthesis and function of the entirety of the human proteins, the proteome. However, this great wealth of fundamental information did not have a major impact on facilitating drug discovery and development. In this sense, the genetic code remains yet uninterpretable. The reason appears obvious: proteins are the targets of virtually every conventional drug, and from genomic data it is impossible to draw conclusions about the mechanism of action of gene products, since post-translational modifications as well as interactions of the proteins with each other often influence their activity. Based on this awareness, the emerging field of structural proteomics attempts to complement the genomic information to allow interpretation of sequence-structure and structure-function relationship for the entire proteome of humans and of every organism of medical interest, e.g. pathogenic micro-organisms. The main efforts encompass extensive development of methods for high-throughput protein profiling, identification of drug targets, large-scale protein production and determination of the three-dimensional structure. Structural information at atomic resolution is the basis for rational and efficient drug development, since it allows for detailed understanding of the function of the target protein, including protein-protein and protein-ligand interactions. To date, the sole reliable approaches for structure determination are experimental and consist of NMR spectroscopy, x-ray crystallography and electron crystallography for atomic coordinates mainly of small proteins, as well as single particle analysis for medium-resolution volumes of large complexes. Computational structure modeling is an emerging discipline with considerable potential as computational power increases exponentially. However, specificly *ab initio* modeling and threading procedures produce results that are currently far from being accurate and reliable enough to be conclusive for industrial applications, e.g. drug development. Comparative or homology modeling is more advanced and the technology has the potential to be highly complementary to the experimental methods. Yet, today comparative modeling is still insufficiently accurate for many applications and most importantly, it requires templates of high sequence homology (ideally $> 30\%$), which in turn can only be generated by experimental structure identification.

1.2 Experimental methods for protein structure determination

1.2.1 Multi-dimensional nuclear magnetic resonance (NMR)

Multi-dimensional NMR is a rapidly progressing method that does not require protein crystallization and can be applied for three-dimensional structure determination and for investigation of dynamic features of small proteins in solution. The fraction of atomic structures contributed by solution NMR makes up for nearly 15% of the total entries to the Research Collaboratory for Structural Bioinfomatics (RCSB) protein data bank (PDB) (http://www.pdb.org, February 2006). Until re-

cently, the major limitation of correlation spectroscopy (COSY) has been the size of the protein. Conventionally recorded NMR spectra of proteins larger than 30-40 kDa showed a significantly reduced sensitivity and resolution due to the lower-frequency Brownian motion of large molecules, resulting in rapid loss of magnetization by transverse nuclear spin relaxation. In recent years, the use of stronger magnetic fields (21.1 Tesla, corresponding to a resonance frequency of 900 MHz), as well as the development of new technologies such as transverse relaxation-optimized spectroscopy (TROSY) (Pervushin et al., 1997) in conjunction with extensive deuterium labeling (Pervushin et al., 1997) and cross-correlated relaxation-enhanced polarization transfer (CRINEPT) (Riek et al., 1999) have allowed structural investigations of much larger proteins exceeding 100-150 kDa (Fernandez and Wüthrich, 2003; Riek et al., 2000). TROSY largely suppresses transverse relaxation and its introduction led to a gain in sensitivity and resolution of NMR spectra by a factor of 20-50 (Riek et al., 2000). This considerable shift in size limitation was particularly important for membrane proteins, since they have to be kept in solution in detergent micelles, which add a mass of 30-60 kDa to the protein. Examples of membrane proteins solved by solution NMR spectroscopy are the outer membrane proteins OmpA (Arora et al., 2001) and OmpX (Fernandez et al., 2004), and the outer membrane palimitoyl transferease PagP (Ahn et al., 2004) of *Escherichia coli*. The vast majority of solution NMR structures, however, concerns small soluble proteins.

1.2.2 X-ray crystallography

X-ray crystallography provided the first three-dimensional structure of a protein, the sperm whale myoglobin (Kendrew et al., 1958). Until today, it has been by far the most successful method for protein structure determination. 29800 or about 84.5% of the entirety of known structures registered in the RCSB protein data bank (http://www.pdb.org, February 2006) were solved by this technique. The field achieved formidable progresses in the recent years, which decisively contributed to this veritable explosion of PDB entries. Some of the primary advances were the use of high intensity light sources with a broad spectrum of x-ray wavelengths and cryo-cooling (Hope, 1988) of the crystals at liquid nitrogen temperature, which significantly increases crystal stability. Tunable wavelengths and the possibility of longer exposure times led to the introduction of multi-wavelength anomalous diffraction (MAD) (Hendrickson, 1985; Karle, 1980), which is today commonly used for the phasing of biological crystals. The major constraint for large-scale structure determination is, however, still the growth of well-diffracting crystals. To overcome this difficulty, industry and academic institutions undertake major efforts for the development of robotic high-throughput crystallization, the miniaturization of the experimental setups and the automation of crystal screening. Automated crystallization procedures will lead to an exponentially increasing amount of data, and future initiatives aim at the use of data mining and machine learning algorithms in order to develop predictive models for crystallization. This is a non-trivial challenge since the thermodynamic and kinetic processes involved in crystal nucleation and growth are extremely complex and poorly understood. Unfortunately, membrane proteins still make up for a very small fraction of the known atomic structures. Their functional and large-scale production and crystallization is considerably more difficult compared to soluble proteins. Since membrane proteins are kept in detergent solution, the protein-micelle complexes have to be accommodated in the crystal lattice. A problem thereby is, that most integral membrane proteins contain only small hydrophilic portions, which are crucial for crystal contact formation. The polar residues of the detergent micelles also contribute to contact formation but do not provide rigid contact surfaces leading to well-ordered crystals. Successful new methods to overcome the difficulties of membrane protein crystallization consist in the extension of hydrophilic areas by antibody fragment co-crystallization (Ostermeier et al., 1995) and in the use of lipidic cubic phase crystallization (Landau and Rosenbusch, 1996). Some of the most prominent examples of membrane protein structures solved by x-ray crystallography include the bacterial photosynthetic reaction center (Deisenhofer et al., 1984), the ATP synthase from yeast mitochondria (Stock et al., 1999), the rotor of the bacterial V-ATPase (Murata et al., 2005), the calcium ATPase from sarcoplasmatic reticulum (Toyoshima et al., 2000), the bovine G-protein coupled receptor rhodopsin (Palczewski et al., 2000), several potassium channels (Doyle et al., 1998;

Jiang et al., 2003), chloride channels (Dutzler et al., 2002) and ABC transporters (Chang and Roth, 2001; Locher et al., 2002).

1.2.3 Electron crystallography

Electron crystallography is an alternative method for three-dimensional protein structure determination, which is mainly applicable to trans-membrane proteins. In contrast to x-ray crystallography, the crystals required for this technique consist of two-dimensional arrays of membrane proteins embedded in a lipid bilayer. The principal difficulties, similarly to x-ray crystallography, include the production of sufficient protein quantities and the requirement for highly ordered crystalline arrays. A major advantage of electron crystallography, however, consists in the replacement of the detergent, used to keep the membrane protein in solution, by phospholipid molecules. In this manner, the physiological environment is optimally mimicked, and full activity of the membrane protein is granted. Suitable methods for the imaging of two-dimensional crystals are quick-freezing in a vitrifying water layer (Dubochet et al., 1988) and freeze-drying in sugar solution (Hirai et al., 1999). Due to the considerable sensitivity of the biological material, high quality images and diffraction data have to be recorded at low electron doses. High-resolution images are taken at doses of below 5 electrons/Å^2 at liquid nitrogen temperature (104K) (Conway et al., 1993) or at doses of below 20 electrons/Å^2 at liquid helium temperature (4.3 K) (Fujiyoshi, 1998) and require the use of microscopes equipped with a field emission gun producing a highly coherent electron beam. Electron micrographs have an inherently low signal-to-noise ratio and the information has to be extracted and enhanced by image averaging procedures. Electron crystallography allows for the combination of results from image processing, containing valuable phase information, with high-resolution diffraction data, in order to optimally exploit the structural information provided by the elastically scattered electrons. The method has been successfully applied for the elicitation of the atomic structures of bacteriorhodopsin (Grigorieff et al., 1996; Henderson et al., 1990; Kimura et al., 1997), the plant light harvesting complex (Kühlbrandt et al., 1994), several aquaporins (Gonen et al., 2005; Gonen et al., 2004; Hiroaki et al., 2006; Murata et al., 2000) and the nicotinic acetyl choline receptor (Miyazawa et al., 2003; Unwin, 2005).

1.2.4 Single particle analysis

Cryo-electron microscopy in combination with single particle image analysis is a rapidly progressing technique, which is complementary to the high-resolution structural methods mentioned above. Large multi-subunit complexes are not suitable for NMR studies and very often oppose to any attempt of crystallization. Single particle methods allow to image protein complexes in their native conformation, quick-frozen in amorphous ice (Dubochet et al., 1988), and without any crystallization constraints. Moreover, molecules in different conformational states can be isolated on the image level and dynamical interactions can be monitored. Single particle analysis assumes the presence of multiple copies of identical molecules that have different spatial orientations. Due to the low signal-to-noise ratio of cryo-electron micrographs, the evaluation of the relative orientations of the particles represents a major difficulty, especially for a completely unknown structure. Valid approaches for the determination of the spatial relationship of the projections are the methods of random conical data collection (Radermacher et al., 1986) and common line search (Crowther, 1971). With the angles determined, the volume of a molecule can be reconstructed using mathematical principles formulated by Radon (Radon, 1917). Refinement of the first three-dimensional model is obtained by iterative cycles of projection matching alternating with volume reconstruction. In the last decade, methodical improvement and rapid growth of computational capacities led to the determination of numerous structures of large complexes at sub-nanometer resolution. Most high-resolution single particle volumes concern icosahedral virus particles (Böttcher et al., 1997; Conway et al., 1997; Zhou et al., 2000), since the effective signal-to-noise ratio is considerably higher than for asymmetric particles, due to their sixty-fold symmetry. Prominent examples of lower-symmetry reconstructions include the chaperone protein GroEL at 6 Å resolution (Ludtke et al., 2004), currently the highest resolution published for a single particle map, the transferrin-transferrin receptor complex, which represents the smallest sub-nanometer single particle structure with only 290 kDa (Cheng et al., 2004), as well as the completely asymmetric bacterial 70S

ribosome at 11.5 Å resolution (Gabashvili et al., 2000). A further milestone was the recent publication of the first sub-nanometer resolution volume of a membrane protein, the skeletal muscle Ca^{2+} release channel (Ludtke et al., 2005). The resolution of the published structures has improved from 30-40 Å fifteen years ago to sub-nanometer resolution in recent years, and future directions clearly aim at resolutions of below 4 Å, which permit tracing of the polypeptide backbone without the need for crystallization. Major efforts in the field regard the development of automated image acquisition, particle pickup and image processing methods, as well as the improvement of the fitting of x-ray structures into medium-resolution density maps.

1.3 Application to membrane proteins

Based on genome-wide sequence analyses, it has been estimated that 30-40% (depending on the sources) of all expressed gene products are membrane proteins, with the larger genomes containing higher percentages than the smaller ones. Biological membranes act as communicative interface between cells and their environment as well as between intracellular compartments. Thereby, membrane proteins are involved in a number of vital processes such as cell-cell signaling and interaction, triggering of intracellular signal cascades, anchoring of the cytoskeleton, and transport of ions and small molecules from one membrane compartment to another. Considering this pivotal role exhibited in many fundamental cellular functions, the high medical importance of membrane proteins is not surprising. It has been estimated that up to 70% of all the currently available drugs act on membrane proteins. G-protein coupled receptors (GPCRs), which are at the origin of diverse signaling cascades, represent the largest class of potential drug targets, but also ion channels and targets for antibacterial drugs are becoming increasingly important, especially in the face of emerging resistance to conventional antibiotics.

Membrane proteins are generally classified into two broad categories; integral and peripheral membrane proteins. Integral membrane proteins have one or several segments embedded in the hydrophobic interior of the lipid bilayer, whereas peripheral membrane proteins are bound to the bilayer via interactions with either integral membrane proteins or polar lipid groups. Insertion of the polar compounds of integral membrane proteins into the hydrophobic hydrocarbon core of the lipid bilayer is coupled to a high thermodynamic expense. To minimize this cost, a number of conditions have to be fulfilled; the residues spanning the hydrophobic core of the membrane have to have non-polar side chains and the hydrophilic CONH groups of the polypeptide backbone have to participate in hydrogen bonding. Therefore, opposite to the water-exposed regions of a protein, which can adopt various folds, the structural diversity of the membrane-spanning segments is restricted by the physical and chemical properties of the lipid bilayer. Indeed, the trans-membrane segments of all integral membrane proteins with known structure either consist of α-helices or of multiple β-sheets arranged to a β-barrel. Most of the membrane proteins with known structure, however, were found to have α-helical trans-membrane segments. In many cases, different classes of helical proteins exhibit particular, characteristic arrangements of the helices. An important family of α-helical proteins is defined by the presence of seven trans-membrane segments. Bacteriorhodopsin was the first representative of this family to be described (Henderson et al., 1990), but also many eukaryotic cell surface receptors, including GPCRs, are predicted to have such a seven trans-membrane helices motif. Another family of helical membrane proteins with high physiological importance is represented by the aquaporins. These tetrameric water channels inherently show a characteristic pattern of six trans-membrane helices in addition to two shorter helices for each subunit (Murata et al., 2000). The second fundamental structural motif, the β-barrel, is mainly found in bacterial outer membrane proteins. For example, porins consist of three identical copies of barrels, each composed of 16 β-sheets (Cowan et al., 1992).

Not only small membrane proteins, but also large molecular machines adhere to the structural restrictions introduced by the lipidic environment. A prominent example of an α-helical complex, is the V-ATPase of bovine brain, which was investigated in this thesis. The volume reconstruction indicates the presence of six rotor subunits and therefore 24 α-helices spanning the membrane, which is in the same range as found for the related ATP synthase (20-30 helices, depending on the species (Pogoryelov et al., 2005; Seelert et al., 2000; Stahlberg

et al., 2001; Stock et al., 1999)). Another large complex presented in this thesis, PulD, the outer membrane pore of the type II secretion system of *Klebsiella oxytoca*, is postulated to be a representative of the β-barrel proteins. Although in recent years formidable progresses were made in the field of membrane proteomics and many mysteries of membrane proteins were unveiled, the detailed mechanism of assembly and action of the majority of known membrane proteins is yet unclear. Coordinated efforts within a comprehensive structural proteomics network, including all the cell-biological, biochemical and structural techniques discussed in this introduction, will be necessary to gain a more profound insight into the function and dynamics of membrane proteins. The contribution of this thesis within the above mentioned network is focused on visualization, three-dimensional reconstruction and characterization of multi-subunit membrane protein assemblies.

1.4 References

Ahn, V.E., Lo, E.I., Engel, C.K., Chen, L., Hwang, P.M., Kay, L.E., Bishop, R.E. and Prive, G.G. (2004) A hydrocarbon ruler measures palmitate in the enzymatic acylation of endotoxin. Embo J, 23, 2931-2941.

Arora, A., Abildgaard, F., Bushweller, J.H. and Tamm, L.K. (2001) Structure of outer membrane protein A transmembrane domain by NMR spectroscopy. Nat Struct Biol, 8, 334-338.

Böttcher, B., Wynne, S.A. and Crowther, R.A. (1997) Determination of the fold of the core protein of hepatitis B virus by electron cryomicroscopy. Nature, 386, 88-91.

Chang, G. and Roth, C.B. (2001) Structure of MsbA from E. coli: a homolog of the multidrug resistance ATP binding cassette (ABC) transporters. Science, 293, 1793-1800.

Cheng, Y., Zak, O., Aisen, P., Harrison, S.C. and Walz, T. (2004) Structure of the human transferrin receptor-transferrin complex. Cell, 116, 565-576.

Conway, J.F., Cheng, N., Zlotnick, A., Wingfield, P.T., Stahl, S.J. and Steven, A.C. (1997) Visualization of a 4-helix bundle in the hepatitis B virus capsid by cryo-electron microscopy. Nature, 386, 91-94.

Conway, J.F., Trus, B.L., Booy, F.P., Newcomb, W.W., Brown, J.C. and Steven, A.C. (1993) The effects of radiation damage on the structure of frozen hydrated HSV-1 capsids. J Struct Biol, 111, 222-233.

Cowan, S.W., Schirmer, T., Rummel, G., Steiert, M., Ghosh, R., Pauptit, R.A., Jansonius, J.N. and Rosenbusch, J.P. (1992) Crystal structures explain functional properties of two E. coli porins. Nature, 358, 727-733.

Crowther, R.A. (1971) Procedures for three-dimensional reconstruction of spherical viruses by Fourier synthesis from electron micrographs. Philos Trans R Soc Lond B Biol Sci, 261, 221-230.

Deisenhofer, J., Epp, O., Miki, K., Huber, R. and Michel, H. (1984) X-ray structure analysis of a membrane protein complex. Electron density map at 3 Å resolution and a model of the chromophores of the photosynthetic reaction center from Rhodopseudomonas viridis. J Mol Biol, 180, 385-398.

Doyle, D.A., Morais Cabral, J., Pfuetzner, R.A., Kuo, A., Gulbis, J.M., Cohen, S.L., Chait, B.T. and MacKinnon, R. (1998) The structure of the potassium channel: molecular basis of K^+ conduction and selectivity. Science, 280, 69-77.

Dubochet, J., Adrian, M., Chang, J.J., Homo, J.C., Lepault, J., McDowall, A.W. and Schultz, P. (1988) Cryo-electron microscopy of vitrified specimens. Q Rev Biophys, 21, 129-228.

Dutzler, R., Campbell, E.B., Cadene, M., Chait, B.T. and MacKinnon, R. (2002) X-ray structure of a ClC chloride channel at 3.0 Å reveals the molecular basis of anion selectivity. Nature, 415, 287-294.

Fernandez, C., Hilty, C., Wider, G., Guntert, P. and Wüthrich, K. (2004) NMR structure of the integral membrane protein OmpX. J Mol Biol, 336, 1211-1221.

Fernandez, C. and Wüthrich, K. (2003) NMR solution structure determination of membrane proteins reconstituted in detergent micelles. FEBS Lett, 555, 144-150.

Fujiyoshi, Y. (1998) The structural study of membrane proteins by electron crystallography. Adv Biophys, 35, 25-80.

Gabashvili, I.S., Agrawal, R.K., Spahn, C.M., Grassucci, R.A., Svergun, D.I., Frank, J. and Penczek, P. (2000) Solution structure of the *E. coli* 70S ribosome at 11.5 A resolution. Cell, 100, 537-549.

Gonen, T., Cheng, Y., Sliz, P., Hiroaki, Y., Fujiyoshi, Y., Harrison, S.C. and Walz, T. (2005) Lipid-protein interactions in double-layered two-dimensional AQP0 crystals. Nature, 438, 633-638.

Gonen, T., Sliz, P., Kistler, J., Cheng, Y. and Walz, T. (2004) Aquaporin-0 membrane junctions reveal the structure of a closed water pore. Nature, 429, 193-197.

Grigorieff, N., Ceska, T.A., Downing, K.H., Baldwin, J.M. and Henderson, R. (1996) Electron-crystallographic refinement of the structure of bacteriorhodopsin. J Mol Biol, 259, 393-421.

Henderson, R., Baldwin, J.M., Ceska, T.A., Zemlin,

F., Beckmann, E. and Downing, K.H. (1990) Model for the structure of bacteriorhodopsin based on high-resolution electron cryo-microscopy. J Mol Biol, 213, 899-929.

Hendrickson, W.A. (1985) Analysis of Protein Structure from Diffraction Measurement at Multiple Wavelengths. Trans. ACA, 21.

Hirai, T., Murata, K., Mitsuoka, K., Kimura, Y. and Fujiyoshi, Y. (1999) Trehalose embedding technique for high-resolution electron crystallography: application to structural study on bacteriorhodopsin. J Electron Microsc (Tokyo), 48, 653-658.

Hiroaki, Y., Tani, K., Kamegawa, A., Gyobu, N., Nishikawa, K., Suzuki, H., Walz, T., Sasaki, S., Mitsuoka, K., Kimura, K., Mizoguchi, A. and Fujiyoshi, Y. (2006) Implications of the aquaporin-4 structure on array formation and cell adhesion. J Mol Biol, 355, 628-639.

Hope, H. (1988) Cryocrystallography of biological macromolecules: a generally applicable method. Acta Crystallogr B, 44 (Pt 1), 22-26.

Jiang, Y., Lee, A., Chen, J., Ruta, V., Cadene, M., Chait, B.T. and MacKinnon, R. (2003) X-ray structure of a voltage-dependent K^+ channel. Nature, 423, 33-41.

Karle, J. (1980) Some Developments in Anomalous Dispersion for the Structural Investigation of Macromolecular Systems in Biology. International Journal of Quantum Chemistry: Quantum Biology Symposium, 7, 357-367.

Kendrew, J.C., Bodo, G., Dintzis, H.M., Parrish, R.G., Wyckoff, H. and Phillips, D.C. (1958) A three-dimensional model of the myoglobin molecule obtained by x-ray analysis. Nature, 181, 662-666.

Kimura, Y., Vassylyev, D.G., Miyazawa, A., Kidera, A., Matsushima, M., Mitsuoka, K., Murata, K., Hirai, T. and Fujiyoshi, Y. (1997) Surface of bacteriorhodopsin revealed by high-resolution electron crystallography. Nature, 389, 206-211.

Kühlbrandt, W., Wang, D.N. and Fujiyoshi, Y. (1994) Atomic model of plant light-harvesting complex by electron crystallography. Nature, 367, 614-621.

Landau, E.M. and Rosenbusch, J.P. (1996) Lipidic cubic phases: a novel concept for the crystallization of membrane proteins. Proc Natl Acad Sci U S A, 93, 14532-14535.

Lander, E.S., Linton, L.M., Birren, B., Nusbaum, C., Zody, M.C., Baldwin, J., Devon, K., Dewar, K., Doyle, M., FitzHugh, W., Funke, R., Gage, D., Harris, K., Heaford, A., Howland, J., Kann, L., Lehoczky, J., LeVine, R., McEwan, P., McKernan, K., Meldrim, J., Mesirov, J.P., Miranda, C., Morris, W., Naylor, J., Raymond, C., Rosetti, M., Santos, R., Sheridan, A., Sougnez, C., Stange-Thomann, N., Stojanovic, N., Subramanian, A., Wyman, D., Rogers, J., Sulston, J., Ainscough, R., Beck, S., Bentley, D., Burton, J., Clee, C., Carter, N., Coulson, A., Deadman, R., Deloukas, P., Dunham, A., Dunham, I., Durbin, R., French, L., Grafham, D., Gregory, S., Hubbard, T., Humphray, S., Hunt, A., Jones, M., Lloyd, C., McMurray, A., Matthews, L., Mercer, S., Milne, S., Mullikin, J.C., Mungall, A., Plumb, R., Ross, M., Shownkeen, R., Sims, S., Waterston, R.H., Wilson, R.K., Hillier, L.W., McPherson, J.D., Marra, M.A., Mardis, E.R., Fulton, L.A., Chinwalla, A.T., Pepin, K.H., Gish, W.R., Chissoe, S.L., Wendl, M.C., Delehaunty, K.D., Miner, T.L., Delehaunty, A., Kramer, J.B., Cook, L.L., Fulton, R.S., Johnson, D.L., Minx, P.J., Clifton, S.W., Hawkins, T., Branscomb, E., Predki, P., Richardson, P., Wenning, S., Slezak, T., Doggett, N., Cheng, J.F., Olsen, A., Lucas, S., Elkin, C., Uberbacher, E., Frazier, M., Gibbs, R.A., Muzny, D.M., Scherer, S.E., Bouck, J.B., Sodergren, E.J., Worley, K.C., Rives, C.M., Gorrell, J.H., Metzker, M.L., Naylor, S.L., Kucherlapati, R.S., Nelson, D.L., Weinstock, G.M., Sakaki, Y., Fujiyama, A., Hattori, M., Yada, T., Toyoda, A., Itoh, T., Kawagoe, C., Watanabe, H., Totoki, Y., Taylor, T., Weissenbach, J., Heilig, R., Saurin, W., Artiguenave, F., Brottier, P., Bruls, T., Pelletier, E., Robert, C., Wincker, P., Smith, D.R., Doucette-Stamm, L., Rubenfield, M., Weinstock, K., Lee, H.M., Dubois, J., Rosenthal, A., Platzer, M., Nyakatura, G., Taudien, S., Rump, A., Yang, H., Yu, J., Wang, J., Huang, G., Gu, J., Hood, L., Rowen, L., Madan, A., Qin, S., Davis, R.W., Federspiel, N.A., Abola, A.P., Proctor, M.J., Myers, R.M., Schmutz, J., Dickson, M., Grimwood, J., Cox, D.R., Olson, M.V., Kaul, R., Shimizu, N., Kawasaki, K., Minoshima, S., Evans, G.A., Athanasiou, M., Schultz, R., Roe, B.A., Chen, F., Pan, H., Ramser, J., Lehrach, H., Reinhardt, R., McCombie, W.R., de la Bastide, M., Dedhia, N., Blocker, H., Hornischer, K., Nordsiek, G., Agarwala, R., Aravind, L., Bailey, J.A., Bateman, A., Batzoglou, S., Birney, E., Bork, P., Brown, D.G., Burge, C.B., Cerutti, L., Chen, H.C., Church, D., Clamp, M., Copley, R.R., Doerks, T., Eddy, S.R., Eichler, E.E., Furey, T.S., Galagan, J., Gilbert, J.G., Harmon, C., Hayashizaki, Y., Haussler, D., Hermjakob, H., Hokamp, K., Jang, W., Johnson, L.S., Jones, T.A., Kasif, S., Kaspryzk, A., Kennedy, S., Kent, W.J., Kitts, P., Koonin, E.V., Korf, I., Kulp, D., Lancet, D., Lowe, T.M., McLysaght, A., Mikkelsen, T., Moran, J.V., Mulder, N., Pollara, V.J., Ponting, C.P., Schuler, G., Schultz, J., Slater, G., Smit, A.F., Stupka, E., Szustakowski, J., Thierry-Mieg, D., Thierry-Mieg, J., Wagner, L., Wallis, J., Wheeler, R., Williams, A., Wolf, Y.I., Wolfe, K.H., Yang, S.P., Yeh, R.F., Collins, F., Guyer, M.S., Peterson, J., Felsenfeld, A., Wetterstrand, K.A., Patrinos, A., Morgan, M.J., de Jong, P., Catanese, J.J., Osoegawa, K., Shizuya, H., Choi, S. and Chen, Y.J. (2001) Initial sequencing and analysis of the human genome. Nature, 409, 860-921.

Locher, K.P., Lee, A.T. and Rees, D.C. (2002) The E. coli BtuCD structure: a framework for ABC transporter architecture and mechanism. Science, 296, 1091-1098.

Ludtke, S.J., Chen, D.H., Song, J.L., Chuang, D.T. and Chiu, W. (2004) Seeing GroEL at 6 A resolution by single particle electron cryomicroscopy. Structure, 12, 1129-1136.

Ludtke, S.J., Serysheva, II, Hamilton, S.L. and Chiu,

W. (2005) The pore structure of the closed RyR1 channel. Structure (Camb), 13, 1203-1211.

Miyazawa, A., Fujiyoshi, Y. and Unwin, N. (2003) Structure and gating mechanism of the acetylcholine receptor pore. Nature, 423, 949-955.

Murata, K., Mitsuoka, K., Hirai, T., Walz, T., Agre, P., Heymann, J.B., Engel, A. and Fujiyoshi, Y. (2000) Structural determinants of water permeation through aquaporin-1. Nature, 407, 599-605.

Murata, T., Yamato, I., Kakinuma, Y., Leslie, A.G. and Walker, J.E. (2005) Structure of the rotor of the V-Type Na^+-ATPase from Enterococcus hirae. Science, 308, 654-659.

Ostermeier, C., Iwata, S., Ludwig, B. and Michel, H. (1995) Fv fragment-mediated crystallization of the membrane protein bacterial cytochrome c oxidase. Nat Struct Biol, 2, 842-846.

Palczewski, K., Kumasaka, T., Hori, T., Behnke, C.A., Motoshima, H., Fox, B.A., Le Trong, I., Teller, D.C., Okada, T., Stenkamp, R.E., Yamamoto, M. and Miyano, M. (2000) Crystal structure of rhodopsin: A G protein-coupled receptor. Science, 289, 739-745.

Pervushin, K., Riek, R., Wider, G. and Wüthrich, K. (1997) Attenuated T2 relaxation by mutual cancellation of dipole-dipole coupling and chemical shift anisotropy indicates an avenue to NMR structures of very large biological macromolecules in solution. Proc Natl Acad Sci U S A, 94, 12366-12371.

Pogoryelov, D., Yu, J., Meier, T., Vonck, J., Dimroth, P. and Müller, D.J. (2005) The c15 ring of the *Spirulina platensis* F-ATP synthase: F1/F0 symmetry mismatch is not obligatory. EMBO Rep, 6, 1040-1044.

Radermacher, M., Wagenknecht, T., Verschoor, A. and Frank, J. (1986) A new 3D reconstruction scheme applied to the 50S ribosomal subunit of *E. coli*. J Microsc, 141 (Pt 1), RP1-2.

Radon, J. (1917) Über die Bestimmung von Funktionen durch ihre Integralwerte längs gewisser Mannigfaltigkeiten. Berichte über die Verhandlungen der königlich sächsischen Gesellschaft der Wissenschaften zu Leipzig. Math. Phys. Klasse, 69, 262-277.

Riek, R., Pervushin, K. and Wüthrich, K. (2000) TROSY and CRINEPT: NMR with large molecular and supramolecular structures in solution. Trends Biochem Sci, 25, 462-468.

Riek, R., Wider, G., Pervushin, K. and Wüthrich, K. (1999) Polarization transfer by cross-correlated relaxation in solution NMR with very large molecules. Proc Natl Acad Sci U S A, 96, 4918-4923.

Seelert, H., Poetsch, A., Dencher, N.A., Engel, A., Stahlberg, H. and Müller, D.J. (2000) Structural biology. Proton-powered turbine of a plant motor. Nature, 405, 418-419.

Stahlberg, H., Müller, D.J., Suda, K., Fotiadis, D., Engel, A., Meier, T., Matthey, U. and Dimroth, P. (2001) Bacterial Na^+-ATP synthase has an undecameric rotor. EMBO Rep, 2, 229-233.

Stock, D., Leslie, A.G. and Walker, J.E. (1999) Molecular architecture of the rotary motor in ATP synthase. Science, 286, 1700-1705.

Toyoshima, C., Nakasako, M., Nomura, H. and Ogawa, H. (2000) Crystal structure of the calcium pump of sarcoplasmic reticulum at 2.6 Å resolution. Nature, 405, 647-655.

Unwin, N. (2005) Refined structure of the nicotinic acetylcholine receptor at 4 Å resolution. J Mol Biol, 346, 967-989.

Venter, J.C., Adams, M.D., Myers, E.W., Li, P.W., Mural, R.J., Sutton, G.G., Smith, H.O., Yandell, M., Evans, C.A., Holt, R.A., Gocayne, J.D., Amanatides, P., Ballew, R.M., Huson, D.H., Wortman, J.R., Zhang, Q., Kodira, C.D., Zheng, X.H., Chen, L., Skupski, M., Subramanian, G., Thomas, P.D., Zhang, J., Gabor Miklos, G.L., Nelson, C., Broder, S., Clark, A.G., Nadeau, J., McKusick, V.A., Zinder, N., Levine, A.J., Roberts, R.J., Simon, M., Slayman, C., Hunkapiller, M., Bolanos, R., Delcher, A., Dew, I., Fasulo, D., Flanigan, M., Florea, L., Halpern, A., Hannenhalli, S., Kravitz, S., Levy, S., Mobarry, C., Reinert, K., Remington, K., Abu-Threideh, J., Beasley, E., Biddick, K., Bonazzi, V., Brandon, R., Cargill, M., Chandramouliswaran, I., Charlab, R., Chaturvedi, K., Deng, Z., Di Francesco, V., Dunn, P., Eilbeck, K., Evangelista, C., Gabrielian, A.E., Gan, W., Ge, W., Gong, F., Gu, Z., Guan, P., Heiman, T.J., Higgins, M.E., Ji, R.R., Ke, Z., Ketchum, K.A., Lai, Z., Lei, Y., Li, Z., Li, J., Liang, Y., Lin, X., Lu, F., Merkulov, G.V., Milshina, N., Moore, H.M., Naik, A.K., Narayan, V.A., Neelam, B., Nusskern, D., Rusch, D.B., Salzberg, S., Shao, W., Shue, B., Sun, J., Wang, Z., Wang, A., Wang, X., Wang, J., Wei, M., Wides, R., Xiao, C., Yan, C., Yao, A., Ye, J., Zhan, M., Zhang, W., Zhang, H., Zhao, Q., Zheng, L., Zhong, F., Zhong, W., Zhu, S., Zhao, S., Gilbert, D., Baumhueter, S., Spier, G., Carter, C., Cravchik, A., Woodage, T., Ali, F., An, H., Awe, A., Baldwin, D., Baden, H., Barnstead, M., Barrow, I., Beeson, K., Busam, D., Carver, A., Center, A., Cheng, M.L., Curry, L., Danaher, S., Davenport, L., Desilets, R., Dietz, S., Dodson, K., Doup, L., Ferriera, S., Garg, N., Gluecksmann, A., Hart, B., Haynes, J., Haynes, C., Heiner, C., Hladun, S., Hostin, D., Houck, J., Howland, T., Ibegwam, C., Johnson, J., Kalush, F., Kline, L., Koduru, S., Love, A., Mann, F., May, D., McCawley, S., McIntosh, T., McMullen, I., Moy, M., Moy, L., Murphy, B., Nelson, K., Pfannkoch, C., Pratts, E., Puri, V., Qureshi, H., Reardon, M., Rodriguez, R., Rogers, Y.H., Romblad, D., Ruhfel, B., Scott, R., Sitter, C., Smallwood, M., Stewart, E., Strong, R., Suh, E., Thomas, R., Tint, N.N., Tse, S., Vech, C., Wang, G., Wetter, J., Williams, S., Williams, M., Windsor, S., Winn-Deen, E., Wolfe, K., Zaveri, J., Zaveri, K., Abril, J.F., Guigo, R., Campbell, M.J., Sjolander, K.V.,

Karlak, B., Kejariwal, A., Mi, H., Lazareva, B., Hatton, T., Narechania, A., Diemer, K., Muruganujan, A., Guo, N., Sato, S., Bafna, V., Istrail, S., Lippert, R., Schwartz, R., Walenz, B., Yooseph, S., Allen, D., Basu, A., Baxendale, J., Blick, L., Caminha, M., Carnes-Stine, J., Caulk, P., Chiang, Y.H., Coyne, M., Dahlke, C., Mays, A., Dombroski, M., Donnelly, M., Ely, D., Esparham, S., Fosler, C., Gire, H., Glanowski, S., Glasser, K., Glodek, A., Gorokhov, M., Graham, K., Gropman, B., Harris, M., Heil, J., Henderson, S., Hoover, J., Jennings, D., Jordan, C., Jordan, J., Kasha, J., Kagan, L., Kraft, C., Levitsky, A., Lewis, M., Liu, X., Lopez, J., Ma, D., Majoros, W., McDaniel, J., Murphy, S., Newman, M., Nguyen, T., Nguyen, N., Nodell, M., Pan, S., Peck, J., Peterson, M., Rowe, W., Sanders, R., Scott, J., Simpson, M., Smith, T., Sprague, A., Stockwell, T., Turner, R., Venter, E., Wang, M., Wen, M., Wu, D., Wu, M., Xia, A., Zandieh, A. and Zhu, X. (2001) The sequence of the human genome. Science, 291, 1304-1351.

Zhou, Z.H., Dougherty, M., Jakana, J., He, J., Rixon, F.J. and Chiu, W. (2000) Seeing the herpesvirus capsid at 8.5 Å. Science, 288, 877-880.

Chapter 2

Three-dimensional reconstruction of bovine brain V-ATPase by cryo-electron microscopy and single particle analysis

Marco Gregorini[1,3], Jin Wang[2], Xiao-Song Xie[2], Ronald A. Milligan[3], Andreas Engel[1]

2.1 Abstract

Bovine V-ATPase from brain clathrin-coated vesicles was investigated by cryo-electron microscopy and single particle analysis. Our studies revealed great flexibility of the central linker region connecting V_1 and V_O. As a consequence, the two sub-complexes were processed separately and the resulting volumes were merged computationally. We present the first three-dimensional (3D) map of a V-ATPase obtained from cryo-electron micrographs. The overall resolution was estimated 34 Å by Fourier shell correlation (0.5 cutoff). Our 3D reconstruction shows a large peripheral stalk and a smaller, isolated peripheral density, suggesting a second, less well-resolved peripheral connection. The 3D map reveals new features of the large peripheral stator and of the collar-like density attached to the membrane domain. Our analyses of the membrane domain indicate the presence of six proteolipid subunits. In addition, we could localize the V_O subunit a flanking the large peripheral stalk.

Keywords: Bovine brain V-ATPase, cryo-electron microscopy, single particle analysis, 3D reconstruction

2.2 Introduction

V-ATPases are ubiquitous large protein complexes in the endo-membrane system of all eukaryotic cells and in the plasma membrane of specialized cells and of many bacteria. Eukaryotic V-ATPases are 900 kDa ATP-hydrolysis driven proton pumps involved in a number of acidification processes outside and inside the cell. In osteoclasts, V-ATPases acidify extracellular spaces for bone remodeling (Blair et al., 1989; Brown and Breton, 1996; Vaananen et al., 1990) while in kidney epithelial cells, they are responsible for urinary acidification (Brown and Breton, 1996; Steinmetz, 1986). V-ATPases are also believed to be crucial for normal sperm development in the male reproductive tract (Brown and Breton, 1996; Brown et al., 1992). Inside the cell, V-ATPases are involved in processes such as receptor-mediated endocytosis, intracellular trafficking, protein processing and degradation, uptake and storage of neurotransmitters (Crider and Xie, 2003; Inoue et al., 2003). Various intracellular compartments such as vacuoles, endosomes, lysosomes, chromaffin granules, clathrin-coated vesi-

[1]M.E.Müller Institute, Biozentrum, University of Basel, Klingelbergstrasse 50/70, CH-4056 Basel, Switzerland

[2]University of Texas Southwestern Medical Center at Dallas, Department of Internal Medicine, 6000 Harry Hines Boulevard, Dallas, TX 75390-8591 - USA

[3]The Scripps Research Institute, Department of Cell Biology, 10550 North Torrey Pines Road, La Jolla, CA 92037 - USA

cles and synaptic vesicles have large amounts of V-ATPases in their membranes. V-ATPases can also function as plasma membrane energizers by establishing and maintaining proton gradients across the membranes of insect cells (Wieczorek et al., 1999).

The eukaryotic V_1 domain is composed of the eight subunits A-H and has a proposed stoichiometry of $A_3B_3CDE_XFG_XH_X$ (X number of subunits controversial) (Arai et al., 1988; Müller and Grüber, 2003; Wilkens et al., 1999; Xu et al., 1999) comprising a mass of 640 kDa. The yeast V_O domain contains the five subunits a, c, c', c" and d that are arranged at a stoichiometry of $a(cc')_{4\text{-}5}c"d$ (Arai et al., 1988; Hirata et al., 1997; Wilkens et al., 1999) and has a mass of approximately 260 kDa. The exact number of c subunits is unclear. In mammalian V-ATPase, the c' isoform could not be demonstrated, but an additional V_O subunit Ac45 was characterized. ATP-hydrolysis takes place at and alternates between the three subunits A, which contain the catalytic sites (Feng and Forgac, 1992). This circular motion drives rotation of the presumably asymmetric central stalk that is firmly linked to the c-ring of V_O (Crider and Xie, 2003; Junge and Nelson, 2005). Protons are believed to be transported through the membrane at the interface of the c-ring and the stator subunit a (Junge and Nelson, 2005; Leng et al., 1996), which is connected to the A_3B_3 complex through a large peripheral stalk and possibly an additional peripheral connection. The number of stator connections of mammalian V-ATPase is controversial. In the case of the fungus *Neurospora crassa* (Venzke et al., 2005), two peripheral connectors were found, similarly to what was observed for the H^+ ATPase/synthase of the bacterium *Thermus thermophilus* (Bernal and Stock, 2004).

The structure of the bovine V-ATPase has been analyzed by biochemical techniques (Crider and Xie, 2003; Xie, 1996) and by electron microscopy of negatively stained samples (Wilkens and Forgac, 2001; Wilkens et al., 2004; Wilkens et al., 1999). A coarse picture of the molecular architecture of this rotary motor is now emerging but important features, especially the composition of the peripheral connection(s), are still subject of ongoing investigations.

Cryo-electron microscopy allows biological molecules to be imaged when immobilized by vitrification in their native conformation (Dubochet et al., 1988). In this study we report the first 3D reconstruction of a V-ATPase from images of frozen-hydrated complexes. In particular, we could resolve the large peripheral stator connection of the bovine V-ATPase, as well as a possible additional linker. Furthermore, hitherto unknown details of the contact area of the main peripheral connection with the collar-like structure, and of the architecture of the membrane domain are elucidated by our 3D reconstruction.

2.3 Results

2.3.1 Purification and functional characterization of bovine brain V-ATPase

Multi milligram quantities of V-ATPase were purified to near homogeneity (Figure 2.1A) as described previously (Xie and Stone, 1986). The larger subunits (V_1 subunits A - E and H, and V_O subunits a and d) are easily identified while the smaller subunits (V_1 subunits F, G1 and G2, and V_O subunit c) require higher concentration of SDS-PAGE (15%) for their resolution and identification (Xie, 1996). V_O subunits Ac45 and c" are poorly stained but their presence can be easily identified by Western blot (data not shown). The purified V-ATPase showed a specific Mg-ATPase activity of 14-16 μmoles P_i/(mg·min) and actively pumps protons when reconstituted into proteoliposomes (Figure 2.1B). The high functionality of the preparation indicates structural integrity.

2.3.2 Cryo-electron microscopy and 2D image processing

Cryo-electron microscopy was used to analyze the V-ATPase immobilized in vitrous ice. Intact molecules appear as asymmetric dumbbell-shaped particles (Figure 2.2A). In most cases the globular V_1 part is distinguishable from the flatter, cylindrical trans-membrane part. Between the two principal densities a narrow space is left free. In this space, attached to the membrane domain, a short elongated density is present. It is oriented perpendicularly to the long axis of the molecule. In addition, some particles show a thin density bridging the gap between the V_1 and V_O domain.

6496 V-ATPase particles were selected interactively for processing. Reference-free alignment procedures were unreliable due to the elongated shape

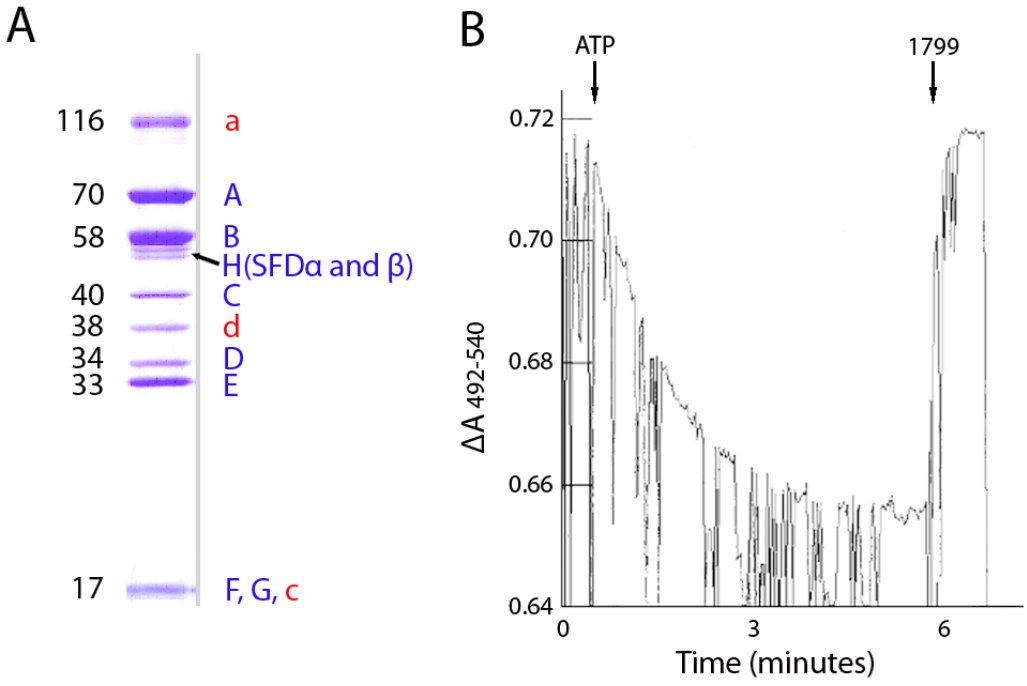

Figure 2.1: **Preparation and functional analysis of V-ATPase.** (A) The purified bovine brain V-ATPase (3 μg) was resolved by SDS-PAGE using a 12.5% gel and stained by Coomassie blue. (B) The proton translocation activity of the bovine brain V-ATPase was measured using acridine orange quenching method as described in the *Experimental procedures*. SFD Sub-Fifty eight Dimer, isoforms α and β.

of the particle and the low contrast and signal-to-noise ratio of the cryo-data. Therefore, class averages from reference-free aligned negative stain data (Figure 2.3A), were used as references for multi-reference alignment of the cryo-data set. Figures 2.2B1 (208 particles) and 2.2B2 (114 particles) show two characteristic class averages representing different orientations of the molecule on the carbon film. To select the fraction of particles exhibiting a straight central axis, a strict cross-correlation threshold was applied. The upper parts of Figures 2.2B1 and 2.2B2 display V_1. The expected hexameric ring of A_3B_3 subunits, here seen in side view, is poorly resolved. Possible reasons are the small number of particles and the sub-ideal alignment of the flexible holoenzymes. A prominent central cavity spans the V_1 domain from top to bottom (Figures 2.2B1 and 2.2B2). V_1 and V_O are connected through a thin density forming a central stalk parallel to the long axis of the molecule. Perpendicular to the central stalk an irregular, elongated density is attached to the membrane domain. A second, peripheral stalk, parallel to the central stalk, connects this density to the catalytic domain (Figure 2.2B2). The V_O complex exhibits an irregular elliptic shape with a density depression at the center. On the extra-cytosolic side of the membrane domain, a globular density (arrowhead Figure 2.2B2) is visible.

The flexibility of the connection between V_1 and V_O emerged as the principal cause for the limited resolution. Masked projections of a refined volume from negative stain data (see next section), calculated at various angles rotating around the long axis, were used for a refined multi-reference alignment of the cryo-images. Several averages of V_1 (Figure 2.2C) and V_O (Figure 2.2D), representing different orientations of the molecule, were calculated. The V_1 complex is resolved in more detail compared to Figure 2.2B. It consists of an asymmetric array of three (C3, C4, C5) or four (C1, C2) distinct lobes, consistent with the side view of a hexameric ring. At the center of the A_3B_3 complex, a longitudinal depression is visible, similarly to the observation made for the class averages of the holoenzyme. The thin density of the central stalk protrudes into the lower part of the abovementioned depression. In Figure 2.2C the large peripheral stalk is visible on the left (C1) and right (C5) side of the images, depending on the orientations of the molecule. Figure 2.2D shows a series of averages of the newly aligned V_O domain. The lower end of the peripheral stalk flank-

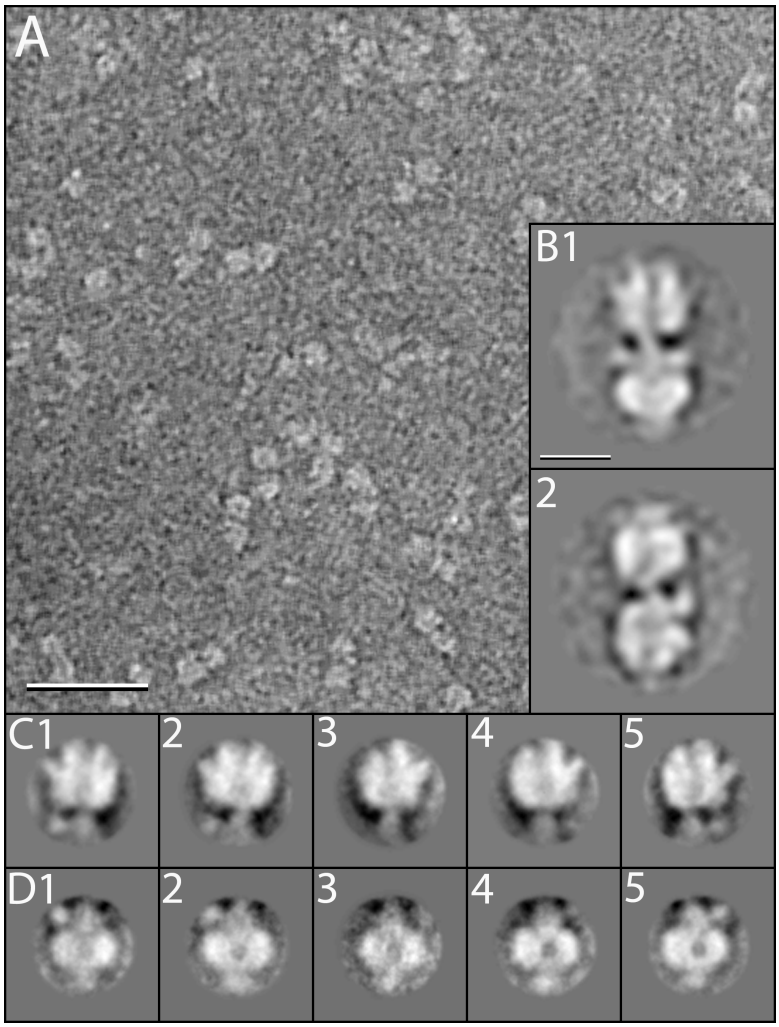

Figure 2.2: **Cryo-electron microscopy and 2D processing.** (A) Overview image of the V-ATPase preparation recorded in ice using a thin carbon support film. A median filter was applied for contrast enhancement. (B) Class averages of selected intact V-ATPase particles. The averages show two orientations represented by a relatively small number of straight particles (B1 208, B2 114). (C) Class average gallery from V_1 images aligned on projections of a negative stain V_1 volume rotated by 0, 30, 90, 120,150 degrees (standard deviation $\pm$ 10 degrees). Number of particles: C1 661, C2 277, C3 227, C4 476, C5 354. (D) Class average gallery from V_O images including the central domain, aligned on projections of a negative stain V_O volume rotated by 0, 30, 90, 120,150 degrees (standard deviation $\pm$ 10 degrees). Number of particles: D1 568, D2 361, D3 195, D4 709, D5 899. Scale bar (A) 500 Å, (B) 100 Å.

ing the central axle is present on the left (D1, D2) and right (D5) side, again depending on the absorption angle. The previously described elongated density perpendicular to the central stalk is rather blurred, compared to the averages in Figure 2.2B. At the bottom of the membrane domain a globular density is visible, while the central depression is still present.

2.3.3 Separate 3D reconstructions of V_1 and V_O

The considerable flexibility of the V-ATPase holoenzyme implied a separate processing of V_1 and V_O. In order to eventually allow a precise merging of the two 3D maps, selected areas of the collar-like structure between the two main densities were included into both partial maps redundantly. 6496 masked V_1 and V_O particles were used as raw data for the 3D processing. The V_1 reconstruction (Figure 2.4A) was calculated by matching the images to projections of a previously calculated negative stain model. In the iterative refinement particles with low cross-correlation values were removed. 2879 out of the initial 6496 particles were used for the refined structure presented in this study. The resolution was estimated 34 Å by Fourier shell correlation (0.5 cutoff, Supplementary Figure 2.7A). Surface repre-

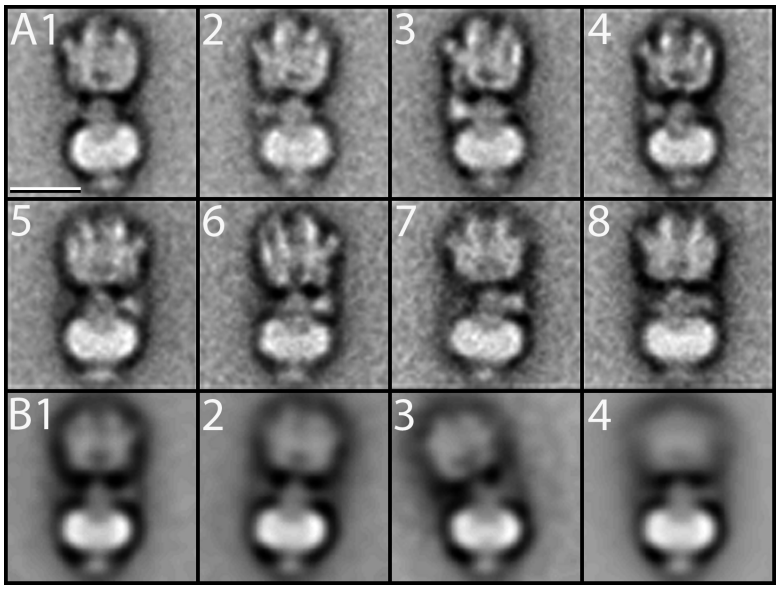

Figure 2.3: **Flexibility of the V-ATPase.** (A) Class averages from negatively stained particles exhibiting a straight central axis. The number of particles per class varies between 41 and 206. (B) Averages from negatively stained particles, aligned on a masked reference containing V_O and the central domain. Classification reveals different bending levels due to the flexibility of the central linker region of the molecule. Scale bar 100 Å.

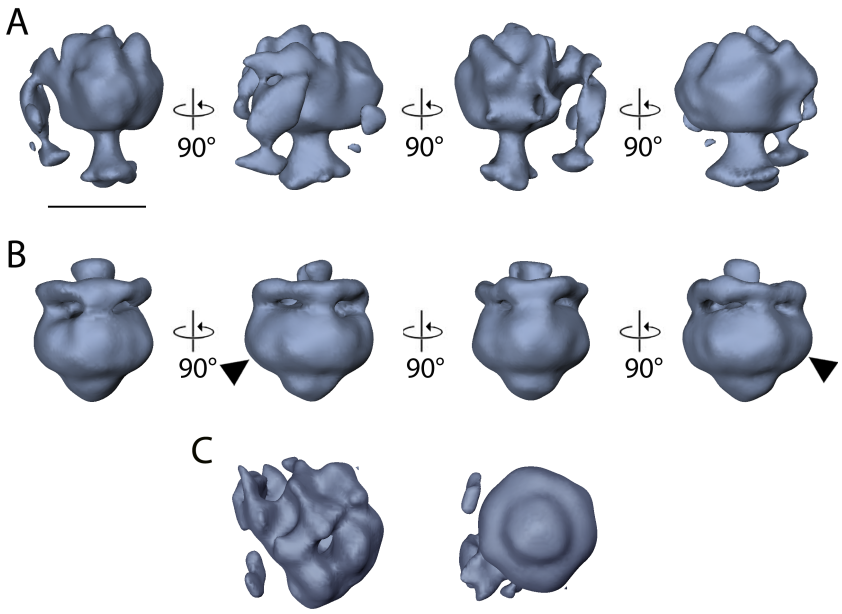

Figure 2.4: **3D reconstructions of V_1 and V_O.** (A) Surface representation of the 3D reconstruction of V_1, low-pass filtered at a resolution of 34 Å. (B) Surface representation of V_O including the collar-like structure surrounding the central stalk. The resolution was restricted to 31 Å. The arrowheads indicate the position of the lateral bulge. (C) Surface rendered top view of V_1 and bottom view of V_O, filtered at the respective resolution mentioned above. Scale bar 100 Å.

sentations of the maps of V_1 and V_O (presumably including the V_1 subunits C, D, F and H) were calculated to enclose a total mass of 640 kDa and 400 kDa respectively. The surfacing of the joint density was adjusted to match the surfacing of the individual reconstructions.

The A_3B_3 complex including a mass of roughly 375 kDa appears as flattened, asymmetric pseudo-hexagonal array with a height of 107 Å and a width of 106-141 Å (Figure 2.4A). The individual subunits of the hexagon are clearly distinguishable. At the bottom of the catalytic domain the elongated central stalk pokes out of the cavity at the interior of the A_3B_3 complex. The rod-shaped central stalk

spans a distance of 48 Å prior to widening in the region where it merges into the membrane domain. A prominent arm-like peripheral stalk, parallel to the central stalk, is attached to the A_3B_3 complex. The contact point of the peripheral connection is located laterally at one side of the A_3B_3 complex, at a distance of 15-20 Å. The length of the peripheral stalk is approximately 120 Å, and its volume comprises about 112'000 Å3. At the bottom of the stalk, where the contact with the collar-like structure has to occur, the density adopts a wider and flat shape.

The 3D map of V_O was obtained with the same strategy used for the V_1 reconstruction. The resulting volume presented in Figure 2.4B was calculated from 4547 individual particles. The resolution was estimated 31 Å by Fourier shell correlation (0.5 cut-off, Supplementary Figure 2.7B). Figure 2.4B displays the c-ring as a compact convex density with a diameter of about 120 Å. On one side of the ring a prominent peripheral bulge is present, giving the complex an elliptic appearance (arrowheads Figure 2.4B). The upper densities of the c-ring merge smoothly into a collar-like structure at the cytosolic side of the membrane. The diameter of this more subtle ring is 116 Å. Inside the collar, the truncated end of the central stalk is visible. On the extracytosolic side of the membrane domain, a globular density is tightly embedded in the pocket formed by the c-ring.

2.3.4 Merged V-ATPase reconstruction

The partial V_1 and V_O maps, low-pass filtered to a resolution of 34 Å and 31 Å respectively, were added to generate a 3D map of the intact V-ATPase (Figure 2.5A). The A_3B_3 complex, the upper part of the peripheral stalk, and the membrane domain are identical with the individual maps. However, there are slight differences in the central domains of the molecule where the two densities were joined together. Due to partial overlap of the added densities, the central stem appears more compact. At the contact point of the peripheral stalk with the membrane domain a terrace-like density completes the stator system (Figure 2.5A). In the side view the peripheral connection appears straighter compared to the partial map (Figure 2.4A), where it has a convex shape. In the partial map, at the bottom of the peripheral stalk, the density gets wider and points towards the central stalk. This is consistent with the terrace-like density observed in Figure 2.5A. A possible explanation for the straighter peripheral stalk in the joined reconstruction is that the peripheral tip of the terrace-like density was truncated by masking the V_1 particles, and that the stator was later complemented by adding the V_O map. Besides the large peripheral stalk, an additional peripheral density is present (Figure 2.5A). This isolated density is elongated and located at a similar distance from the central stalk. Compared to the individual V_1 map (Figure 2.4A), the density is larger, possibly due to the masking. In the top view (Figure 2.5D), the large peripheral stalk and the isolated peripheral density form an isosceles triangle with the central axis of the complex. The volumes of the central stalk and the isolated density are approximately 112'000 $Å^3$ and 14'300 $Å^3$ respectively.

Figures 2.5B-D show the interior of the 3D reconstruction. The six compact, elongated subunits of the A_3B_3 complex are arranged around the central cavity in an asymmetric fashion (Figures 2.5B2). The central stalk is massive between V_1 and V_O but does not fill the central cavity (Figure 2.5D). The A_3B_3 complex, the central stem and the c-ring are the domains with the highest density. The c-ring is a compact barrel and depending on the arrangement of the individual subunits, the thickness of the ring varies considerably. Six distinct areas with increased thickness are distinguishable (red arrowheads Figure 2.5B). The distribution suggests six proteolipid subunits for the bovine V-ATPase. Figure 2.5C1 shows a longitudinal projection of the isolated membrane ring. Difference-mapping of this projection with the same but six-fold symmetrized image reveals a strong density in the upper part of the ring (arrowheads Figure 2.5C2). This additional density is adjacent to the large peripheral stalk but not to the smaller isolated density.

2.4 Discussion

2.4.1 Cryo-electron microscopy

Cryo-electron microscopy allows imaging of proteins in native conformation, without artifacts caused by heavy metal salt stains (Dubochet et al., 1988). We present the first 3D reconstruction of a V-ATPase from cryo-electron microscopy images. The concentration of the pure V-ATPase preparation was estimated 0.3 mg/ml and was insufficient to ob-

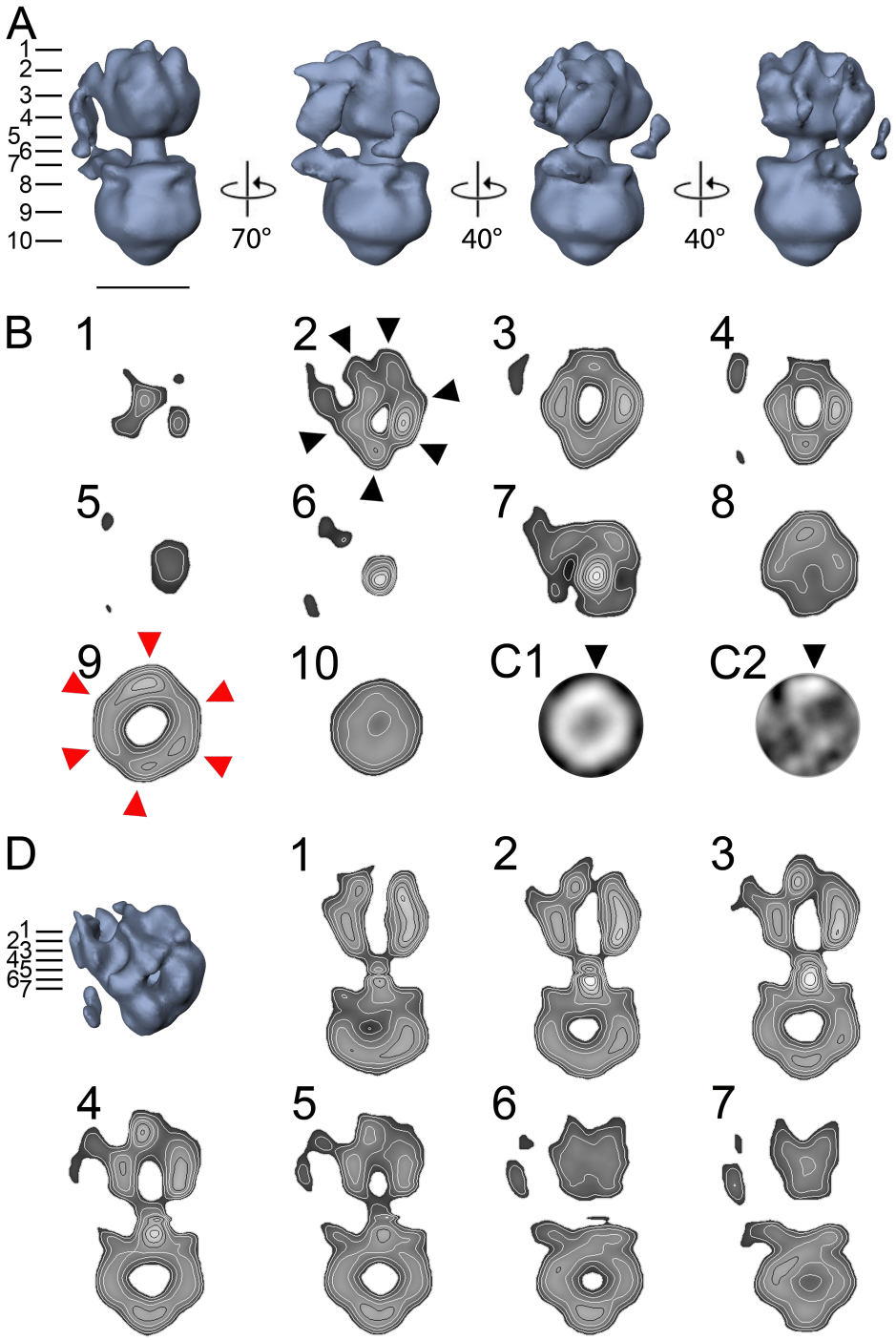

Figure 2.5: **Surface and contour representations of the merged 3D reconstruction.** (A) Surface representation of the merged 3D reconstruction displayed at different orientations emphasizing the peripheral stator domain. (B) Visualization of the internal structure. Contoured cross-sections perpendicular to the long axis at the levels indicated by the bars in panel (A). The black arrowheads display the position of the subunits of the A_3B_3 complex. The red arrowheads show the hexagonal density distribution in the membrane domain. (C1) Projection of the isolated density of the membrane domain. (C2) Difference map of the projection shown in C1 and its six-fold symmetrized equivalent. (D) Vertical sections through the volume at the levels indicated by the bars. Scale bar 100 Å.

tain images of the complex over holes of perforated carbon film, mainly due to the presence of detergent. Therefore, the particles were adsorbed to thin carbon film and vitrified. Adsorption to a carbon support can lead to flattening of the particles, albeit to a lesser extent compared to negative stain methods. The thickness of the ice layer on the grid was particularly important. Particles were concen-

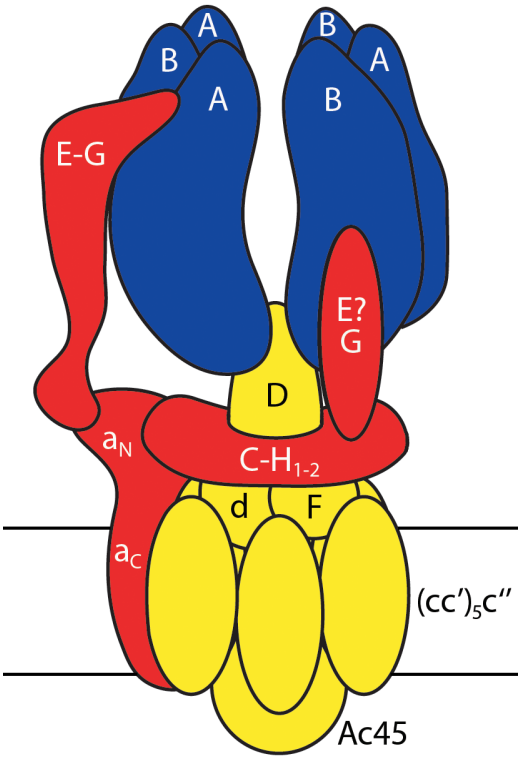

Figure 2.6: **Model of the subunit composition.** The catalytic part is highlighted in blue, the peripheral stator complex in red and the rotor domain in yellow. The horizontal lines indicate the position of the membrane. The model is based on interpretation of our 3D reconstruction and on previously published results from cross-linking and two hybrid binding experiments.

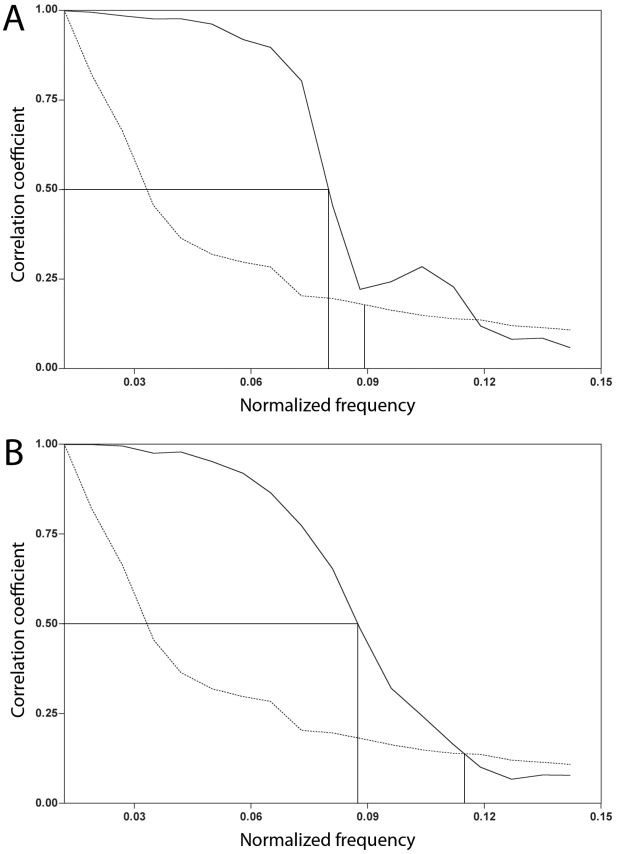

Figure 2.7: Supplementary Figure. **Resolution assessment.** (A) Fourier shell correlation curve of the V_1 reconstruction. The dotted line indicates five times the noise correlation curve (5σ). The resolution was estimated to 34 Å (0.5 cutoff) or 30 Å (5σ criterion). (B) Fourier shell correlation of the V_O reconstruction resulted in a resolution of 31 Å (0.5 cutoff) or 23 Å (5σ criterion).

trated in restricted areas with a distinct ice thickness, whereas large regions of the grid squares were empty. The elongated shape of the complex enforced adsorption with the long axis parallel to the carbon film. Furthermore, the physical constraint impeding adsorption with the large peripheral stalk facing the carbon film, led to a missing wedge of nearly 60 degrees in the density map (Supplementary Figure 2.8A). However, except for this missing wedge, the angular distribution of the projections is sufficiently balanced. The difference in the histograms for V_1 and V_O (Supplementary Figure 2.8A and 2.8B) can be explained by the presence of three distinct conformations with an angular shift of the rotor by 120/240 degrees relatively to the stator. In the histogram, covering 180 degrees, this can lead to a partial shift of the large peak at $\Theta \approx 10$ degrees (Supplementary Figure 2.8A) to $\Theta \approx 70/130$ degrees (Supplementary Figure 2.8B), due to averaging of the three conformations.

2.4.2 Individual processing of V_1 and V_O due to flexibility of the holoenzyme

The particular architecture of the V-ATPase implies that the relatively thin linker region between the cytosolic and the membrane domain is likely to be flexible. Confirmation was obtained by comparison of images of the holoenzyme that were aligned both, on masked V_1 and V_O references and on unmasked references (Figure 2.2B-D and Figure 2.3B). The averages of the masked partial complexes, especially of V_1, showed significantly more detail. Three (Figure 2.2C3, C4, C5) or four (Figure 2.2C1, C2) asymmetrically arranged distinct lobes are visible in V_1, consitent with projections of a pseudo-hexagonal array. In (Figure 2.2B) the V_1 subunits are less well resolved. Alignment of the holoenzyme images on masked references also led to the displacement off the vertical axis of densities lying outside the mask (Figure 2.3B). By classifica-

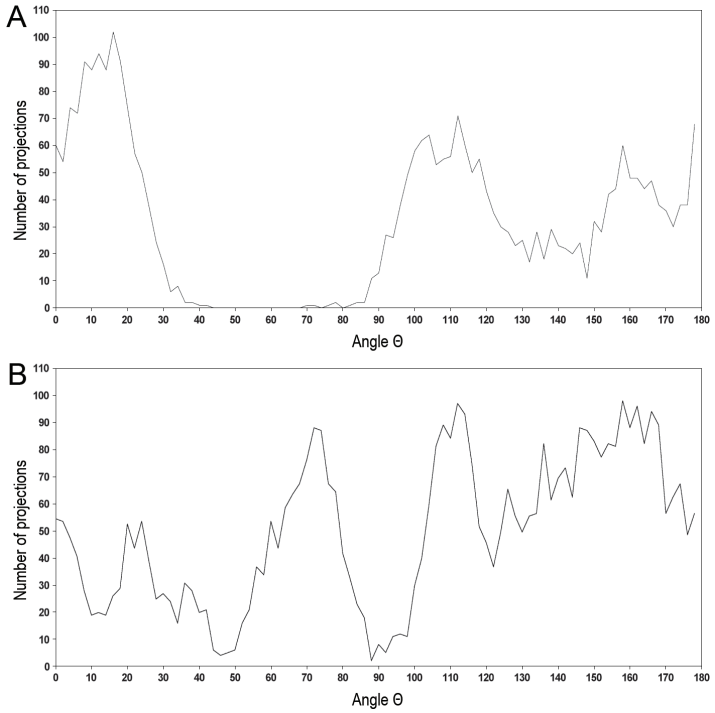

Figure 2.8: Supplementary Figure. **Angular distribution of the projections.** (A) Euler angle distribution of the side view projections contributing to the V_1 reconstruction and (B) to the V_O reconstruction.

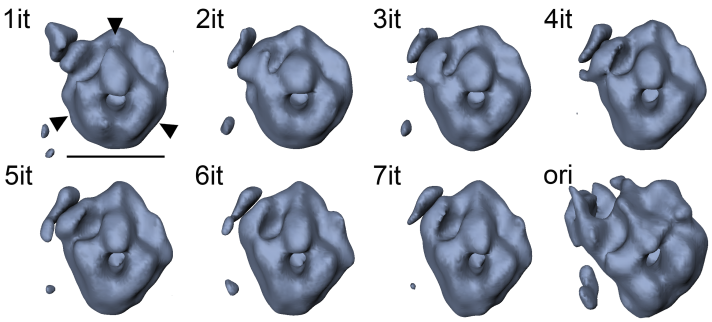

Figure 2.9: Supplementary Figure. **Symmetry of the A_3B_3 complex.** Top view series of 3D reconstructions obtained after one to seven iterations (1it - 7it) of projection matching and back-projection, starting from a reference with a three-fold symmetrized A_3B_3 complex. The last panel shows a top view of the original 3D map (ori) (Figure 2.4B). The arrowheads show the three-fold symmetry present after the first iteration. The symmetry gradually disappears in the refinement process and the A_3B_3 complex assumes an elongated shape. Scale bar 100 Å.

tion the varying bending levels of the particles could be resolved. The hypothesis, that the V-ATPase naturally adopts a strongly curved shape and that different bending levels correspond to different orientations, can be excluded. The class averages in Figure 2.2B and Figure 2.3A, obtained from straight particles, display distinct features such as the large peripheral arm or the asymmetric array of V_1 in various orientations. If the particles were curved, these features would always be in the same place or mirrored on the long axis. In addition, 3D orientation search prior to merging the V_1 and V_O maps resulted in a joined reconstruction with a rather straight central axis.

Given the high flexibility of the central linker region connecting V_1 and V_O, in order to avoid resolution loss due to a heterogeneous particle population, we calculated individual 3D maps for the two sub-complexes and eventually merged the two reconstructions in the correct relative orientation.

2.4.3 Catalytic domain and central stalk

Six subunits of the catalytic domain form an irregular, elongated hexagon with a prominent cav-

ity inside. A distinct six-fold array is visible in the cytosol-facing part of the A_3B_3 (black arrowheads Figure 2.5B2). The membrane-facing part of the same hexagonal array is less well resolved. Surprisingly, the V_1 domain in our reconstruction is different from the rather regular three-fold arrangement of the F_1-ATPase (Abrahams et al., 1994). Despite the presence of three densities at the cytosol-facing tip (Figure 2.5B1), the three-fold symmetry in our map is less obvious, compared to the F-ATPase and compared to a previously published negative stain map of V_1 (Radermacher et al., 2001). To test the correctness of the angular refinement in our 3D map, the A_3B_3 complex was three-fold symmetrized, prior to attaching the large peripheral stalk and the isolated peripheral density to the symmetrized complex. This model was used as initial reference for projection matching without symmetry constraints. The initially enforced three-fold symmetry was not stable for many iterations but gradually changed back towards the original elongated shape (Supplementary Figure 2.9). A possible conclusion is that the V-ATPase subunits A and B are arranged in a rather irregular fashion compared to the $\alpha_3\beta_3$ complex of the F-ATPase. However, the elliptic appearance of the V_1 domain in our reconstruction is unexpected. A possible explanation is that the missing densities around $\Theta \approx$30-90 degrees (Supplementary Figure 2.8A) are the cause of artificial stretching and blurring of the 3D map. Alternating hydrolysis of ATP at the three catalytic sites causes cyclic conformational changes in the A_3B_3 complex, which drive step-wise rotation of the central axle. For maximum efficiency, analogously to the F-ATPase subunit γ (Abrahams et al., 1994), an asymmetric central stalk is necessary. The truncated stalks of the V_1 (Figure 2.4A) and V_O (Figure 2.4B) reconstructions are indeed asymmetric. However, addition of the two individual maps (Figure 2.5A) caused a partial accumulation of density in the central stalk, which is artificial. A correction was not applied because it would imply arbitrary weighting of the voxel values in both maps, and hence create new artifacts. In contrast to the F-ATPase, where the γ subunit spans the interior of the $\alpha_3\beta_3$ complex from top to bottom, in our V-ATPase reconstruction, the central stalk is only partially inserted into the membrane-facing side of the A_3B_3 complex. The large cavity in V_1 is in agreement with previously published negative stain reconstructions (Domgall et al., 2002; Venzke et al., 2005; Wilkens et al., 2004).

Based on cross-linking experiments (Arata et al., 2002; Wilkens et al., 2005) proposed that the central stalk may be composed of the subunits D and F (Figure 2.6), and that subunit D would be the counterpart of subunit γ in the F-ATPase. Another model however, suggests that the central stalk is made of the subunits E and G (Chaban et al., 2002; Grüber et al., 2000; Xie, 1996). Evidence for this opposite view came from proteolysis experiments, which indicated a central position for the subunits E and G (Grüber et al., 2000). Additional support was provided by activity experiments showing that the subunits E and G, but not the subunits D and F, are essential to ensure ATP hydrolysis activity (Xie, 1996).

2.4.4 Peripheral stalk

The least understood domain of the V-ATPase is the peripheral stator. It is essential for preventing rotation of the catalytic domain against the remainder of the complex, thus enabling proton transport through the membrane. The number and design of the peripheral connection(s) is controversial, and there is evidence that the architecture of the V-ATPase may differ from species to species. The 3D reconstruction we present displays a large peripheral stalk and an additional isolated density, possibly part of a second, less well resolved connection (Figure 2.5A). The 120 Å long peripheral stalk is attached laterally to the long side of the stretched hexagonal A_3B_3 array and to a terrace-like density that protrudes from the collar-like structure surrounding the central stalk (Figure 2.5A). This terrace-like density is adjacent to the area of the membrane domain that was found to be occupied by the 96 kDa subunit a (Figure 2.5B). Since the mass of the soluble domain of subunit a (Wilkens and Forgac, 2001) matches the volume of the terrace-like density, in all probability, in this area the subunit a makes contact to the V_1 subunits of the peripheral stalk.

Besides the large peripheral stalk, at a similar distance from the central stalk, a second isolated density is present in our 3D map (Figure 2.5A). The orientation of this density and the fact that, in the top view, it forms an isosceles triangle with the central and the peripheral stalk, indicate a possible involvement in a second, less well resolved peripheral connection. The relative orientation of the peripheral

stalk and the isolated density is similar to the one of the two peripheral connections that were described for the V-ATPase of *Neurospora crassa* (Venzke et al., 2005) and for the H^+ ATPase/Synthase of *Thermus thermophilus* (Bernal and Stock, 2004). However, these reconstructions show two peripheral stalks of about the same thickness. The stator system in our reconstruction with one predominant peripheral connection resembles the one of the plant V-ATPase from *Kalanchoë daigremontiana* (Domgall et al., 2002), although there two isolated densities were described. The dominance of one stalk is consistent with the class averages. The large peripheral stalk is very distinct (Figure 2.2B2, Figure 2.3A3 and 2.3A6), whereas none of the averages shows a second connection. Finally, comparison of our 3D map with a negative stain reconstruction of the bovine V-ATPase reveals significant differences in the central domain, which we cannot explain. In the reconstruction by (Wilkens et al., 2004) the collar-like structure is subdivided into five isolated peripheral units, which are arranged around the central axis. Two of these isolated densities form thin, short connections to the membrane-facing part of the A_3B_3 complex, just spanning the gap between the cytosolic and the membrane domain. This stands in contrast to the 3D map we present, and to reconstructions from other species (Bernal and Stock, 2004; Domgall et al., 2002; Venzke et al., 2005).

Limited information about the position and the interactions of involved subunits was gained from cross-linking and two hybrid binding experiments (Adachi et al., 1990; Puopolo et al., 1992; Wilkens et al., 2005; Xu et al., 1999). These data suggest that the long stretch of the stalk is composed of the subunits E and G (Figure 2.6). The interaction of the subunits E and a, demonstrated by cross-linking experiments (Xu et al., 1999), provides evidence for a peripheral location of the subunit E. In our reconstruction, the elongated density of the peripheral stalk, excluding the contact regions with the catalytic and the membrane domain, has a volume that corresponds to a protein mass of about 41 kDa. Both, the E-G and the D-F complexes have a mass of 40-41 kDa and could be accommodated in this volume. However, opposite to the subunit F, two copies of the subunit G have been predicted for the bovine V-ATPase (Arai et al., 1988; Xu et al., 1999). In addition, a recent publication on the yeast V-ATPase (Ohira et al., 2006) suggests the presence of more than one copy of the subunit E. The isolated peripheral density in our reconstruction has a volume that would roughly accommodate the 14 kDa subunit G, but not a second copy of subunit E (Figure 2.6). It is possible, that the densities corresponding to a hypothetic second subunit E were averaged out, since there is no connection from the isolated density to the remainder of the complex. Another possibility is that the elongated subunit C protrudes from the collar-like structure and contributes to the peripheral stator, as proposed for the yeast V-ATPase (Drory et al., 2004).

2.4.5 Membrane-associated domain

A massive, irregular ring accounts for the largest portion of V_O domain. On the surface representations (Figure 2.4B) structured features resembling the edges of an irregular screw nut are visible. Comparing two side views at a relative angle of 90 degrees, the complex reveals an elliptical rather than a circular shape. The ellipse is not centered with respect to the long axis of the molecule, but arises through a prominent lateral bulge (arrowheads Figure 2.4B). This bulge is likely to be caused by the 96 kDa subunit a, which is believed to form the membrane-resident part of the peripheral stalk (Figure 2.6). The position of subunit a could be determined by difference-mapping of a projection of the isolated membrane domain and its six-fold symmetrized equivalent (Figure 2.5C). The difference map displays a large supplemental density that spatially coincides with the lateral bulge mentioned above.

The number of proteolipid subunits, predicted to have four trans-membrane helices each, was never determined with certainty and may even vary, depending on the species, similarly to what was observed in the case of the F-ATPase (Pogoryelov et al., 2005; Seelert et al., 2000; Stahlberg et al., 2001; Stock et al., 1999). The density distribution of the membrane domain in our reconstruction clearly shows a hexagonal design (red arrowheads Figure 2.5B), and thus indicates the presence of six proteolipid subunits for the bovine brain V-ATPase. This would account for 24 trans-membrane helices, which is in the range of 20-28 helices, as documented for two F-ATPase species (Meier et al., 2005; Stock et al., 1999).

Inside the compact walls of the proteolipid bar-

rel, a large cavity is visible (Figure 2.5B-D). The side views of the interior of the 3D map display a nearly spherical frame of densities surrounding the cavity (Figure 2.5D). At the extra-cytosolic end of the proteolipid barrel, a compact globular density is present. The logical candidate for this density is the Ac45 subunit that is characteristic for bovine V-ATPases. In our reconstruction, it appears more tightly embedded into the proteolipid pocket, compared to the negative stain reconstruction of the same enzyme published by (Wilkens and Forgac, 2001). On the opposite side of the proteolipid barrel, the central stalk assumes a wider shape in the area that makes contact with the membrane domain. This density seems to form a lid that plugs the proteolipid ring, and at the same time smoothly merges into the collar-like density (Figure 2.5D). In our reconstruction, the collar-like density appears as a ring with varying thickness. Compared to previously published 3D maps, it is most similar to the same region of the *Thermus thermophilus* H^+ ATPase/synthase, where the authors describe a rather irregular disc, surrounding the central stalk (Bernal and Stock, 2004). The reconstruction of the V-ATPase from the fungus *Neurospora crassa* (Venzke et al., 2005) is also similar in design, but there the central stalk is not entirely surrounded by a disc-shaped density. Instead, a semi-circular density is attached to one side of the central stalk. In the previously mentioned reconstruction of the bovine V-ATPase (Wilkens et al., 2004), rather than a compact collar-like structure, five individual peripheral densities were described. With respect to our 3D map, obtained from low contrast cryo-electron micrographs, it could be argued that in the refinement the individual densities could not be resolved and were instead merged to a continuous ring. However, in the face of the well resolved edges of the screw-nut-shaped membrane domain and the evident asymmetry of the truncated central stalk, this hypothesis is very unlikely.

2.5 Experimental procedures

2.5.1 Preparations

The bovine brain V-ATPase was purified to a specific activity of 14-16 μmoles P_i/(mg·min), as described (Xie and Stone, 1986).

2.5.2 Reconstitution of the V-ATPase into proteoliposomes

The bovine brain V-ATPase was reconstituted into liposomes, which contain phosphatidylcholine (PC), phosphatidylethanolamine (PE), phosphatidylserine (PS) and cholesterol at a weight ratio of 40:26.5:7.5:26, by the cholate dilution, freeze-thaw method, as described (Xie et al., 1986) with some modifications. Liposomes (200 μg) were added to 1 μg of V-ATPase and were well mixed. Glycerol, Na-cholate, KCl, and $MgCl_2$ were added to the protein-lipid mixture at final concentrations of 10% (vol/vol), 1%, 0.15 M and 2.5 mM, respectively. The reconstitution mixture was incubated at room temperature (RT) for 1 h, frozen in liquid N_2 for one min and then thawed at RT. In order to form tightly sealed proteoliposomes, the reconstituted samples had to be diluted at least 20-fold to decrease the concentration of both detergents, cholate and C12E9, to a level well below their respective critical micellar concentration. This was not performed in a separate step but was instead accomplished during the proton translocation assay by adding samples into the assay buffer in a cuvette with a magnetic bar at the bottom, resulting in over 90-fold dilution.

2.5.3 Measurement of proton translocation

Proton translocation activity of the reconstituted proteoliposomes was measured using the acridine orange quenching method (Xie and Stone, 1986) conducted in a SLM-Aminco DW2C dual wavelength spectrophotometer and the activity was registered as $\Delta A_{492\text{-}540}$. 16 μl proteoliposomes containing 1 μg of intact V-ATPase were added to 1.5 ml of proton pumping assay buffer that consisted of 20 mM Tricine, pH 7.0, 6.7 μM acridine orange, 3 mM $MgCl_2$, 150 mM KCl, and 1 μM valinomycin. The reaction was initiated by addition of 1.3 mM ATP (pH 7.0) and was stopped by adding 1 μM of 1799, a proton ionophore.

2.5.4 Electron microscopy of negatively stained samples

3 μl of the protein solution (diluted to 0.03 mg/ml) was applied to a thin carbon film rendered hydrophilic by glow-discharge at low pressure in air, which was mounted on a 400 mesh copper grid.

The grid was washed with 6 drops of water and stained with 2% uranyl acetate. A Philips CM120 microscope operating at 100 kV was used to record images on Kodak SO-163 film. The micrographs, recorded at a magnification of 50kx, were developed 8 minutes in Kodak D19 full strength developer.

2.5.5 Cryo-electron microscopy

3 μl of the protein solution (0.3 mg/ml) was adsorbed to a thin carbon film as for negative staining. The grid was washed with 6 drops of water, blotted and quick-frozen in liquid ethane. 80% of the images were taken on Kodak SO-163 film using a Philips CM200 FEG microscope operating at 200 kV. The negatives were developed 12 minutes in Kodak D19 full strength developer. 20% of the images were recorded with the Leginon automated imaging software (Carragher et al., 2000) on a TVIPS 4k x 4k CCD camera connected to a Tecnai F20 microscope, operating at 120 kV. All the micrographs were taken under low-dose conditions, at a magnification of 50kx.

2.5.6 Reference generation from negative stain images

The negatives were digitized with a Zeiss SCAI Scanner at a resolution of 1.4 Å/px at the specimen level. The resolution was binned to 4.2 Å/px. EMAN boxer (Ludtke et al., 1999) was used to select 2785 particles from the negatives. For further processing, SPIDER (Frank et al., 1996) was employed. The boxed particles were subjected to reference-free alignment (Penczek et al., 1992) and classification by multivariate statistical analysis (Frank and van Heel, 1982; van Heel and Frank, 1981). The first volume was generated from 12 class averages, and was subsequently refined by projection matching with the 2785 selected particles. Spherical masks were applied to the refined starting model to generate two truncated 3D maps of V_1 and V_O, both containing overlapping densities of the central domains of the intact complex.

2.5.7 Image processing of cryo-micrographs

The negatives were digitized with a Heidelberg Primescan D 7100 drum scanner at a resolution of 2.7 Å/px at the specimen level. This corresponds to the resolution of the TVIPS CCD camera at a magnification of 50kx. 6496 particles were selected using EMAN boxer (Ludtke et al., 1999). All the further processing was done with SPIDER (Frank et al., 1996). Projections of the refined negative stain volume, calculated at different angles, served as references for alignment of the cryo-data set. The aligned cryo-particles were masked with the same parameters, shifted to the center of the image, and classified according to their angular orientation in the final 3D map, allowing a maximal deviation of $\pm$ 10 degrees. As a starting model for the 3D reconstruction, the previously obtained negative stain volumes of V_1 and V_O were used. Initially, 6496 masked V_1 and V_O particles were used for refinement by projection matching. Particles with a low cross-correlation value relative to the reference projections were omitted from the reconstruction. After 120 iterations with increasing angular accuracy, two individual volumes of V_1 (2879 particles) and V_O (4547 particles) were obtained. The contrast transfer function (CTF) was corrected using a Wiener filter (Schiske, 1973). The redundant densities of V_1 and V_O volumes were aligned by 3D cross-correlation. The two densities were added in the correct orientation. For resolution assessment, Fourier shell correlations (0.5 cutoff) (Saxton and Baumeister, 1982) of the individual sub-complexes were calculated. Surface representations were made with DINO (www.dino3d.org).

2.6 Acknowledgements

We thank Joel Quispe and Francisco Guerra for their help with Leginon, Mohamed Chami for discussions about the imaging of the V-ATPase in ice, and Nicolas Boisset for his encouragement in the image processing. This work was supported by the Maurice E. Müller Foundation of Switzerland, by the Swiss National Foundation (SNF) within the framework of the National Center of Competence in Research for Structural Biology, the SNF grant 3100-059415 to AE, and the NoE 3D-EM, EU project (LSHG-CT-2004-502828).

2.7 References

Abrahams, J.P., Leslie, A.G., Lutter, R. and Walker, J.E. (1994) Structure at 2.8 Å resolution of F_1-ATPase from bovine heart mitochondria. Nature, 370, 621-628.

Adachi, I., Puopolo, K., Marquez-Sterling, N., Arai, H. and Forgac, M. (1990) Dissociation, cross-linking, and glycosylation of the coated vesicle proton pump. J Biol Chem, 265, 967-973.

Arai, H., Terres, G., Pink, S. and Forgac, M. (1988) Topography and subunit stoichiometry of the coated vesicle proton pump. J Biol Chem, 263, 8796-8802.

Arata, Y., Baleja, J.D. and Forgac, M. (2002) Cysteine-directed cross-linking to subunit B suggests that subunit E forms part of the peripheral stalk of the vacuolar H^+-ATPase. J Biol Chem, 277, 3357-3363.

Bernal, R.A. and Stock, D. (2004) Three-dimensional structure of the intact Thermus thermophilus H^+-ATPase/synthase by electron microscopy. Structure (Camb), 12, 1789-1798.

Blair, H.C., Teitelbaum, S.L., Ghiselli, R. and Gluck, S. (1989) Osteoclastic bone resorption by a polarized vacuolar proton pump. Science, 245, 855-857.

Brown, D. and Breton, S. (1996) Mitochondria-rich, proton-secreting epithelial cells. J Exp Biol, 199, 2345-2358.

Brown, D., Lui, B., Gluck, S. and Sabolic, I. (1992) A plasma membrane proton ATPase in specialized cells of rat epididymis. Am J Physiol, 263, C913-916.

Carragher, B., Kisseberth, N., Kriegman, D., Milligan, R.A., Potter, C.S., Pulokas, J. and Reilein, A. (2000) Leginon: an automated system for acquisition of images from vitreous ice specimens. J Struct Biol, 132, 33-45.

Chaban, Y., Ubbink-Kok, T., Keegstra, W., Lolkema, J.S. and Boekema, E.J. (2002) Composition of the central stalk of the Na^+-pumping V-ATPase from Caloramator fervidus. EMBO Rep, 3, 982-987.

Crider, B.P. and Xie, X.S. (2003) Characterization of the functional coupling of bovine brain vacuolar-type H^+-translocating ATPase. Effect of divalent cations, phospholipids, and subunit H (SFD). J Biol Chem, 278, 44281-44288.

Domgall, I., Venzke, D., Luttge, U., Ratajczak, R. and Böttcher, B. (2002) Three-dimensional map of a plant V-ATPase based on electron microscopy. J Biol Chem, 277, 13115-13121.

Drory, O., Frolow, F. and Nelson, N. (2004) Crystal structure of yeast V-ATPase subunit C reveals its stator function. EMBO Rep, 5, 1148-1152.

Dubochet, J., Adrian, M., Chang, J.J., Homo, J.C., Lepault, J., McDowall, A.W. and Schultz, P. (1988) Cryo-electron microscopy of vitrified specimens. Q Rev Biophys, 21, 129-228.

Feng, Y. and Forgac, M. (1992) Cysteine 254 of the 73-kDa A subunit is responsible for inhibition of the coated vesicle H^+-ATPase upon modification by sulfhydryl reagents. J Biol Chem, 267, 5817-5822.

Frank, J., Radermacher, M., Penczek, P., Zhu, J., Li, Y., Ladjadj, M. and Leith, A. (1996) SPIDER and WEB: processing and visualization of images in 3D electron microscopy and related fields. J Struct Biol, 116, 190-199.

Frank, J. and van Heel, M. (1982) Correspondence analysis of aligned images of biological particles. J Mol Biol, 161, 134-137.

Grüber, G., Radermacher, M., Ruiz, T., Godovac-Zimmermann, J., Canas, B., Kleine-Kohlbrecher, D., Huss, M., Harvey, W.R. and Wieczorek, H. (2000) Three-dimensional structure and subunit topology of the V_1 ATPase from Manduca sexta midgut. Biochemistry, 39, 8609-8616.

Hirata, R., Graham, L.A., Takatsuki, A., Stevens, T.H. and Anraku, Y. (1997) VMA11 and VMA16 encode second and third proteolipid subunits of the Saccharomyces cerevisiae vacuolar membrane H^+-ATPase. J Biol Chem, 272, 4795-4803.

Inoue, T., Wilkens, S. and Forgac, M. (2003) Subunit structure, function, and arrangement in the yeast and coated vesicle V-ATPases. J Bioenerg Biomembr, 35, 291-299.

Junge, W. and Nelson, N. (2005) Structural biology. Nature's rotary electromotors. Science, 308, 642-644.

Leng, X.H., Manolson, M.F., Liu, Q. and Forgac, M. (1996) Site-directed mutagenesis of the 100-kDa subunit (Vph1p) of the yeast vacuolar H^+-ATPase. J Biol Chem, 271, 22487-22493.

Ludtke, S.J., Baldwin, P.R. and Chiu, W. (1999) EMAN: semiautomated software for high-resolution single-particle reconstructions. J Struct Biol, 128, 82-97.

Meier, T., Polzer, P., Diederichs, K., Welte, W. and Dimroth, P. (2005) Structure of the rotor ring of F-Type Na^+-ATPase from Ilyobacter tartaricus. Science, 308, 659-662.

Müller, V. and Grüber, G. (2003) ATP synthases: structure, function and evolution of unique energy converters. Cell Mol Life Sci, 60, 474-494.

Ohira, M., Smardon, A.M., Charsky, C.M., Liu, J., Tarsio, M. and Kane, P.M. (2006) The E and G subunits of the yeast V-ATPase interact tightly and are both present at more than one copy per V_1 complex. J Biol Chem, 281, 22752-22760.

Penczek, P., Radermacher, M. and Frank, J. (1992) Three-dimensional reconstruction of single particles embedded in ice. Ultramicroscopy, 40, 33-53.

Pogoryelov, D., Yu, J., Meier, T., Vonck, J., Dimroth, P. and Müller, D.J. (2005) The c15 ring of the *Spirulina platensis* F-ATP synthase: F1/F0 symmetry mismatch is not obligatory. EMBO Rep, 6, 1040-1044.

Puopolo, K., Sczekan, M., Magner, R. and Forgac, M. (1992) The 40-kDa subunit enhances but is not required for activity of the coated vesicle proton pump. J Biol Chem, 267, 5171-5176.

Radermacher, M., Ruiz, T., Wieczorek, H. and Grüber, G. (2001) The structure of the V_1-ATPase determined by three-dimensional electron microscopy of single particles. J Struct Biol, 135, 26-37.

Saxton, W.O. and Baumeister, W. (1982) The correlation averaging of a regularly arranged bacterial cell envelope protein. J Microsc, 127 (Pt 2), 127-138.

Schiske, P. (1973) Image processing using additional statistical information about the object. In: Image processing and computer-aided design in electron optics., Hawkes P.W. Academic Press London pp 82-90.

Seelert, H., Poetsch, A., Dencher, N.A., Engel, A., Stahlberg, H. and Müller, D.J. (2000) Structural biology. Proton-powered turbine of a plant motor. Nature, 405, 418-419.

Stahlberg, H., Müller, D.J., Suda, K., Fotiadis, D., Engel, A., Meier, T., Matthey, U. and Dimroth, P. (2001) Bacterial Na^+-ATP synthase has an undecameric rotor. EMBO Rep, 2, 229-233.

Steinmetz, P.R. (1986) Cellular organization of urinary acidification. Am J Physiol, 251, F173-187.

Stock, D., Leslie, A.G. and Walker, J.E. (1999) Molecular architecture of the rotary motor in ATP synthase. Science, 286, 1700-1705.

Vaananen, H.K., Karhukorpi, E.K., Sundquist, K., Wallmark, B., Roininen, I., Hentunen, T., Tuukkanen, J. and Lakkakorpi, P. (1990) Evidence for the presence of a proton pump of the vacuolar H^+-ATPase type in the ruffled borders of osteoclasts. J Cell Biol, 111, 1305-1311.

van Heel, M. and Frank, J. (1981) Use of multivariate statistics in analysing the images of biological macromolecules. Ultramicroscopy, 6, 187-194.

Venzke, D., Domgall, I., Kocher, T., Fethiere, J., Fischer, S. and Böttcher, B. (2005) Elucidation of the stator organization in the V-ATPase of Neurospora crassa. J Mol Biol, 349, 659-669.

Wieczorek, H., Brown, D., Grinstein, S., Ehrenfeld, J. and Harvey, W.R. (1999) Animal plasma membrane energization by proton-motive V-ATPases. Bioessays, 21, 637-648.

Wilkens, S. and Forgac, M. (2001) Three-dimensional structure of the vacuolar ATPase proton channel by electron microscopy. J Biol Chem, 276, 44064-44068.

Wilkens, S., Inoue, T. and Forgac, M. (2004) Three-dimensional structure of the vacuolar ATPase. Localization of subunit H by difference imaging and chemical cross-linking. J Biol Chem, 279, 41942-41949.

Wilkens, S., Vasilyeva, E. and Forgac, M. (1999) Structure of the vacuolar ATPase by electron microscopy. J Biol Chem, 274, 31804-31810.

Wilkens, S., Zhang, Z. and Zheng, Y. (2005) A structural model of the vacuolar ATPase from transmission electron microscopy. Micron, 36, 109-126.

Xie, X.S. (1996) Reconstitution of ATPase activity from individual subunits of the clathrin-coated vesicle proton pump. The requirement and effect of three small subunits. J Biol Chem, 271, 30980-30985.

Xie, X.S. and Stone, D.K. (1986) Isolation and reconstitution of the clathrin-coated vesicle proton translocating complex. J Biol Chem, 261, 2492-2495.

Xie, X.S., Tsai, S.J. and Stone, D.K. (1986) Lipid requirements for reconstitution of the proton-translocating complex of clathrin-coated vesicles. Proc Natl Acad Sci U S A, 83, 8913-8917.

Xu, T., Vasilyeva, E. and Forgac, M. (1999) Subunit interactions in the clathrin-coated vesicle vacuolar H^+-ATPase complex. J Biol Chem, 274, 28909-28915.

Chapter 3

Structural insights into the secretin PulD and its trypsin-resistant core

Mohamed Chami[1,4], Ingrid Guilvout[2,4], **Marco Gregorini**[1], Hervé-W. Rémigy[1], Shirley A. Müller[1], Marielle Valerio[3], Andreas Engel[1], Anthony P. Pugsley[2], Nicolas Bayan[2]

3.1 Abstract

Limited proteolysis, secondary structure and biochemical analyses, mass spectrometry and mass measurements by scanning transmission electron microscopy were combined with cryo-electron microscopy to generate a 3D model of the homomultimeric complex formed by the outer membrane secretin PulD, an essential channel-forming component of the type II secretion system from *Klebsiella oxytoca*. The complex is a dodecameric structure composed of two rings that sandwich a closed disc. The two rings form chambers on either side of a central plug that is part of the middle disc. The PulD polypeptide comprises two major, structurally quite distinct domains, an N domain that forms the walls of one of the chambers and a trypsin-resistant C domain that contributes to the outer chamber, the central disc and the plug. The C domain contains a lower proportion of potentially transmembrane β structure than classical outer membrane proteins, suggesting that only a small part of it is embedded within the outer membrane. Indeed, the C domain probably extends well beyond the confines of the outer membrane bilayer, forming a centrally plugged channel that penetrates both the peptidoglycan on the periplasmic side and the lipopolysaccharide and capsule layers on the cell surface. The inner chamber is proposed to constitute a docking site for the secreted exoprotein pullulanase, while the outer chamber could allow displacement of the plug to open the channel and permit the exoprotein to escape.

3.2 Introduction

The widespread Type II secretion systems (T2SS) of Gram-negative bacteria allow the secretion of hydrolytic enzymes (lipases, amylases) or virulence factors, collectively referred to as exoproteins, into the external medium (Pugsley, 1993; Sandkvist, 2001). These exoproteins are first translocated by the Sec (Pugsley et al., 1991) or Tat (Voulhoux et al., 2001) translocons into the periplasm. They are then specifically transported through the outer membrane by an ATP and proton-motive force-dependent machinery (the secreton) (Letellier et al., 1997; Possot et al., 1997) composed of 12 to 15 proteins (Pugsley, 1993; Sandkvist, 2001). The secreton components include several integral inner membrane proteins, pseudopilins (proteins with structural features similar to those of type IV pilins (Köhler et al., 2004)), and an integral outer membrane protein called secretin. Besides their role in protein secretion by the T2SS (e.g., *Klebsiella oxytoca* protein PulD (Hardie et al., 1996a) and *Pseudomonas aeruginosa*

[1]M.E.Müller Institute, Biozentrum, University of Basel, Klingelbergstrasse 50/70, CH-4056 Basel, Switzerland

[2]Molecular Genetics Unit, CNRS URA2175, Institut Pasteur, 25 rue du Dr. Roux, 75724 Paris cedex 15, France

[3]Laboratoire de Modélisation et Ingénierie des Proteines, Université de Paris XI-Orsay, 15 rue G. Clémenceau, 91405 Orsay cedex, France

[4]These authors contributed equally.

protein XcpQ (Bitter et al., 1998; Koster et al., 1997)) and the Type III secretion system (e.g., *Yersinia enterocolitica* protein YscC (Koster et al., 1997)), secretins are also required for filamentous bacteriophage secretion (e.g., bacteriophage f1 protein pIV (Linderoth et al., 1996)) and type IV pilus assembly(e.g., *Neisseria meningitidis* and *P. aeruginosa* PilQ (Bitter et al., 1998; Collins et al., 2001)).

According to electron microscopy, 12 to 14 identical secretins form ring-like complexes with an internal channel (estimated diameters range from 5 nm (PilQ, YscC) to 10 nm (XcpQ) (Bitter et al., 1998; Brok et al., 1999; Burghout et al., 2004)) large enough to accommodate their substrates (Bitter et al., 1998; Koster et al., 1997; Linderoth et al., 1997; Nouwen et al., 1999). Negative stain analysis of PulD (Nouwen et al., 2000) and cryo-electron microscopy of pIV (Opalka et al., 2003) revealed a central channel plug. Incorporation of secretins into the *Escherichia coli* outer membrane causes neither leakage of periplasmic proteins nor increased sensitivity to small toxic compounds that are unable to breach the outer membrane (Guilvout et al., 1999). Furthermore, PulD, pIV, XcpQ and YscC all form very small conductance channels in lipid bilayers (Brok et al., 1999; Burghout et al., 2004; Marciano et al., 2001; Marciano et al., 1999; Nouwen et al., 1999).

Comparison of secretin sequences led to the definition of two major domains of approximately equal length (Guilvout et al., 1999). The predicted domain organization was confirmed by analysis of trypsin or proteinase K-resistant domains of PulD and XcpQ (Brok et al., 1999; Nouwen et al., 2000) that, in the case of XcpQ, formed channels whose conductance was similar to that of the intact protein (Brok et al., 1999). These data prompted speculation that the well conserved secretin C domain is anchored in the outer membrane by 10 to 14 potentially transmembrane amphipathic β strands (Guilvout et al., 1999) characteristic of other outer membrane proteins (Koebnik et al., 2000). The N domain, corresponding approximately to the first half of the protein, is much less conserved. The *Erwinia chrysanthemi* exoprotein pectate lyase binds to this region of its cognate secretin, OutD, indicating that it might carry a specific exoprotein recognition determinant (Shevchik et al., 1997). A third secretin domain sometimes present downstream from the C domain (the S domain), interacts with a protein (pilotin) that facilitates secretin targeting to the outer membrane (Daefler et al., 1997a; Daefler et al., 1997b; Lario et al., 2005; Shevchik and Condemine, 1998).

The three dimensional (3D) structures of detergent-solubilized secretins pIV and *N. meningitidis* PilQ were determined by cryo-electron microscopy to resolutions of 18 and 12 Å respectively. The pIV complex is approximately 13.5 nm in diameter and 12 nm deep, and comprises three stacked rings with two large chambers separated by a central protein mass (Opalka et al., 2003). The C- and N domains, identified by labeling specific cysteine residues with nanogold particles, are on opposite rings (Opalka et al., 2003). In contrast, PilQ complexes have a cone-like structure that is closed at the tip (Collins et al., 2001; Collins et al., 2003; Collins et al., 2004b). Individual secretin subunits were not resolved in either structure, but symmetries of 14 (pIV) and 12 (PilQ) were inferred from analysis of the rotational power spectrum (Opalka et al., 2003) and from regular patterns of stain accumulation visible in the reconstituted 3D image (Collins et al., 2003; Collins et al., 2004a), respectively.

The pullulanase T2SS of *K. oxytoca* is one of the most extensively studied secretons and has been completely reconstituted in *E. coli*. A low resolution 3D structure of a purified complex of the pullulanase T2SS secretin PulD and its pilotin, PulS, revealed a cylindrical complex with 12-fold symmetry and a central open channel of about 7 nm encircled by radial spokes that we originally presumed to be the pilotin, which is absent from pIV and PilQ (Nouwen et al., 1999). Here, we report refined biochemical and structural analyses of intact and proteolysed PulD multimers.

3.3 Results

3.3.1 Purification and proteolysis of intact his-tagged secretin multimers

The PulD-PulS complex reported previously by Nouwen et al. (Nouwen et al., 1999) precipitated from ZW3-14 solutions at low temperature and at low salt concentrations, which hampered high-resolution cryo-electron microscopy analysis. To circumvent this problem, we dissociated PulS from PulD without denaturing the latter. To facilitate the purification of PulD alone, a hexahistidine tag was inserted in the S domain of PulD at position

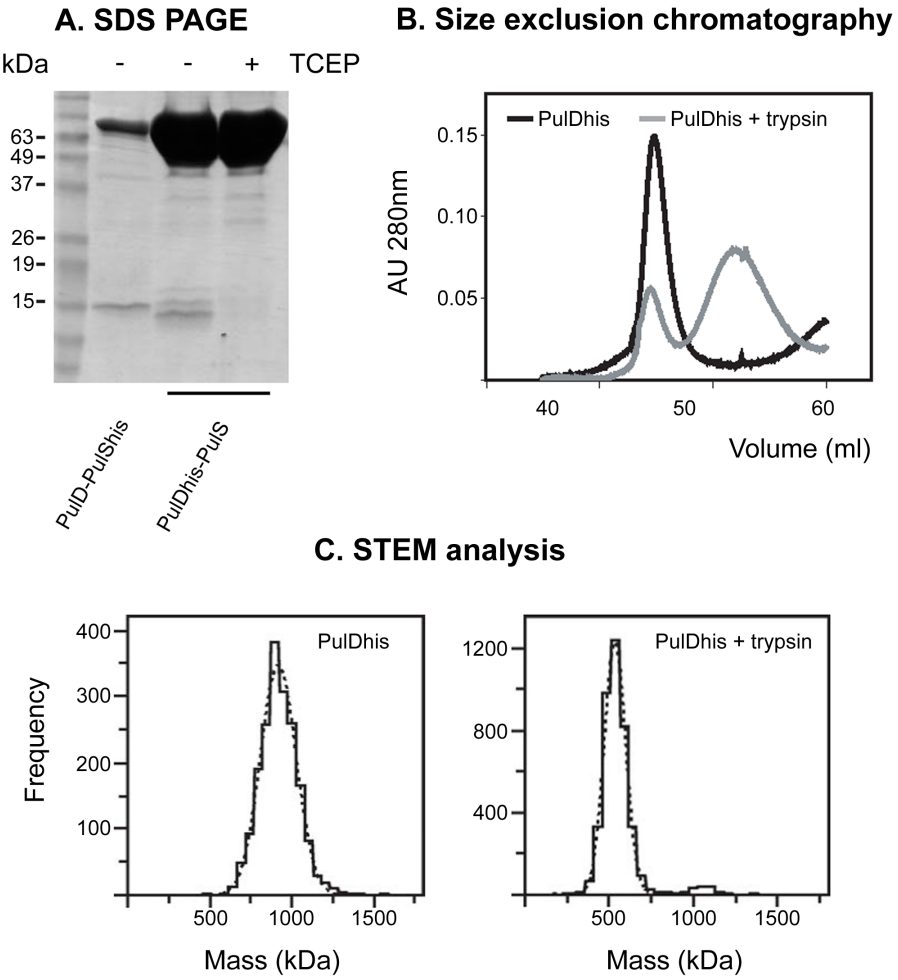

Figure 3.1: **Mass measurement of intact and proteolysed PulDhis.** (A) Coomassie blue stained SDS-PAGE of purified secretin complexes. PulD-PulShis or PulDhis-PulS were purified from *E. coli* outer membranes. TCEP was added before size exclusion chromatography on S300HR and concentration on Q Sepharose. Samples were treated with phenol before solubilization in sample buffer in order to completely dissociate the complex. (B) Intact or trypsin proteolysed PulDhis complexes were subjected to size exclusion chromatography on a calibrated Sephacryl S300HR column in 50 mM Tris-HCl, 250 mM NaCl and 0.6% ZW3-14. (C) STEM mass analysis. The histograms show the mass distributions for the intact and proteolysed PulDhis complexes. The Gaussian is at 919 $\pm$ 109 kDa (n = 1872, SE = 2.5 kDa, overall uncertainty = 46 kDa) for intact PulDhis (left) and at 537 $\pm$ 64 kDa (n = 3906, SE = 1.0 kDa, overall uncertainty = 27 kDa) after trypsin treatment (right). The higher masses on the latter histogram arise from the occasional association of two complexes (see Figure 3.5B).

635 (i.e., in the S domain; see Figure 3.3). The tagged protein, PulDhis, restored pullulanase secretion in a strain lacking PulD but producing all other secreton components (*Experimental procedures*). When produced at high levels together with PulS, PulDhis was readily solubilized from membranes in ZW3-14 and was purified as a high molecular mass complex by cobalt and anion exchange chromatography (*Experimental procedures*). PulS co-eluted with PulDhis but at a stoichiometry of only 0.1:1 (Figure 3.1A), compared to approximately 1:1 for PulS+PulD (Nouwen et al., 1999) or PulShis+PulD (Figure 3.1A), showing that the his tag in the S domain PulD did not prevent it from inserting into the outer membrane but might cause PulS to dissociate. Reduction of the disulfide bridge in PulS (Pugsley et al., 2001) by Tris-[2-carboxyethylphosphine]hydrochloride completely dissociated the remaining PulS from the purified PulDhis complex (Figure 3.1A).

The purified PulD complex and the complex remaining after limited trypsin proteolysis (*Experimental procedures*) were subjected to size exclusion chromatography (Figure 3.1B). The intact complex eluted at 46 ml, corresponding to a Stokes radius of $\geq$12 nm. This is exactly the same elution volume as that of PulD-PulShis or PulD-PulS complexes (data not shown), indicating that the removal of PulS does not drastically modify the shape of the complex. In contrast, the protease-resistant com-

plex eluted at 52 ml, indicating a Stokes radius of ≈9 nm.
STEM mass analysis (Figure 3.1C; left histogram) showed the intact PulDhis complex to have a mass of 919 kDa (±109 kDa). Previous studies of PulD-PulS revealed a stoichiometry of 12 (Nouwen et al., 2000). Assuming that this stoichiometry is unaltered by the removal of PulS and the insertion of a his tag (see below), the PulDhis complex comprises 12 of the 68.745 kDa monomers with a total mass of 825 kDa, the remaining 94 kDa being bound detergent. This is in good agreement with the earlier experiments on purified PulD-PulS complexes, in which the detergent contribution was estimated to be 56 kDa (Nouwen et al., 2000), and with the amount of detergent (75 ± 20 kDa) expected to bind to the hydrophobic surface of the PulD homomultimer (112 nm^2 for a 12 nm diameter (see below), 3 nm thick (Boulanger et al., 1996) hydrophobic belt). STEM analysis showed the mass of the proteolysed complex to be 537 kDa (± 64 kDa; Figure 3.1C; right histogram; see below).
To verify the stoichiometry, both complexes were freeze-etched, metal shadowed and observed by transmission electron microscopy. As expected, the complexes appeared as ring like structures when viewed end-on (Figure 3.2A). Individual protomers were sometimes visible for the proteolysed complex (Figure 3.2B) but not for the intact complex (data not shown), possibly because flexible loops averaged out the signal in the latter. The projection average obtained upon single particle analysis of the metal shadowed proteolysed complex has a pronounced 12-fold symmetry (Figure 3.2C), confirming that the stoichiometry of the complex is not modified by removal of PulS and proteolysis.

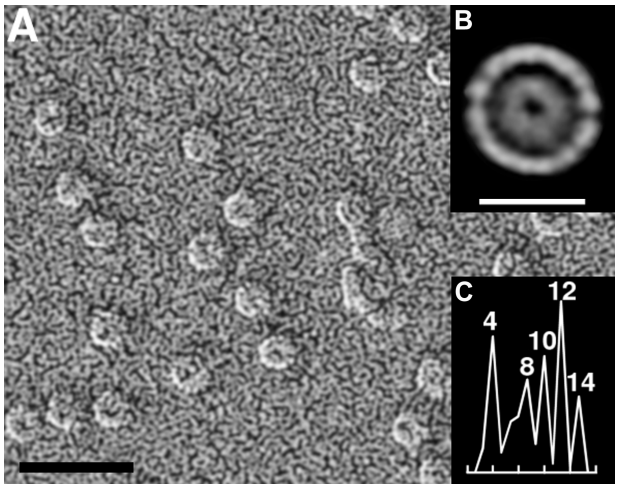

Figure 3.2: **Single particle analysis of top-views imaged from rotary metal-shadowed trypsin-resistant PulDhis complexes.** (A) Overview of rotary metal-shadowed sample. (B) Average of metal-shadowed top views. (C) The rotational power spectrum of a characteristic average indicates the prevailing 12-fold symmetry. The strong 4th harmonic supports an oligomeric state of twelve. Scale bar for (A) is 40nm, for (B) is 10nm.

3.3.2 Polypeptide composition of proteolysed PulDhis

The polypeptide composition of the trypsin-resistant PulDhis multimers was determined by SDS-PAGE, mass spectrometry and Edman degradation analyses. A single band with an apparent molecular size of 40 kDa was observed after Tris-Tricine SDS-PAGE (Figure 3.3A). Successive cycles of Edman degradation indicated that this polypeptide started with QAAK, corresponding to residues 298 to 301 of PulDhis.
Mass spectrometry of proteolysed PulDhis complexes revealed the presence of molecular species with masses of 3950 Da and 33797 Da (F1 and F2, respectively) (Figure 3.3A). No other peaks were detected, indicating complete homogeneity. F2 corresponds to the 40 kDa band seen on SDS-PAGE and thus comprises residues 298 to 617 of PulDhis (calculated mass, 33783 Da). A genetically engineered truncated PulD protein corresponding to residues 298 to 616 of PulDhis also migrated more slowly than expected during SDS-PAGE (data not shown). To identify F1, which was not detected by Tris-Tricine SDS-PAGE, the proteolysed complex was dissociated with phenol (Hardie et al., 1996a) and analyzed by HPLC on a C18 column. Several peptides were detected, recovered and submitted to Edman degradation and mass spectrometry. All of them had a mass of 3950 Da and began with QQAT, corresponding to residues 262 to 265 of PulDhis. The reason why these identical peptides eluted in several peaks from the C18 column is unknown. From the precise mass of the fragment, we unambiguously identified F1 as residues 262 to 297 of PulDhis (calculated mass, 3936 Da). Thus, trypsin removes regions from both the N- and C-termini of PulDhis, leaving a nicked core structure corresponding to residues 262 to 617 (Figure 3.3B). This protease-resistant region, which is called the C domain, is highly conserved in all secretins and comprises the third of three CD1 modules and the CD2 module (see Figure 3.3B for explanation). The C domain corresponds to the β domain defined pre-

viously (Nouwen et al., 2000) plus peptide F1.
According to mass spectrometry, only F1 among the peptides cleaved off by trypsin remained associated with the trypsin-resistant PulDhis complex. Therefore, the latter has a mass of 452.6 kDa (12x[33783+3936]), indicating that 46% of the mass of the secretin is removed by proteolysis. Likewise, the STEM data indicate a mass of 537 kDa for the proteolysed complex (Figure 3.1C; right histogram). The difference of 84 kDa between the value determined by STEM and that calculated from the mass spectrometry data represents the amount of bound detergent, which is very close to that associated with the intact complex (see above). This is entirely consistent with the fact that the C domain includes the membrane-integrated part of the complex, which is presumably where the majority of the detergent binds (see *Discussion*).

3.3.3 Secondary structure of PulDhis

Circular dichroism was used to determine the secondary structure of the trypsin resistant C domain of PulDhis (262 to 617). The proteolysed complex was dialyzed to replace NaCl by NaF so that a reliable signal could be recorded down to a wavelength of 190 nm. As shown in Figure 3.4, the spectrum displays a single minimum at 218 nm. Deconvolution of this spectrum using the CONTIN program on the Dichroweb site (http://www.cryst.bbk.ac.uk/cdweb/html/home.html) (Lobley et al., 2002; Whitmore and Wallace, 2004) indicated that 27% of the polypeptide is β structure. The reconstructed spectrum could be perfectly superimposed on the experimental data (not shown). The presence of β strands is not surprising, since the proteolysed complex is predicted to contain the transmembrane domain, but the value of 27% is low compared to other bacterial integral outer membrane proteins, suggesting that a large part of the C domain is not organized in a classical outer membrane β barrel structure and, therefore, is probably not embedded in the membrane.
We engineered a plasmid coding for the trypsin cleaved N domain of PulD (residues 28 to 266) and an N-terminal polyhistidine tag. This domain was soluble and was easily purified to homogeneity by cobalt affinity chromatography (data not shown). It eluted as a single symmetrical peak corresponding to the monomeric form of the protein upon size exclusion chromatography (data not shown). The CD spectrum of this N domain was substantially different from that of the trypsin resistant C domain, with minima at 208 and 222 nm typical of α helixes (Figure 3.4). The observed difference in the CD spectra of the isolated N- and C domains of PulD clearly indicates the radically different organization of the polypeptide chain in these two regions, confirming that they are two structurally distinct domains.
As noted above, intact PulDhis complexes are very sensitive to NaCl concentration and we could not completely replace NaCl by NaF without precipitating the protein. Thus, we could only record a reliable CD spectrum between 200 and 250 nm and it was not possible to deconvolute this spectrum. However, the spectrum of PulD secretin and the calculated sum of the isolated N- and C domain spectra could be almost perfectly superimposed. Accordingly, the spectra of the isolated N- and C domains reflect their secondary structure in the native protein.

3.3.4 Cryo-electron microscopy of intact and proteolysed PulDhis

When frozen for cryo-electron microscopy, membrane proteins, and in particular secretin complexes, tend to cluster at the edge of the grid holes. To avoid this problem, intact and trypsin-proteolysed PulDhis complexes were adsorbed onto thin carbon films prior to freezing. Both PulDhis and the trypsin-resistant complexes mainly oriented end-on, appearing as ring-like structures with a large central density (Figure 3.5). PulDhis also sometimes oriented on its side, revealing a 'cup and saucer' structure (Figure 3.5A) similar to that observed previously upon negative staining (Nouwen et al., 2000). Occasional side-views dimeric complexes interacting via their saucer side were also observed. Trypsin-proteolysed PulDhis complexes were rarely seen in side-views unless the sample had been left at room temperature before analysis. These side-views were almost always dimers in which the two complexes were associated on their cup side (Figure 3.5B), indicating that the physico-chemical properties of this part of the complex are modified by proteolysis.
A striking common feature of native and trypsin-resistant PulDhis top-views is a sharp ring-shaped density at the edge of the projected cylinder (arrowheads in Figure 3.5 insets). The diameter of this

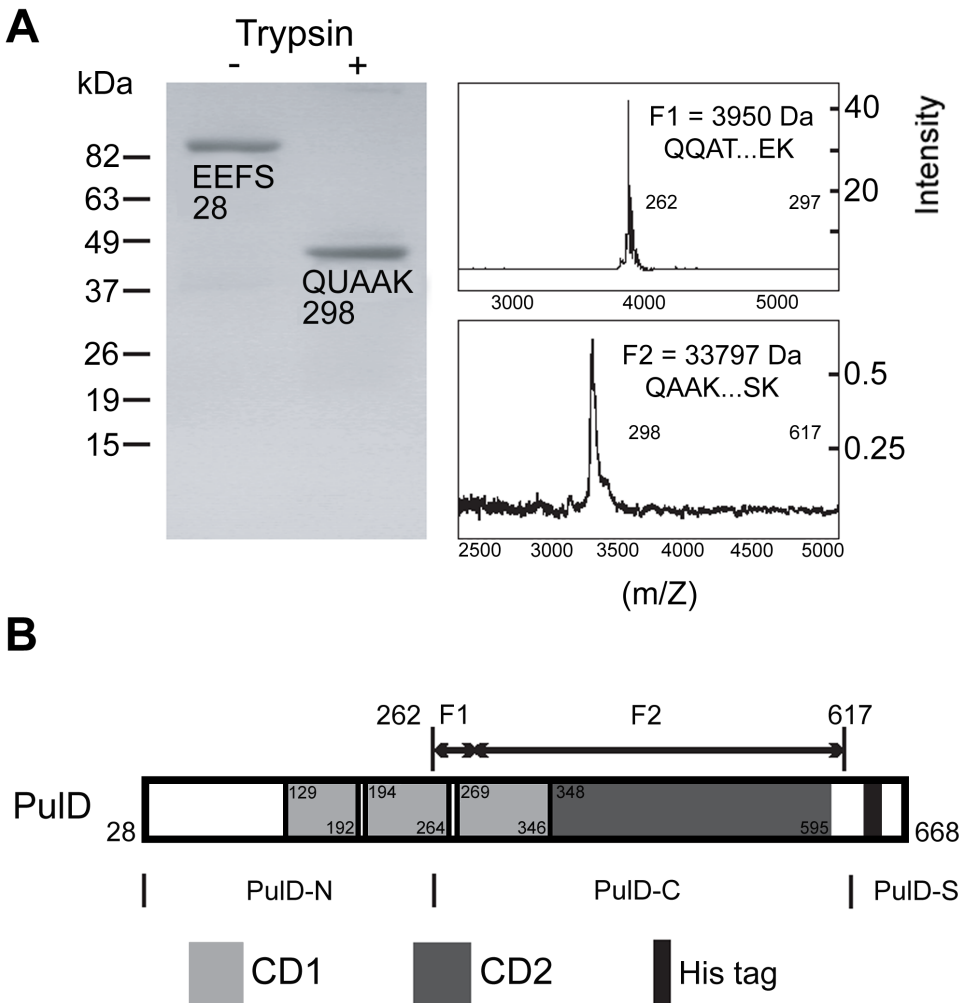

Figure 3.3: **Domain structure of PulDhis revealed by analysis of protease-generated fragments.** (A) Intact and trypsin proteolysed PulDhis recovered from S300HR chromatography were examined by Tris-Tricine-buffered SDS-PAGE after phenol treatment. Proteins were stained with Coomassie blue. No additional bands were detected when proteins were stained with silver. In parallel, the samples were also submitted to mass spectrometry. Two peaks, F1 and F2, corresponding to 3950 and 33797 Da were detected for trypsin proteolysed PulDhis. No signal could be detected with the intact protein. (B) Linear representation of PulDhis sequence is given to localize the trypsin-resistant fragments F1 and F2. PulD-N, PulD-C and PulD-S domains are indicated on the basis of the present proteolysis study. The PulD-C domain includes the CD2 very conserved domain (previously named secretin C-domain) and one CD1 module.

sharp ring of density, 11.9 nm, is the same as the distance between the fine structures that connect the cup and saucer (marked by arrow-heads in the side-view averages shown in Figure 3.5 insets). In addition, native PulDhis complexes possess distinct peripheral densities with a 12-fold rotational symmetry (Figure 3.5A inset). These peripheral densities are missing from proteolysed PulDhis complexes (Figure 3.5B inset). In agreement with these observations, peripheral structures were clearly visible on some of the negatively stained PulDhis complexes imaged by STEM but were not detected on proteolysed samples (Supplementary Figures 3.7 and 3.8).

More than 6000 intact PulDhis complexes were selected interactively from the micrographs recorded by cryo-electron microscopy, reference-free aligned, classified and averaged (see *Experimental procedures*). Characteristic top- and side-view class averages are shown in the insets of Figure 3.5A. The images classified as side views were employed to generate an initial 3D volume, imposing C12 symmetry. Refinement cycles using projection matching of the selected particles with an increasing number of calculated reference projections were repeated until the 3D map did not improve further (Figure 3.6A,B). The resolution of the generated map was estimated to 1.7 nm from the Fourier shell correlation function using a cutoff of 0.5.

Class averages of a total of nearly 3300 top-views

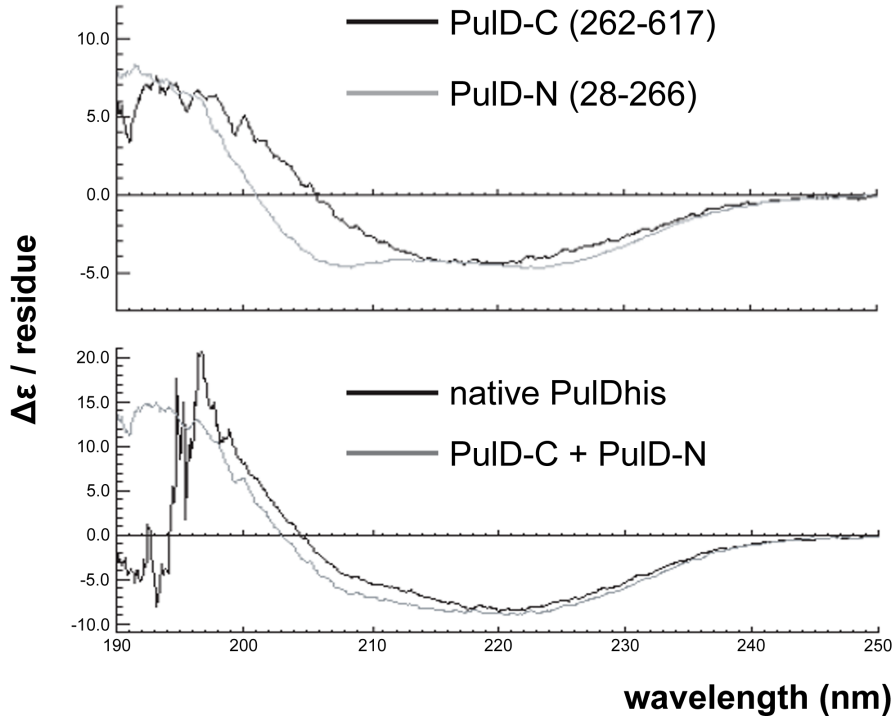

Figure 3.4: **Circular dichroism spectra of PulDhis, PulD-N and PulD-C.** PulD-C is the trypsin resistant domain of PulDhis. PulD-N is a purified polypeptide corresponding to the N terminal half of PulDhis that was cleaved off by proteolysis. The calculated sum of PulD-C and PulD-N CD spectra was superimposed on the CD spectrum of full length PulDhis.

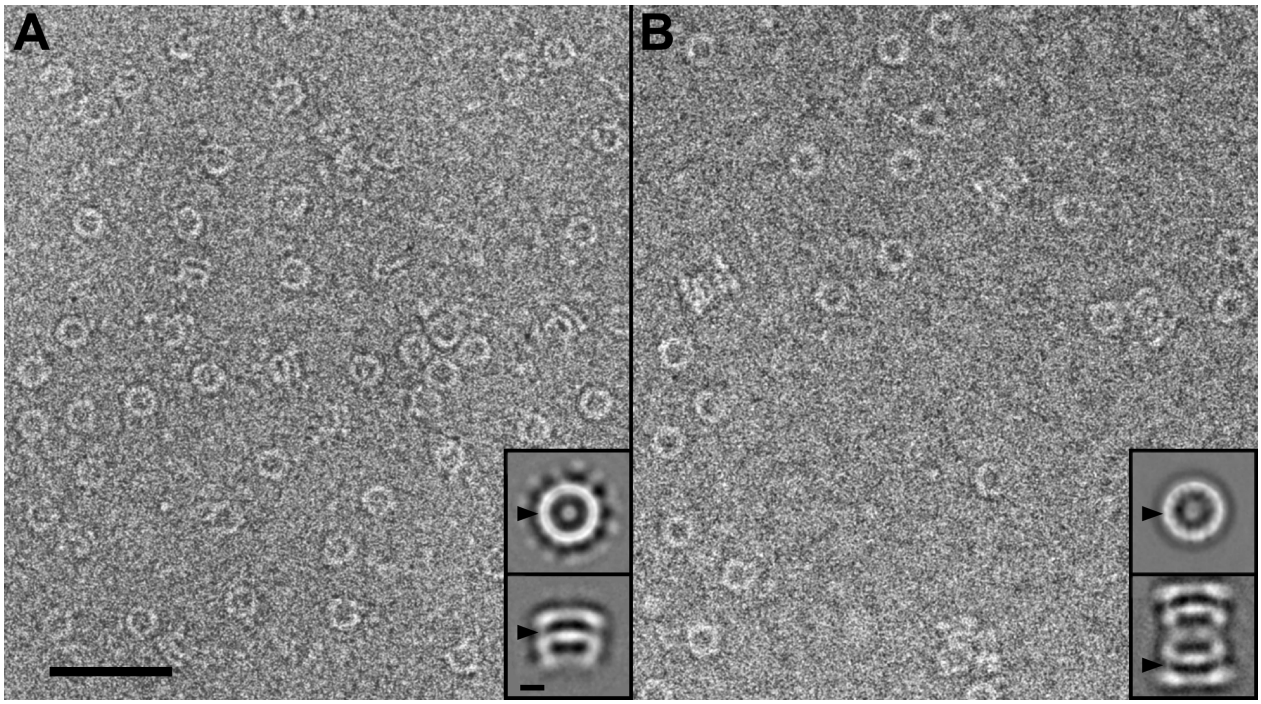

Figure 3.5: **Cryo-electron microscopy of the intact and digested PulDhis complexes.** Overview images of frozen hydrated samples of the intact (A) and trypsin-resistant (B) PulDhis complexes. The insets show characteristic class averages of the native (2489 top-views and 1284 side-views) and proteolysed (3276 top-views 1453 side-views) complexes viewed along the central axis or from the side, the latter revealing the cup and saucer shape (inverted) of the complex. Arrowheads on the side-view averages mark the connections between cup and saucer, which correspond to the sharp rings detected for the top-views. The protruding densities seen in intact PulD are not present after proteolysis. Due to lack of single side-views of the digested complex, only class averages of dimers are shown. The scale bar in the overview corresponds to 50 nm, the scale bar in the small window to 5 nm.

and 1500 side-views of the complex dimer were similarly calculated for the proteolysed PulDhis complex. The inset of Figure 3.5B displays a typical top- and side-view class average. As only approximately 100 side-views of the complex monomer could be found, the 3D map of the proteolysed secretin was computed as the volume of the complex dimer, applying a D12 symmetry, and refined as above. The two reconstructed complexes were then separated and merged (see *Experimental procedures*). The resolution of the final reconstruction (Figure 3.6A,D) could not be reliably determined because the volume was composed from side-views of dimers.

The models of the intact (mesh) and trypsin-resistant (blue) PulDhis complexes are superimposed in Figure 3.6A. The corresponding tilted complexes are displayed in Figures 3.6B and 3.6D. Both the intact and the proteolysed PulD complexes are cylinders with external and maximal internal diameters of around 12 nm and 9 nm, resptively (Table 3.1). The outer contours of the three stacked rings give the two structures a cup and saucer appearance (shown in upside-down orientation in Figure 3.6), one of the three rings being the saucer and the other two, the cup. Connections between saucer and cup are not visible at the current resolution of 1.7 nm, although they are visible on class averages of negatively stained side-views (Nouwen et al., 2000) and on unstained top- and side views (arrowheads in Figure 3.5). While the saucer has a central hole, a plug occludes the saucer end of the chamber formed by the cup. Almost all of these features are smaller after trypsin treatment (Table 3.1), the reduction in the height of the cup from 6.4 to 4 nm being the largest change. This means that trypsin removes the outer ring of the cup, which must therefore be formed by the N-terminal domain of PulDhis, the larger of the two domains that are cleaved off (Figure 3.2). Since the saucer is also shallower in the trypsin-resistant complex, the overall height of the structure decreases from 10.9 to 8 nm. These data suggest that the major contribution to the mass of the plug and the saucer is made by the C domain. The diameter of the saucer also decreases from 17.9 nm to 14.3 nm upon proteolysis through removal of the spoke-like densities. In addition, the peripheral densities that surround the native PulDhis cup disappear completely upon proteolysis. Projections of the 3D maps of the native and the trypsin-resistant PulDhis along the cylinder axis (Figures 3.6C and 3.6E, respectively) facilitate visualization of these differences.

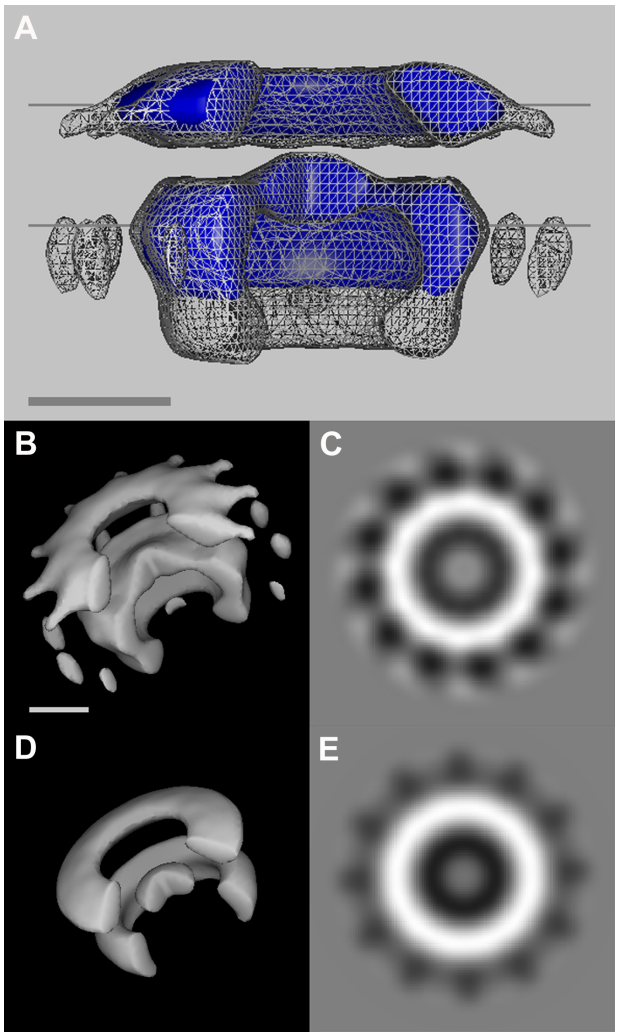

Figure 3.6: **Calculated volumes and back-projections of intact and protease-resistant PulDhis complexes.** (A) Superposition of the 3D reconstruction of the intact complex (white mesh) and of the digested fragment (blue). The horizontal lines represent the outer limits of the lipopolysaccharide/phospholipid outer membrane (approximately 4.5 nm wide). (B) Perspective view of the native PulD complex and (C) the corresponding axial back-projection of the 3D map. (D) Perspective view and (E) axial back-projection of trypsin-resistant PulD complexes. All scale bars correspond to 5 nm, and B-E are displayed at the same magnification.

3.4 Discussion

The model we propose here for the secretin PulD complex is based on biochemical analysis, and cryo-electron microscopy of particles adsorbed from zwitterionic detergent solution onto carbon films.

Domain	Feature measured	Native (nm)	Trypsin-resistant (nm)
Saucer	Outer diameter incl. spokes	17.9	
	Outer diameter excl. spokes	13.7	14.3
	Inner diameter	5.9	6.9
	Height	3.0	2.5
Cup	Outer diameter incl. satellites	18.3	
	Outer diameter excl. satellites	12.8	12.2
	Outer diameter at periplasmic end	11.1	
	Inner diameter cavity max.	8.9	8.9
	Inner diameter at periplasmic end	5.4	7.7
	Height at side	6.4	4.0
	Height center incl. plug	7.1	
Plug	Width	6.5	4.9
	Height	2.6	2.3
Satellites	Width	1.4	
	Height	2.9	
Complex	Total height	10.9	8.0
	Space between cup and saucer	1.1	1.8

Table 3.1: **Dimensions of native and trypsin-resistant PulD complexes.**

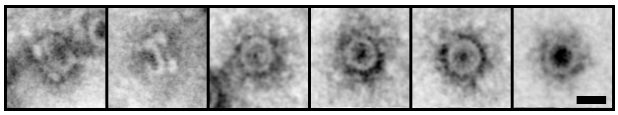

Figure 3.7: Supplementary Figure. **Negatively stained intact PulD complexes imaged by annular dark-field scanning transmission electron microscopy (STEM)**. Side-views exhibit the characteristic cup and saucer shape, while distinct but disordered peripheral densities are visible in the top-views. Scale bar represents 10 nm.

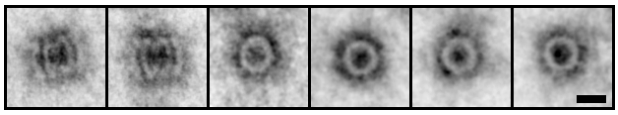

Figure 3.8: Supplementary Figure. **Negatively stained trypsin-resistant C domain PulD complexes imaged by STEM**. Side-views most are mostly dimers of complexes stacked cup-to-cup. Peripheral densities are not visible in the top-views. Scale bar represents 10 nm.

The outer contours give the structure the appearance of a cup and saucer. The essential features of the model are two rings that form large chambers on either side of the complex and a central disc sandwiched between them, including the plug that occludes the channel. This is in good agreement with the model proposed earlier based on images recorded from negatively stained PulD-PulS complexes (Nouwen et al., 2000). The changes caused by proteolysis indicate that the N-terminal domain of PulDhis forms the outer ring of the cup while the C domain forms most of the plug and the saucer with its outer chamber. The overall features of the model are remarkably similar to those proposed for the quite distantly-related bacteriophage f1-encoded secretin pIV in the non-ionic detergent Triton X-100 (Opalka et al., 2003) and for *Salmonella enterica* secretin InvG in purified Type III secretion needle complexes (Marlovits et al., 2004). The major difference between the models proposed for PulD and pIV is that the former is clearly dodecameric, whereas pIV is a tetradecamer (Linderoth et al., 1997; Opalka et al., 2003). STEM analysis gave a mass of 919 kDa for the native PulDhis complex, including the detergent present, thereby exluding the presence of 14 subunits, for which the calculated mass is 962 kDa. Moreover, the PulD complex is highly unlikely to contain 13 subunits like YscC (Burghout et al., 2004), since the detergent contribution would then only be about 25 kDa, which is incompatible with the dimensions of the hydrophobic belt (Boulanger et al., 1996). Changes in stoichiometry might have occurred during the evolution of the secretin superfamily to permit the transport of differently structured macromolecules (bacteriophage, pseudopili or folded exoproteins). Only relatively small changes in subunit dimensions and packing would be required to accommodate a change from 12 to 14

secretin subunits (or vice-versa). A similar scenario was recently proposed to explain the variations in dimensions of TatA complexes isolated from the *E. coli* (Gohlke et al., 2005). These complexes apparently form the channel through which specific folded proteins of varying sizes are translocated across the inner membrane. The TatA complexes might acquire or release protomers to adapt to particular substrates or might exist as a mixed population to enable the entire range of substrates to be accommodated. As with secretins, the number of protomers in the TatA complex is probably so high that addition or subtraction of a small number of TatA monomers would involve minimal distortion of the entire complex.

The apparent structural similarity of the InvG, pIV and PulD complexes makes it all the more remarkable that the structure proposed for *N. meningitidis* PilQ secretin complex is so different (Collins et al., 2004b). Initial electron microscopy of negatively-stained PilQ extracted in deoxycholate that was then replaced by SDS (Collins et al., 2001) or zwitterionic detergent 3-10 (Collins et al., 2003) indicated a ring-like structure similar to that of other secretins in SDS (Collins et al., 2001) and with peripheral densities similar to those of PulD in zwitterionic detergent (Nouwen et al., 1999; Nouwen et al., 2000). However, class averages of side-views of deoxycholate-extracted PilQ complexes dissolved in zwitterionic detergent 3-10 and examined by cryo-electron microscopy after negative staining with ammonium molybdate, revealed that the central density corresponds to the closed aperture at the tip of a cone-like structure (Collins et al., 2004b), rather than the central plug observed for pIV (Opalka et al., 2003) and PulD (this study) or the septum of InvG (Marlovits et al., 2004). The closed aperture in PilQ appears to be the site to which the type IV pilus binds (Collins et al., 2005). Although it is not inconceivable that different secretins might assemble into different structures, we note that the primary sequences of PulD and PilQ are more closely related than are those of PulD and pIV. In addition, although normally dedicated to pullulanase secretion, PulD can perform the same function as PilQ, i.e., the assembly of surface pili (Sauvonnet et al., 2000; Vignon et al., 2003) including a pilus normally produced by *Neisseria* (Köhler et al., 2004).

The central plug is a major, newly defined feature of the PulD complex (Figure 3.6). The plug was not apparent in the previous 3D model (Nouwen et al., 1999) but was observed on later, negatively stained samples (Nouwen et al., 2000). Its presence is consistent with the failure of PulD to form constitutively open channels (Guilvout et al., 1999; Nouwen et al., 1999). The fact the major contribution to the mass of the plug is made by the C domain, and not by the N domain as originally proposed (Nouwen et al., 2000), explains why the low electrical conductance of the PulD homologue XcpQ in artificial planar bilayers does not increase when the N domain is removed by proteolysis (Brok et al., 1999). In addition, mutations in secretin structural genes that alter the permeability of the outer membrane invariably map to the region encoding the C domain (Chen et al., 2004; Marciano et al., 2001; Marciano et al., 1999; Zhao et al., 2005). Fine connections presumably anchor the central plug to the perimeter of the cup in proteolysed PulD complex. Our failure to visualize the plug in the previous model (Nouwen et al., 1999) might be explained by differences in preparation and analytical methods. It is worth noting that the mechanism by which the secretin channel is occluded is completely different from that used to prevent the uncontrolled movement of solutes through TonB-dependent outer membrane transporters, where the N-domain constitutes the plug (Ferguson et al., 1998).

The structural changes caused by proteolysis allow the membrane orientation of the PulD complex to be predicted. The N domain, corresponding mostly to rim of the cup that disappears upon proteolysis, must face the periplasm to perform its proposed function in exoprotein recognition (Shevchik et al., 1997). The location of this domain at one end of the secretin is in line with gold labeling experiments performed with pIV (Opalka et al., 2003). The secretin N domain forms the outer part of a large chamber into which macromolecules (e.g., exoproteins or filamentous bacteriophages) might insert before they are transported across the outer membrane. Exoprotein docking to this site might cause displacement of the plug to create a continuous channel that would remain blocked by the exoprotein during its translocation. Assembly of pseudopilins into a pseudopilus that reaches the cup of the secretin might provide the driving force to expel the exoprotein from the inner chamber (Köhler et al., 2004; Vignon et al., 2003). Exoprotein release and pseudopilus retraction would allow the plug to reform and the channel to close. A similar model explains the opening of InvG secretin channel to allow the assembly of the type III secretion sys-

tem needle, except that the septum does not close again once it is opened (Marlovits et al., 2004).
Another striking feature of both PulD complexes that is clearly seen on specific class averages of top-views is a sharp but faint ring-shaped density at the periphery of the cylinder (marked by arrowheads in Figure 3.5, insets). This corresponds to the fine connections present between cup and saucer in side-views, but is not seen in the final 3D map (Figure 3.6). Their absence in the latter is explained by the limited resolution of the 3D map (1.7 nm), which results from using all projections to reconstruct the volume, rather than considering specific top- and side views only. Bound detergent, not visible on the images (the ZW3-14 detergent used has a density close to 1 (Ariel Lustig, personal communication), could explain why this region was not proteolysed. Accordingly, these fine connections could reflect the β barrel inferred from CD spectra and indicate the position of the lipid bilayer. Indeed, a small number of β strands from each monomer would suffice to form a large ring structure, as in the integral outer membrane region of the *E. coli* protein TolC trimers (Koronakis et al., 2000) or the *Mycobacterium tuberculosis* outer membrane porin MspA (Faller et al., 2004).
If the β strands are indeed located in between the cup and saucer parts of the structure, some of the saucer ($\approx$1.5 nm, see Figure 3.6A) would be on the outside of the outer membrane, possibly even reaching beyond the lipopolysaccharide and other outer layers of the cell. The disc and outer ring of the cup would extend $\approx$5 nm into the periplasm, which would leave sufficient space for exoproteins to enter its inner chamber. An alternative model where the ring corresponding to the saucer is fully embedded in the outer membrane, with little structure exposed on the cell surface, as proposed for pIV (Opalka et al., 2003) is inconsistent with the relatively low amount of β strand secondary structure in the C domain of PulD (27%). It would also be inconsistent with irregular outer wall of the saucer (note the lateral projections in Figure 3.6), around which the outer membrane lipids would not fit snugly. Furthermore, this model would imply that the rest of the structure extends through the periplasm almost to the inner membrane, which might make it difficult for exoproteins to access the inner chamber.
Peripheral protein mass first observed in PulD-PulS complexes (Nouwen et al., 1999; Nouwen et al., 2000) imaged by negative staining and by cryo-electron microscopy was proposed to represent PulS bound to the periphery of the PulD complex because it was almost completely absent from top-views of negatively stained, trypsin-digested PulD-PulS particles (which lack PulS and the S domain of PulD, as well as the N domain) (Nouwen et al., 2000). However, as shown by Figures 3.5 and 3.6, similar peripheral objects (termed peripheral densities) are also associated with native PulDhis complexes without PulS. Thus, the earlier assignment was not quite correct; the peripheral densities do not correspond solely to PulS, as proposed, but must also contain a small amount of PulD. Both the spokes of the saucer and the peripheral densities disappear upon trypsin treatment (Figures 3.5B and 3.6E) and are not visible on top-views of negatively stained particles of trypsin-resistant PulDhis observed by STEM (Supplementary Figures 3.7 and 3.8). Since the larger cleaved domain must correspond to the N-terminal region (see above), the peripheral densities could be the S domains, which would be compatible with a mass loss of $\approx$6 kDa (Figure 3.3), and would place them close to the periplasmic face of the outer membrane, in which PulS is probably anchored by its fatty acids (Hardie et al., 1996a; Hardie et al., 1996b).
The data and refined model presented here indicate that the trypsin-resistant C domain is a substantial part of the periplasmic structure of the secretin complex. It could form a basic core structure required for stable multimerization and interaction with other envelope components such as lipopolysaccharide and peptidoglycan. This leads us to propose that the C domain, which is more highly conserved throughout the secretin superfamily than the N domain, is a scaffold onto which different functions have been grafted through evolution of the N domain. In the case of the T2SS secretin family, these functions could include interactions with the exoproteins (Shevchik et al., 1997), with the pseudopilus (Lee et al., 2005) and with other secreton components such as PulC or its homologues (Baichwal et al., 1993; Bleves et al., 1999; Lee et al., 2005; Possot et al., 1999).

Plasmid	Antibiotic resistance	Vector	Cloned gene(s), mutation	*lac*Zp control	Reference
pCHAP1226	Ap/Km	pBR322	pCHAP231 Δ*pulD pulB*::kan1	–	d'Enfert et al., 1987 Possot et al., 2000
pCHAP3516	Km	pBGS18	*pulD*	+	Shevchik et al., 1998
pCHAP3635	Cm	pSU18	*pulD*	+	Guilvout et al., 1999
pCHAP3676	Km	pBGS18	*pulDhis*	+	This study
pCHAP3678	Cm	pSU18	*pulDhis*	+	This study
pCHAP3702	Ap	pET-15b	*pulD-N*	–	This study
pCHAP585	Ap	pUC19	*pulS*	+	Guilvout et al., 1999
pCHAP580	Cm	pSU19	*pulS*	+	Guilvout et al., 1999
pCHAP5506	Ap	pUC19	*pulShis*	+	This study

Table 3.2: **Plasmids.** Km kanamycin; Cm chloramphenicol; Ap ampicillin

3.5 Experimental procedures

3.5.1 Bacterial strains and growth conditions

The *E. coli* strains PAP105 (Δ(*lac-pro*) F'(*lacI*^{q1} *proAB*$^{+}$ *Tn10*) and XL1-Blue (Δ*lacZM15 recA1 endA1 gyrA96 thi hsdR17 glnV44 relA1* F'(*lacI*^{q1} *proAB*$^{+}$ *Tn10*) were used for recombinant DNA work. *E. coli* strain BL21(DE3) (F^{-} *ompT hsdS*$_B$ *gal dcm*) was used to produce the PulD N domain. The principal characteristics of the plasmids used in this study are summarized in Table 3.2. Bacteria were grown at 30°C in Luria-Bertani (LB) medium (Miller, 1992) containing chloramphenicol (25 μg/ml), ampicillin (100 μg/ml, except where noted) or kanamycin (50 μg/ml).

3.5.2 Construction of PulDhis and PulShis

To create PulDhis, a his linker made by annealing oligonucleotides 5'-GATCCATCACCATCACCATCACGC-3' and 5'-GATCGCGTGATGGTGATGGTGATG-3' was introduced into the BglII site in *pulD* carried by pCHAP3516 (Daefler et al., 1997a). The resulting plasmid was digested with EcoRI and HindIII and the fragment corresponding to *pulDhis* was ligated into pSU18 (Bartolomé et al., 1991) and cleaved by the same enzymes to create pCHAP3678. The ability of PulDhis to replace PulD was tested in a pullulanase enzymatic assay (Michaelis et al., 1985) using strain PAP105 carrying pCHAP1226 (encoding all Pul secretion factors except PulD (Possot et al., 2000)). Bacteria were grown in LB medium buffered with 10% M63 salts solution (Miller, 1992) and 0.4% maltose to induce expression of genes encoding pullulanase secretion factors. pCHAP3678 restored secretion to 83% of the wild-type level.

PulShis was constructed by amplifying *pulS* using pCHAP585 template DNA (Guilvout et al., 1999) and reverse M13 sequencing primer and the primer 5'-ATCGAAGCTTTTAGTGATGGTGATGGTGATGGTGATGTTTATTGTCGCGCAGGC-3', which inserts codons for 8 histidines at the 3' end of the amplicon. The amplicon was digested with HindIII and inserted in pSU19 (Bartolomé et al., 1991) to generate pCHAP5506. The sequence of the entire gene was confirmed by sequencing. The ability of PulShis to replace PulS was tested as above in strain PAP7500S (Δ(*lac-argF*)*U169 araD139 relA1 rpsL150* Δ*malE444 malG501* F'(*lacI*^{q1} *pro*$^{+}$ *Tn10*) *malP*::(*pulS*::Tn*5 pulA-pulB pulC-pulO*) into which pCHAP5506 was introduced. PulShis restored secretion to 100% of the wild-type level.

3.5.3 Construction and purification of PulD-N

To construct a plasmid encoding the N-domain of PulD, primers 5'-AGCTGCCATATGGAAGAGTTTTCCGCCAGCTTC-3' and 5'-TACGGCGGATCCTACTGGGTCGCCTGCTGGCGGTCGAGCT-3' were used to PCR amplify the corresponding DNA from pCHAP3635 (Guilvout et al., 1999) template DNA. The amplicon was digested by NdeI and BamHI at sites introduced by the oligonucleotides and cloned downstream from the T7-derived promoter in-frame with DNA encoding the N-terminal histidine tag and the thrombin proteolysis site in pET-15b (Novagen) cleaved with the same restriction enzymes. The *pulD-N* fragment in the resulting plasmid, pCHAP3702, was

sequenced to confirm the absence of mutations.
Strain BL21(DE3) (pCHAP3702) was grown overnight in LB medium and then diluted 1/10 into fresh medium with 200 μg/ml ampicillin. When the OD_{600} reached 0.6, the T7 RNA polymerase gene transcribed from the *lac*UV5 promoter was induced by addition of isopropyl-β-D-galactopyranoside (IPTG) to a final concentration of 0.25 mM and incubated for a further 3 hours. The cells were then harvested and resuspended in 50 mM Tris-HCl (pH 8) containing 250 mM NaCl and 0.2 mg/ml Pefablock. Cells were disrupted in a French pressure cell (Nouwen et al., 1999). Soluble proteins, including most of the PulD N-domain produced, were separated from unbroken cells and inclusion bodies by 2 successive centrifugations (10 min, 15000g) and subjected to cobalt affinity chromatography as above except that the buffer did not contain detergent. After washing with 30 volumes of buffer, the bound N-domain of PulD was eluted with 300 mM imidazole and further purified on a Sephacryl S300HR column equilibrated in 50 mM Tris-HCl, pH 8.5, 250 mM NaCl. The protein eluted from the column as a single major peak that had almost the same elution volume as carbonic anhydrase (29 kDa). Antibodies directed against PulD recognized the protein in this peak.

3.5.4 Purification of secretins

Outer membranes were isolated from PAP105 (pCHAP3516/pCHAP5506) and PAP105 (pCHAP-3678/pCHAP585) producing PulD and PulShis or PulDhis and PulS, respectively as described previously (Nouwen et al., 1999). Membrane proteins were solubilized in 50 mM Tris-HCl (pH 7.5) containing 3% *n*-Tetradecyl-*N,N*-dimethyl-3-ammonio-1-propanesulfonate (ZW3-14), 250 mM NaCl and 0.1 mg/ml of the protease inhibitor Pefablock (Pierce) and incubated for one hour at room temperature. Solubilized proteins were recovered after ultracentrifugation at 185000 x g and mixed with cobalt agarose resin (Talon, Clontech) previously equilibrated in 50 mM Tris-HCl pH 7.5, 0.6% ZW3-14, 250 mM NaCl (TZN buffer) containing 5 mM imidazole for 1 hour at 20°C. The resin was washed with 10 volumes of TZN buffer + 5 mM imidazole and then poured into a column. Bound proteins were eluted with 5 column volumes of TZN buffer containing 5 mM EDTA and immediately loaded onto a HiTrap Q HP column (1 ml) (Amersham Biosciences) connected to an ÄKTAprime system (Amersham Biosciences) at a flow rate of 0.1 ml/min. After extensive washing, secretin complexes were eluted using a linear gradient of 250 mM to 1.25 M NaCl. In order to completely dissociate PulS from the complex, the fractions containing PulD (eluted at 700-750 mM NaCl) were incubated with 50 mM of the reducing agent Tris[2-carboxyethylphosphine] hydrochloride (TCEP; Pierce) for 2 hours at 20 °C. PulS was separated from the PulDhis complex by gel filtration on Sephacryl S300HR. The absence of PulS in the PulDhis fractions was confirmed by immunoblotting using antibodies directed against MalE-PulS. The fractions were concentrated on Q Sepharose and stored in 100 μl aliquots at -80°C.

3.5.5 Trypsin proteolysis of PulDhis secretin

100 μg of purified PulDhis complex (0.1 mg/ml) was incubated with 10 μg/ml *N-p*-Tosyl-L-phenylalanine chloromethyl ketone-treated trypsin (Sigma) for 2 hours at 18°C. Pefabloc was then added to 0.1 mg/ml and the sample was immediately injected onto a Sephacryl S300HR column. A control experiment was performed under the same conditions except that the trypsin was omitted. In both cases, aliquots from all fractions were treated with phenol to dissociate the PulD complexes (Hardie et al., 1996a) and then analyzed by SDS-PAGE. The Sephacryl S300HR column was calibrated using thyroglobulin, alcohol dehydrogenase, bovine serum albumin and carbonic anhydrase. PulD-containing fractions were concentrated and stored in 50 μl aliquots at -80°C for electron microscopy.

3.5.6 Electrophoresis, immunoblotting and protein sequencing

Denaturing SDS-PAGE was performed in a Miniprotean II^{TM} system (BioRad) with 3.2% acrylamide stacking gel and 10 or 12% acrylamide separating gels using Tris-glycine-HCl buffers. Tris-Tricine buffered 10-20% acrylamide gradient gels (BioRad) were used to analyze trypsin proteolysed PulDhis in an attempt to detect small peptides. In all cases, the multimeric secretin complexes were dissociated by phenol extraction (Hardie et al., 1996a) and resuspended in sample buffer (100 mM Tris-HCl (pH 8.0), 12.5% glycerol, 2.5% SDS).

Proteins separated by electrophoresis were stained with Coomassie brilliant blue or silver nitrate. For immunoblotting, proteins were electrophoretically transferred onto nitrocellulose sheets in a semi-dry apparatus. PulDhis was detected either by antibodies directed against PulD (d'Enfert et al., 1989; Hardie et al., 1996a) or with the Hisprobe^{TM}-HRP (Pierce). PulShis was detected with antibodies directed against MalE-PulS (Hardie et al., 1996b). Bound primary antibodies were then reacted with horseradish-peroxidase-coupled donkey anti rabbit IgG (Amersham Biosciences) and the immunoblots developed by enhanced chemiluminescence. For automated sequencing on an Applied 494 sequencer, proteins were transferred from acrylamide gels onto PVDF membranes (Immobilon-P^{SQ}, Millipore).

3.5.7 Circular dichroism analysis

Circular dichroism (CD) spectra were recorded from 190 to 250 nm on a JASCO dichrograph (J-710) equipped with a thermostatically controlled cell holder and connected to a computer for data acquisition. Purified PulD-N at 100 μg/ml was dialyzed against 1 mM Tris-HCl (pH 8) containing 250 mM NaF and submitted to CD analysis in a 1 mm quartz cell (3 data sets were acquired). The PulD-C domain was dialyzed against 1 mM Tris-HCl (pH 7.5) containing 250 mM NaF and 0.6% ZW3-14 immediately prior to analysis in a 5 mm quartz cell at a final concentration of 10 μg/ml (5 data sets were acquired). Purified PulDhis at 60 μg/ml in 50 mM Tris-HCl (pH 7.5) containing 250 mM NaCl and 0.6% ZW3-14 was diluted twice in 500 mM NaF containing 0.6% ZW3-14 immediately before CD analysis in a 1 mm quartz cell (5 data sets were acquired).

3.5.8 Peptide analysis by HPLC, sequencing and mass spectrometry

SPeptides were separated in a 0-70% acetonitrile gradient in 0.1% trifluoroacetic acid by HPLC on a 1x150 mm C18 column (Interchim UP90DBD15). Samples were collected and frozen until they were sequenced on an Applied 494 sequencer or subjected to mass spectrometry using SELDI-TOF MS (Ciphergen). The matrix for the latter was alpha-cyano-4-hydroxy cinnamic acid and 2 μl samples were loaded onto the gold ProteinChip array.

3.5.9 Scanning transmission electron microscopy

A Vacuum Generators (East Grinstead) HB-5 STEM, interfaced to a modular computer system (Tietz Video and Image Processing Systems), was used. Samples were prepared on 200-mesh-per-inch, gold-plated copper grids as previously (Müller et al., 1992). Grids were washed on 5-7 droplets of quartz double-distilled water to remove detergent. Isolated tobacco mosaic virus particles (kindly supplied by R. Diaz-Avalos) adsorbed to a separate grid and air-dried, served as the mass standard.
For structural examination, digital 512x512 pixel dark-field images were recorded from negatively stained (2% uranyl acetate) PulD at an acceleration voltage of 100 kV and a nominal magnification of 500kx using doses between 3450 and 10250 electrons/nm. The pixel size ($\approx$0.33 nm) depended on the focus conditions (Müller et al., 1992).
For mass determination, digital 512 x 512 pixel dark-field images were recorded from unstained freeze-dried samples of the PulD complexes at an acceleration voltage of 80 kV and a nominal magnification of 200kx. The recording dose used varied between 295 and 640 electrons/nm^2 for these main data sets. In addition, repeated low-dose scans were recorded from some grid regions to assess beam-induced mass-loss (Müller et al., 1992). The images were evaluated with the IMPSYS program package as described previously (Müller et al., 1992). Complexes were delimited by circles, the total mass calculated and the background subtracted. The beam-induced mass-loss was assessed as previously (Müller et al., 1992). The experimental mass data were multiplied by the correction factors calculated for the recording doses used and scaled according to the MPL measured for TMV particles. Finally, they were binned into histograms and fitted with Gauss curves. The overall experimental uncertainty of the results was estimated from the corresponding SE (SE = SD/$\sqrt{n}$) and the 5% uncertainty in the calibration of the instrument by calculating the square root of the sum of the squares.

3.5.10 Metal shadowing

A 5 μl aliquot of purified sample at 0.05 mg/ml was applied to copper grids covered with a thin carbon film of uniform thickness, blotted with Whatman 2 filter paper, washed with 5 droplets of water to remove excess detergent and quick-frozen in liquid

ethane at -178 °C. The frozen grids were transferred into a Balzers 300 freeze-etching unit and freeze-dried at -90°C for 5 hours in a vacuum of approximately 1.3x10^{-5} Pa. Platinum/Carbon (1 to 2 nm-thick) was evaporated onto the surface at an angle of 45° while the sample was rotating. Images were taken on Kodak SO-163 film at a nominal magnification of 50kx with a Hitachi 7000 electron microscope operating at an accelerating voltage of 100 kV. The film was digitized at 4 Å/pixel with a Primescan D 7100 drum scanner (Heidelberger Druckmaschinen AG). EMAN boxer (Ludtke et al., 1999) was used to interactively select 1300 particles. Neural network-based classification, averaging and calculation of the rotational power spectra (Crowther and Amos, 1971) was done using the Xmipp (Marabini et al., 1996) software package.

3.5.11 Cryo-electron microscopy and single particle analysis

A 5 μl aliquot of purified sample at 0.05 mg/ml was applied to thin carbon film mounted on copper grids, washed with 5 droplets of water to remove excess detergent and then quick-frozen in liquid ethane at -178 °C. The frozen grids were transferred to a Philips CM200-FEG electron microscope using a Gatan cryo-holder. Images were recorded on Kodak SO-163 film at a nominal magnification of 50kx and an accelerating voltage of 200 kV under low-dose conditions. The defocus of the micrographs ranged between 2.4 μm and 5.1 μm. The negatives were digitized at 2 Å/pixel with a Primescan D 7100 drum scanner.

Particles were selected interactively from the images with the EMAN boxer (Ludtke et al., 1999) software and analysed using the SPIDER image processing programs (Frank et al., 1996). Reference-free alignment (Penczek et al., 1992) and classification by correspondence analysis was employed to generate class averages. These were then used as references for iterative multi-reference alignment, the cycles of alignment and classification being repeated until no further change was observed in the class averages.

For the intact complex, the various side-views were utilized to generate a rough starting model by a common line search varying only one Euler angle. A cyclic 12-fold symmetry (C12) was imposed for the starting model, which was refined by projection matching of the top and side-views while still imposing the C12 symmetry for the final volume. Several cycles of projection matching with increasing numbers of reference projections followed by iterative back projection in real space were required to obtain the final volume. All particle views were included in the refinement and matched to evenly balanced projections covering the whole 3D space. The mandatory contrast-transfer function (CTF) correction at the defocus values employed was made by a Wiener filter using a combination of the MRC (Crowther et al., 1996) and SPIDER (Frank et al., 1996) software suites. The resolution of the generated map was estimated from the Fourier shell correlation function using a threshold of 0.5.

Since practically only dimers of side-views of the proteolysed PulDhis complexes were available, a first volume of the dimer was computed and refined, imposing a dihedral twelve-fold symmetry (D12) throughout. The two reconstructed complexes were then separated and merged; the average of the few complex monomer side-views available was used to measure the dimensions of the fragment in order to obtain a clean separation of the two, thereby eliminating symmetrization artifacts at the interface. The CTF was corrected as above.

3.6 Acknowledgements

We thank Jacques d'Alayer (Platform de Microséquençage, Institut Pasteur) for peptide purification, microsequencing and mass spectrometry, Gilles Craescu for use of the circular dichroism facility at the Institut Curie (Orsay, France), Eric Larquet for preliminary electron microscopy of PulD, Dominique Vidal-Ingigliardi for computer analyses, Philippe Ringler and Françoise Erne for the STEM microscopy, Nicolas Boisset for advice on image analysis and members of the Molecular Genetics Unit of the Institut Pasteur for their interest and support.

This work was supported in part by a research and training grant from the European Commission (HPRN-CT-2000-00075), by Swiss National Foundation grant NF 31-59 415.99 to A.E., the Maurice E. Müller Foundation of Switzerland and by the Université de Paris Sud.

3.7 References

Baichwal, V., Liu, D. and Ames, G.F.-L. (1993) The ATP-binding component of a prokaryotic traffic ATPase is exposed to the periplasmic (external) surface. Proc. Natl Acad. Sci. USA, 90, 620-624.

Bartolomé, B., Jubete, Y., Martinez, E. and de la Cruz, F. (1991) Construction and properties of a family of pACYC184-derived cloning vectors compatible with pBR322 and its derivatives. Gene, 102, 75-78.

Bitter, W., Koster, M., Latijnhouwers, M., de Cock, H. and Tommassen, J. (1998) Formation of oligomeric rings by XcpQ and PilQ, which are involved in protein transport across the outer membrane of *Pseudomonas aeruginosa*. Mol. Microbiol., 27, 209-219.

Bleves, S., Gérard-Vincent, M., Lazdunski, A. and Filloux, A. (1999) Structure-function analysis of XcpP, a component involved in general secretory pathway-dependent protein secretion in *Pseudomonas aeruginosa*. J. Bacteriol., 181, 4012-4019.

Boulanger, P., le Maire, M., Bonhivers, M., Dubois, S., Desmadril, M. and Letellier, L. (1996) Purification and structural and functional characterization of FhuA, a transporter of the *Escherichia coli* outer membrane. Biochemistry, 35, 14216-14224.

Brok, R., Van Gelder, P., Winterhalter, M., Ziese, U., Koster, A.J., de Cock, H., Koster, M., Tommassen, J. and Bitter, W. (1999) The C-terminal domain of the Pseudomonas secretin XcpQ forms oligomeric rings with pore activity. J. Mol. Biol, 294, 1169-1179.

Burghout, P., Van Boxtel, R., Van Gelder, P., Ringler, P., Muller, S.A., Tommassen, J. and Koster, M. (2004) Structure and Electrophysiological Properties of the YscC Secretin from the Type III Secretion System of *Yersinia enterocolitica*. J Bacteriol, 186, 4645-4654.

Chen, C., Tobiason, D.M., Thomas, C.E., Shafer, W.M., Seifert, H.S. and Sparling, P.F. (2004) A mutant form of the *Neisseria gonorrhoeae* pilus secretin protein PilQ allows increased entry of heme and antimicrobial compounds. J Bacteriol, 186, 730-739.

Collins, R.F., Davidsen, L., Derrick, J.P., Ford, R.C. and Tonjum, T. (2001) Analysis of the PilQ secretin from *Neisseria meningitidis* by transmission electron microscopy reveals a dodecameric quaternary structure. J Bacteriol, 183, 3825-3832.

Collins, R.F., Ford, R.C., Kitmitto, A., Olsen, R.O., Tonjum, T. and Derrick, J.P. (2003) Three-dimensional structure of the *Neisseria meningitidis* secretin PilQ determined from negative-stain transmission electron microscopy. J. Bacteriol., 185, 2611-2617.

Collins, R.F., Frye, S.A., Balasingha, S., Ford, R.C., Tonjum, T. and Derrick, J.P. (2005) Interaction with type IV pili induces structural changes in the bacterial outer membrane secretin PilQ. J. Biol. Chem., 280, 18923-18930.

Collins, R.F., Frye, S.A., Kitmitto, A., Ford, R.C., Tonjum, T. and Derrick, J.P. (2004a) Structure of the *Neisseria meningitidis* outer membrane PilQ secretin complex at 12 A resolution. J Biol Chem, 279, 39750-39756.

Collins, R.F., Frye, S.A., Kitmitto, A., Ford, R.C., Tonjum, T. and Derrick, J.P. (2004b) Structure of the *Neisseria meningitidis* outer membrane PilQ secretin complex at 12 A resolution. J Biol Chem, 279, 28227-28232.

Crowther, R.A. and Amos, L.A. (1971) Harmonic analysis of electron microscope images with rotational symmetry. J. Mol. Biol., 60, 123-130.
Crowther, R.A., Henderson, R. and Smith, J.M. (1996) MRC image processing programs. J. Struct. Biol., 116, 9-16.

d'Enfert, C., Reyss, I., Wandersman, C. and Pugsley, A.P. (1989) Protein secretion by Gram-negative bacteria: characterization of two membrane proteins required for pullulanase secretion by *Escherichia coli* K-12. J Biol Chem, 264, 17462-17468.

d'Enfert, C., Ryter, A. and Pugsley, A.P. (1987) Cloning and expression in Escherichia coli of the *Klebsiella pneumoniae* genes for production, surface localization and secretion of the lipoprotein pullulanase. EMBO J, 6, 3531-3538.

Daefler, S., Guilvout, I., Hardie, K.R., Pugsley, A.P. and Russel, M. (1997a) The C-terminal domain of the secretin PulD contains the binding site for its cognate chaperone, PulS, and confers PulS dependence on pIVf1 function. Mol. Microbiol, 24, 465-475.

Daefler, S., Russel, M. and Model, P. (1997b) Module swaps between related translocator proteins pIVf1, pIVIKe and PulD: identification of a specificity domain. J Mol Biol, 266, 978-992.

Faller, M., Niederweis, M. and Schulz, G.E. (2004) The structure of a mycobacterial outer-membrane channel. Science, 303, 1189-1192.

Ferguson, A.D., Hofmann, E., Coulton, J.W., Diederichs, K. and Welte, W. (1998) Siderophore-mediated iron transport: crystal structure of FhuA with bound lipopolysaccharide. Science, 282, 2215-2220.

Frank, J., Radermacher, M., Penczek, P., Zhu, J., Li, Y., Ladjadj, M. and Leith, A. (1996) SPIDER and WEB: processing and visualization of images in 3D electron microscopy and related fields. J Struct Biol, 116, 190-199.

Gohlke, U., Pullan, L., McDevitt, C.A., Porcelli, I., de Leeuw, E., Palmer, T., Saibil, H.R. and Berks, B.C. (2005) The TatA component of the twin-arginine protein transport system forms channel complexes of variable diameter. Proc Natl Acad Sci U S A, 102, 10482-10486.

Guilvout, I., Hardie, K.R., Sauvonnet, N. and Pugsley, A.P. (1999) Genetic dissection of the outer membrane secretin PulD: are there distinct domains for multimerization and secretion specificity? J Bacteriol, 181, 7212-7220.

Hardie, K.R., Lory, S. and Pugsley, A.P. (1996a) Insertion of an outer membrane protein in *Escherichia coli* requires a chaperone-like protein. EMBO J, 15, 978-988.

Hardie, K.R., Seydel, A., Guilvout, I. and Pugsley, A.P. (1996b) The secretin-specific, chaperone-like protein of the general secretory pathway: separation of proteolytic protection and piloting functions. Mol. Microbiol, 22, 967-976.

Koebnik, R., Locher, K.P. and Van Gelder, P. (2000) Structure and function of bacterial outer membrane proteins: barrels in a nutshell. Mol Microbiol, 37, 239-253.

Koronakis, V., Sharff, A., Koronakis, E., Luisi, B. and Hughes, C. (2000) Crystal structure of the bacterial membrane protein TolC central to multidrug efflux and protein export. Nature, 405, 914-919.

Koster, M., Bitter, W., de Cock, H., Allaoui, A., Cornelis, G. and Tommassen, J. (1997) The outer membrane component, YscC, of the Yop secretion machinery of *Yersinia enterocolitica* forms a ring-shaped multimeric complex. Mol Microbiol, 26, 789-797.

Köhler, R., Schäfer, K., Müller, S., Vignon, G., Driedrichs, K., Philippsen, A., Ringler, P., Pugsley, A.P., Engel, A. and Welte, W. (2004) Structure and assembly of pseudopilin PulG. Mol. Microbiol., 54, 647-664.

Lario, P.I., Pfuetzner, R.A., Frey, E.A., Creagh, L., Haynes, C., Maurelli, A.T. and Strynadka, N.C. (2005) Structure and biochemical analysis of a secretin pilot protein. EMBO J, 24, 1111-1121.

Lee, M.S., Chen, L.Y., Leu, W.M., Shiau, R.J. and Hu, N.T. (2005) Associations of the major pseudopilin XpsG with XpsN (GspC) and secretin XpsD of *Xanthomonas campestris pv. campestris* type II secretion apparatus revealed by crossling analysis. J Biol Chem, 280, 4585-4591.

Letellier, L., Howard, S.P. and Buckley, T.J. (1997) Studies on the energetics of proaerolysin secretion across of the outer membrane of *Aeromonas spp*: evidence for requirement for both the protonmotive force and ATP. J Biol Chem, 272, 11109-11113.

Linderoth, N.A., Model, P. and Russel, M. (1996) Essential role of a sodium dodecyl sulfate-resistant protein IV multimer in assembly-export of filamentous phage. J. Bacteriol., 178.

Linderoth, N.A., Simon, M.N. and Russel, M. (1997) The filamentous phage pIV multimer visualized by scanning transmission electron microscopy. Science, 278, 1635-1638.

Lobley, A., Witmore, L. and Walace, B.A. (2002) Bioinformatics, 18, 211-212.

Ludtke, S.J., Baldwin, P.R. and Chiu, W. (1999) EMAN: Semiautomated software for high resolution single-particle reconstructions. J. Struct. Biol., 128, 82-97.

Marabini, R., Masegosa, I.M., San Martin, M.C., Marco, S., Fernandez, J.J., de la Fraga, L.G., Vaquerizo, C. and Carazo, J.M. (1996) J. Struct. Biol., 116, 237-240.

Marciano, D., Russel, M. and Simon, S. (2001) Assembling filamentous phage occlude pIV channels. Proc. Natl Acad. Sci. USA., 98, 9359-9364.

Marciano, D.K., Russel, M. and Simon, S.M. (1999) An aqueous channel for filamentous phage export. Science, 284, 1516-1519.

Marlovits, T.C., Kubori, T., Sukhan, A., Thomas, D.R., Galan, J.E. and Unger, V.M. (2004) Structural insights into the assembly of the type III secretion needle complex. Science, 306, 1040-1042.

Michaelis, S., Chapon, C., d'Enfert, C., Pugsley, A.P. and Schwartz, M. (1985) Characterization and expression of the structural gene for pullulanase, a maltose-inducible secreted protein of *Klebsiella pneumoniae*. J Bacteriol, 164, 633-638.

Miller, J.H. (1992) A short course in bacterial genetics. A laboratory manual and Handbook for *Escherichia coli* and related bacteria. Cold Spring Harbor Press, Cold Spring Harbor.

Müller, S.A., Goldie, K.N., Bürki, R., Häring, R. and Engel, A. (1992) Factors influencing the precision of quantitative scanning transmission electron microscopy. Ultramicroscopy, 46, 317-334.

Nouwen, N., Ranson, N., Saibil, H., Wolpensinger, B., Engel, A., Ghazi, A. and Pugsley, A.P. (1999) Secretin PulD: association with pilot protein PulS, structure and ion-conducting channel formation. Proc. Natl. Acad. Sci. USA, 96, 8173-8177.

Nouwen, N., Stahlberg, H., Pugsley, A.P. and Engel, A. (2000) Domain structure of secretin PulD revealed by limited proteolysis and electron microscopy. EMBO J., 19, 2229-2236.

Opalka, N., Beckmann, R., Boisset, N., Sion, M.N., Russel, M. and Darst, S. (2003) Structure of the filamentous phage pIV multimer by cryo-electron microscopy. J. Mol. Biol., 325, 461-470.

Penczek, P., Radermacher, M. and Frank, J. (1992) Three-dimensional reconstitution of single particles embedded in ice. Ultramicroscopy, 40, 33-53.

Possot, O., Letellier, L. and Pugsley, A.P. (1997) Energy requirement for pullulanase secretion by the main terminal branch of the general secretory pathway. Mol. Microbiol., 24, 457-464.

Possot, O., Vignon, G., Bomchil, N., Ebel, F. and Pugsley, A.P. (2000) Multiple interactions between pullulanase secreton components involved in stabilization and cytoplasmic membrane association of PulE. J. Bacteriol., 182, 2142-2152.

Possot, O.M., Gérard-Vincent, M. and Pugsley, A.P.

(1999) Membrane association and multimerization of secreton component PulC. J. Bacteriol., 181, 4004-4011.

Pugsley, A.P. (1993) The complete general secretory pathway in gram-negative bacteria. Microbiol. Rev., 57, 50-108.

Pugsley, A.P., Bayan, N. and Sauvonnet, N. (2001) Disulphide bond formation in secreton component PulK provides a possible explanation for the role of DsbA in pullulanase secretion. J. Bacteriol., 183, 1312-1319.

Pugsley, A.P., Kornacker, M.G. and Poquet, I. (1991) The general secretion pathway is directly required for extracellular pullulanase secretion in Escherichia coli. Mol Microbiol, 5, 343-352.

Sandkvist, M. (2001) Biology of type II secretion. Mol. Microbiol., 40, 271-283.

Sauvonnet, N., Vignon, G., Pugsley, A.P. and Gounon, P. (2000) Pilus formation and protein secretion by the same machinery in *Escherichia coli*. EMBO J., 19, 2221-2228.

Shevchik, V.E. and Condemine, G. (1998) Functional characterization of the *Erwinia chrysanthemi* OutS protein, an element of a type II secretion system. Microbiol, 144, 3219-3228.

Shevchik, V.E., Robert-Badouy, J. and Condemine, G. (1997) Specific interaction between OutD, an *Erwinia chrysanthemi* outer membrane protein of the general secretory pathway, and secreted proteins. EMBO. J, 16, 3007-3016.

Vignon, G., Köhler, R., Larquet, E., Giroux, S., Prévost, M.-C., Roux, P. and Pugsley, A.P. (2003) Type IV-like pili formed by the type II secreton: specificity, composition, bundling, polar localization and surface presentation of peptides. J. Bacteriol., 185, 3416-3428.

Voulhoux, R., Ball, G., Ize, B., Vasil, M.L., Lazdunski, A., Wu, L.-F. and Filloux, A. (2001) Involvement of the twin-arginine translocation system in protein secretion via the type II pathway. EMBO. J., 20, 6735-6741.

Whitmore, L. and Wallace, L.A. (2004) Nucleic Acids Res., 32, W668-673.

Zhao, S., Tobiason, D.M., Hu, M., Seifert, H.S. and Nicholas, R.A. (2005) The penC mutation conferring antibiotic resistance in *Neisseria gonorrhoeae* arises from a mutation in the PilQ secretin that interferes with multimer assembly and presvents antibiotic influx. Mol. Microbiol., in press.

Chapter 4

Cytotoxin ClyA from Escherichia coli assembles to a 13-meric pore independent of its redox-state

Nora Eifler[1,3], Michael Vetsch[2,3], **Marco Gregorini**[1], Philippe Ringler[1], Mohamed Chami[1], Ansgar Philippsen[1], Andrea Fritz[2], Shirley A. Müller[1], Rudi Glockshuber[2], Andreas Engel[1], Ulla Grauschopf[2]

4.1 Abstract

ClyA is a pore-forming toxin from virulent *Escherichia coli* and *Salmonella enterica* strains. Here we show that the intrinsic hemolytic activity of ClyA is independent of its redox state, and that the assembly of both reduced and oxidized ClyA to the ring-shaped oligomer is triggered by contact with lipid or detergent. A rate-limiting conformational transition in membrane-bound ClyA monomers precedes their assembly to the functional pore. We obtained a 3D model of the detergent-induced oligomeric complex at 12 Å resolution by combining cryo- and negative stain electron microscopy with mass measurements by scanning transmission electron microscopy. The model reveals that 13 ClyA monomers assemble into a cylinder with a hydrophobic cap region, which may be critical for membrane insertion.

Keywords: pore-forming toxin, structure, assembly, electron microscopy

4.2 Introduction

Pore-forming toxins (PFTs) kill target cells by inserting channels into their membranes. Strikingly, PFTs are soluble in aqueous solution before converting to a membrane-embedded state. This transition requires the exposure of hydrophobic surfaces that are buried in the water-soluble state, and frequently includes assembly of monomers to an annular, oligomeric pore complex (reviewed in Parker and Feil (2005)). PFTs are classified into α PFTs and β PFTs (Gouaux, 1997). α PFTs span the target membrane with α-helices. Well-known members of this class are the colicins (Zakharov and Cramer, 2002) and diphtheria-toxin (Choe et al., 1992). Conversely, β PFTs insert into membranes by forming transmembrane β-barrels. This class includes *Staphylococcus aureus* α-hemolysin (Song et al., 1996), *Aeromonas hydrophila* aerolysin (Parker et al., 1994), and cholesterol-dependent cytolysins (Tweten et al., 2001).

ClyA (also referred to as HlyE or SheA) is a recently discovered PFT (del Castillo et al., 1997; Ludwig et al., 1995; Oscarsson et al., 1996), which could not be classified so far due to the lack of structural data. It is responsible for the hemolytic phenotype of *several Escherichia coli* and *Salmonella enterica* strains (del Castillo et al., 1997; Ludwig et al., 2004; Oscarsson et al., 2002). ClyA lyses erythrocytes from different species, shows cytotoxi-

[1]M.E.Müller Institute, Biozentrum, University of Basel, Klingelbergstrasse 50/70, CH-4056 Basel, Switzerland

[2]Institute for Molecular Biology and Biophysics, ETH Zürich, CH-8093 Zürich, Switzerland

[3]These authors contributed equally.

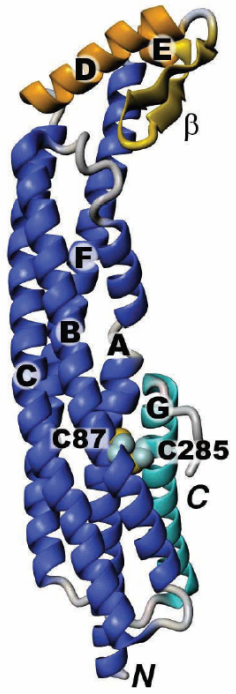

Figure 4.1: **Structure of monomeric ClyA.** Atomic structure of soluble, monomeric $ClyA_{red}$ (Wallace et al., 2000) with the four-helix bundle formed by helices A, B, C and F (blue), the b hairpin (yellow) with its flanking helices D and E (orange), and the C-terminal helix G (cyan) that is linked to helix B by a disulfide bridge (C87-C285) in $ClyA_{ox}$.

city towards cultured mammalian cells, and induces apoptosis of macrophages (Lai et al., 2000; Ludwig et al., 1999; Oscarsson et al., 1999). In addition, sublytic amounts of ClyA induce slow intracellular Ca^{2+} oscillations in epithelial cells (Soderblom et al., 2005). These observations suggest that ClyA contributes to the virulence of pathogenic bacterial strains (Kerenyi et al., 2005; Ludwig et al., 2004).

The crystal structure of monomeric, soluble ClyA (34 kDa) revealed a rod-shaped, mostly α-helical molecule ((Wallace et al., 2000); Figure 4.1). It consists of a long four-helix bundle (helices A, B, C, and F) with a short C-terminal helix (helix G) alongside at one end. A subdomain consisting of a short β-hairpin (the "β-tongue") flanked by two short helices (helices D and E), is located on the other end of the bundle. The β-tongue region forms the major hydrophobic patch on the ClyA surface, and mutational analysis indicated that this region interacts with target membranes (Wallace et al., 2000). The two cysteine residues of ClyA, located in helix B (C87) and helix G (C285), are sufficiently close to form a disulfide bond. In the crystal structure of ClyA the cysteines are reduced and bridged by a mercury atom of a Hg(II)-derivative compound.

Based on the crystal structure of the monomer and on electron microscopy (EM) data, Wallace et al. (2000) constructed a model of the ClyA pore, in which eight protomers are aligned perpendicular to the membrane surface with the β-tongue interacting with lipid. In this octameric assembly the conformation of the monomer is essentially retained, apart from a minor 20° reorientation of the subdomain containing the β-tongue with respect to the rest of the molecule.

Many aspects of the biogenesis of functional ClyA are largely unknown. Translocation to the periplasm is neither mediated by a signal sequence nor requires cytolytic activity of ClyA (del Castillo et al., 1997; del Castillo et al., 2001; Ludwig et al., 1999). Export from the bacterial cell occurs in outer membrane vesicles (OMVs) where ClyA forms oligomeric, membrane-embedded pores (Wai et al., 2003a). Soluble ClyA in the periplasm contains the C87-C285 disulfide bond (Ludwig et al., 1999; Oscarsson et al., 1999; Wai et al., 2003a), whereas OMV-embedded ClyA is reduced (Wai et al., 2003a). Recent results indicated that oxidized ClyA ($ClyA_{ox}$) has a lower intrinsic hemolytic activity than reduced ClyA ($ClyA_{red}$) (Atkins et al., 2000; Wai et al., 2003a; Wallace et al., 2000). Therefore, it was postulated that the disulfide bond may prevent assembly of functional pore complexes by anchoring helix G to the four-helix bundle (Atkins et al., 2000). Since secretion and activation seem to occur hand in hand with a change in the redox state of ClyA, it was hypothesized that the assembly of active ClyA pores is redox-regulated (Atkins et al., 2000; Wai et al., 2003a; Wallace et al., 2000). This is supported by the observation that *E. coli dsbA*$^-$ and *dsbB*$^-$ strains, which are deficient in periplasmic disulfide bond formation, display a ClyA-dependent hemolytic phenotype on blood agar plates that is not detectable for the corresponding wild-type strain (Wai et al., 2003a).

Here we provide firm evidence that, in contrast to previous results, ClyA is assembly-competent and active independent of its redox state. We show that detergent or lipid induces a slow structural change in monomeric ClyA towards the conformation required for the assembly into the cylindrical pore complex. Using cryo-EM and single particle analysis we have established the 3D structure of the oligomeric pore complex at 12 Å resolution. It comprises thirteen subunits, consistent with the mass measured by scanning transmission electron microscopy (STEM). Our three-dimensional model

combined with spectroscopic data suggests a large structural change of the ClyA monomers during assembly of the pore complex. Projections from vitrified proteoliposomes bearing lipid-inserted pore complexes document that the architectures of the detergent-induced and the lipid-inserted ClyA pore complexes are highly similar.

4.3 Results

4.3.1 Redox state of ClyA cysteines does not modulate hemolytic activity

To date, controversy exists about the activity of $ClyA_{ox}$ (Atkins et al., 2000; Wai et al., 2003a; Wai et al., 2003b; Wallace et al., 2000). In order to clarify the functional and structural role of the disulfide bond of ClyA, we prepared homogeneous samples of $ClyA_{red}$ and of $ClyA_{ox}$. $ClyA_{red}$ was overexpressed and isolated from the cytoplasm of *E. coli*. $ClyA_{ox}$ was obtained by Cu^{2+}-mediated air oxidation of purified $ClyA_{red}$, and subjected to gel filtration to remove high molecular weight aggregates that formed during oxidation. The redox state of $ClyA_{ox}$ and $ClyA_{red}$ was verified by Ellman's assay and by labeling of free cysteines under denaturing conditions with 5-((((2-iodoacetyl)amino)ethyl)amino)naphthalene-1-sulfonic acid (IAEDANS) (Supplementary Figure 4.8).

We used gel filtration to analyze the oligomerization state of freshly purified $ClyA_{red}$ and $ClyA_{ox}$. At 15 °C both $ClyA_{red}$ and $ClyA_{ox}$ are stable monomers even at very high protein concentrations (100 μM, Figure 4.2A, Supplementary Figure 4.9). The observed retention volumes correspond to that of a globular 43 kDa protein. Considering that the elongated shape of ClyA will lead to a lower retention volume, this clearly indicates the monomeric state of $ClyA_{ox}$ and $ClyA_{red}$ (34 kDa). Thus, our experiments contradict the hypothesis of redox-regulated oligomerization of soluble ClyA (Atkins et al., 2000; Wai et al., 2003a). The only difference between $ClyA_{ox}$ and $ClyA_{red}$ with regard to the oligomeric state was the much higher tendency of $ClyA_{ox}$ to form inactive, high molecular weight aggregates upon prolonged incubation, especially at 37 °C (Supplementary Figure 4.9).

We next studied the hemolytic activity of $ClyA_{red}$ and $ClyA_{ox}$. As shown in Figure 4.2B, $ClyA_{red}$ and $ClyA_{ox}$ displayed the same hemolytic activity in a liquid hemolysis assay with horse erythrocytes. To test whether the difference in hemolytic activity observed by other authors (Atkins et al., 2000; Wai et al., 2003a) reflects different kinetics of hemolysis induced by $ClyA_{red}$ and $ClyA_{ox}$, we followed the time-course of hemolysis (Figure 4.2C). Yet again, $ClyA_{red}$ and $ClyA_{ox}$ were identical in activity. In addition, we tested whether ClyA changes its redox state upon contact with erythrocytes. Exposure of $ClyA_{red}$ and $ClyA_{ox}$ to IAEDANS under denaturing conditions before and after incubation with erythrocytes revealed that neither $ClyA_{red}$ nor $ClyA_{ox}$ changes the redox state upon membrane insertion (Figure 4.2D). Taken together, our data show that the intrinsic hemolytic activity of ClyA is independent of its redox state.

4.3.2 Oligomerization of ClyA is triggered by detergent

Since no functional differences were detectable between $ClyA_{red}$ and $ClyA_{ox}$, and since biologically active ClyA is exported from the bacterial cell in its reduced state (Wai et al., 2003a), we focused our structural analysis on the pore complex formed by $ClyA_{red}$. In search of conditions that would allow the pore structure to be investigated by single particle analysis, we screened a variety of detergents for their ability to trigger assembly of ClyA. Many different detergents induced the formation of oligomeric complexes (data not shown) with dimensions similar to those of lipid-embedded complexes reported by Wallace et al. (2000). The most homogeneous samples were obtained with n-dodecyl-β-D-maltopyranoside (DDM). The kinetics of DDM-induced oligomerization of $ClyA_{red}$ were analyzed by gel filtration (Figure 4.3A). We selected a temperature of 15 °C, at which the assembly process is slow enough to allow for identification of assembly intermediates (see below). A shift of the retention volume of $ClyA_{red}$ from 15.1 ml to 12.3 ml was observed after only two minutes of exposure to DDM. This peak decreased with increasing incubation time while another peak at a retention volume of 9.6 ml appeared. Because retention volumes of soluble proteins are not affected by DDM (soluble mass standard proteins showed the same retention volumes with and without DDM, Figures 4.2C and 4.3A), we conclude that association of monomeric $ClyA_{red}$ with detergent causes the lower retention volume of $ClyA_{red}$ observed after short exposure to DDM. The dominant peak at 9.6 ml contained oligomers, as documented by EM

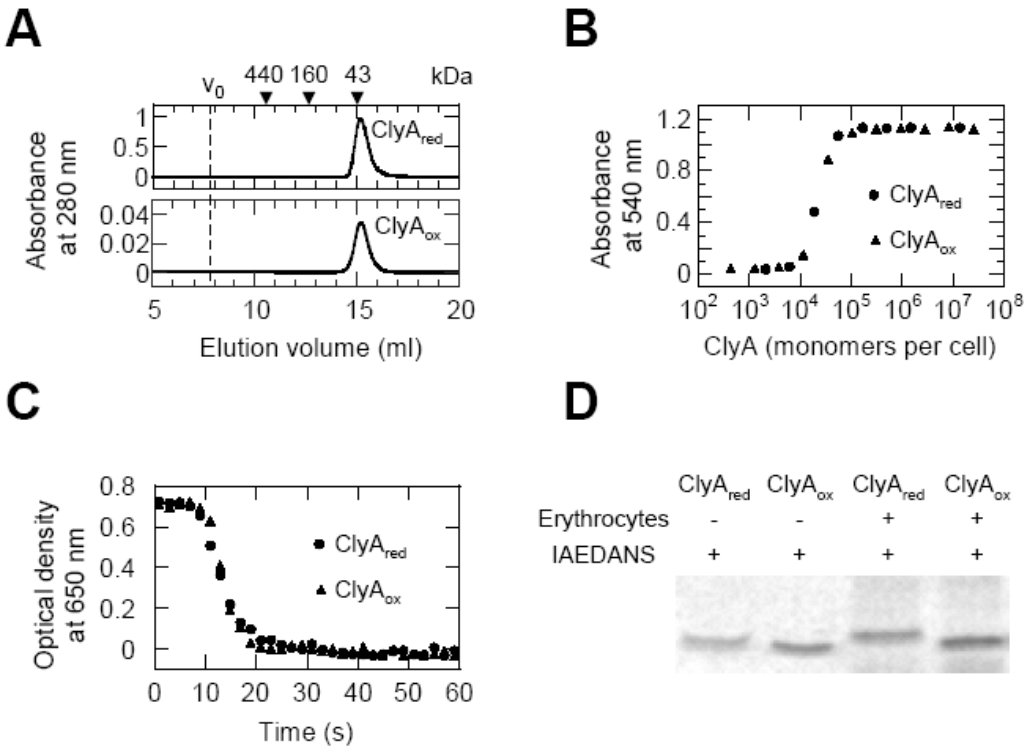

Figure 4.2: **Activity of reduced and oxidized ClyA.** (A) Oligomerization state of $ClyA_{red}$ and $ClyA_{ox}$ in PBS at 15 °C. $ClyA_{red}$ (100 μM) and $ClyA_{ox}$ (5 mM) were subjected to analytical gel filtration. The protein is monomeric, even at high concentrations. Arrows indicate retention volumes of soluble mass standard proteins. v_0, void volume. (B) Hemolytic activity of $ClyA_{red}$ and $ClyA_{ox}$ at 37 °C. Hemolysis of a 1% suspension of horse erythrocytes by $ClyA_{red}$ and $ClyA_{ox}$ (concentration range between 0.01 nM and 1000 nM) was examined using a liquid hemolysis assay according to Rowe and Welch (1994). (C) Kinetics of hemolysis induced by $ClyA_{red}$ and $ClyA_{ox}$ at 37 °C. The decrease in turbidity upon hemolysis of a 0.1% suspension of horse erythrocytes exposed to 250 nM $ClyA_{red}$ or $ClyA_{ox}$ was monitored at 650 nm. (D) Redox state of ClyA after insertion into erythrocyte membranes. 250 nM $ClyA_{red}$ (lanes 1, 3) or $ClyA_{ox}$ (lanes 2, 4) were added to a 1% suspension of horse erythrocytes (lanes 3, 4) or PBS (lanes 1, 2) and incubated for 30 min at 37 °C. The samples were thereupon exposed to IAEDANS under denaturing conditions and analyzed by SDS-PAGE (there are no prominent bands of erythrocyte proteins in the mass range of ClyA).

(see below). Quantitative analysis of the peak areas at 9.6 and 12.3 ml showed that DDM-associated, monomeric $ClyA_{red}$ (intermediate I_1) disappeared with virtually the same rate as oligomeric $ClyA_{red}$ was formed, with half-lives of 1000 $\pm$ 300 s and 1100 $\pm$ 200 s, respectively (Figure 4.3A, right panels). To test whether intermediate I_1 indeed represents monomeric $ClyA_{red}$ in complex with detergent, rather than an oligomeric form, $ClyA_{red}$ was exposed to DDM for different times, cross-linked with dithiobis(succinimidylpropionate) (DSP), and the products were examined by SDS-PAGE (Figure 4.3B, left panel). The protein was predominantly monomeric after 2 min exposure to DDM (Figure 4.3B, left panel, lane 2). With longer exposure to DDM (lanes 3 - 6), the band corresponding to monomeric $ClyA_{red}$ gradually disappeared and the band corresponding to the covalently linked pore complex appeared (Supplementary Figure 4.10). Quantitative densitmoetric analysis showed that the band of monomeric $ClyA_{red}$ exhibits the same half-life (1100 $\pm$ 200s) as intermediate I_1 identified by gel filtration (Figures 4.3A and 4.3B, left panels). Together, our data suggest a model in which $ClyA_{red}$ inserts into the detergent micelle as a monomer and then assembles rapidly via faintly populated intermediates to a defined oligomeric complex.

Electron micrographs of negatively stained protein eluting at 9.6 ml revealed homogeneous, ring-shaped and rectangular projections corresponding to top- and side views of the $ClyA_{red}$ oligomer (Figure 4.3C), top views representing the majority of particle projections. The outer diameter of the top view averages varied between 90 Å and 125 Å (Supplementary Figure 4.12). This is consistent with the diameter of ClyA oligomers reconstituted into lipid vesicles (Wallace et al., 2000), and with that

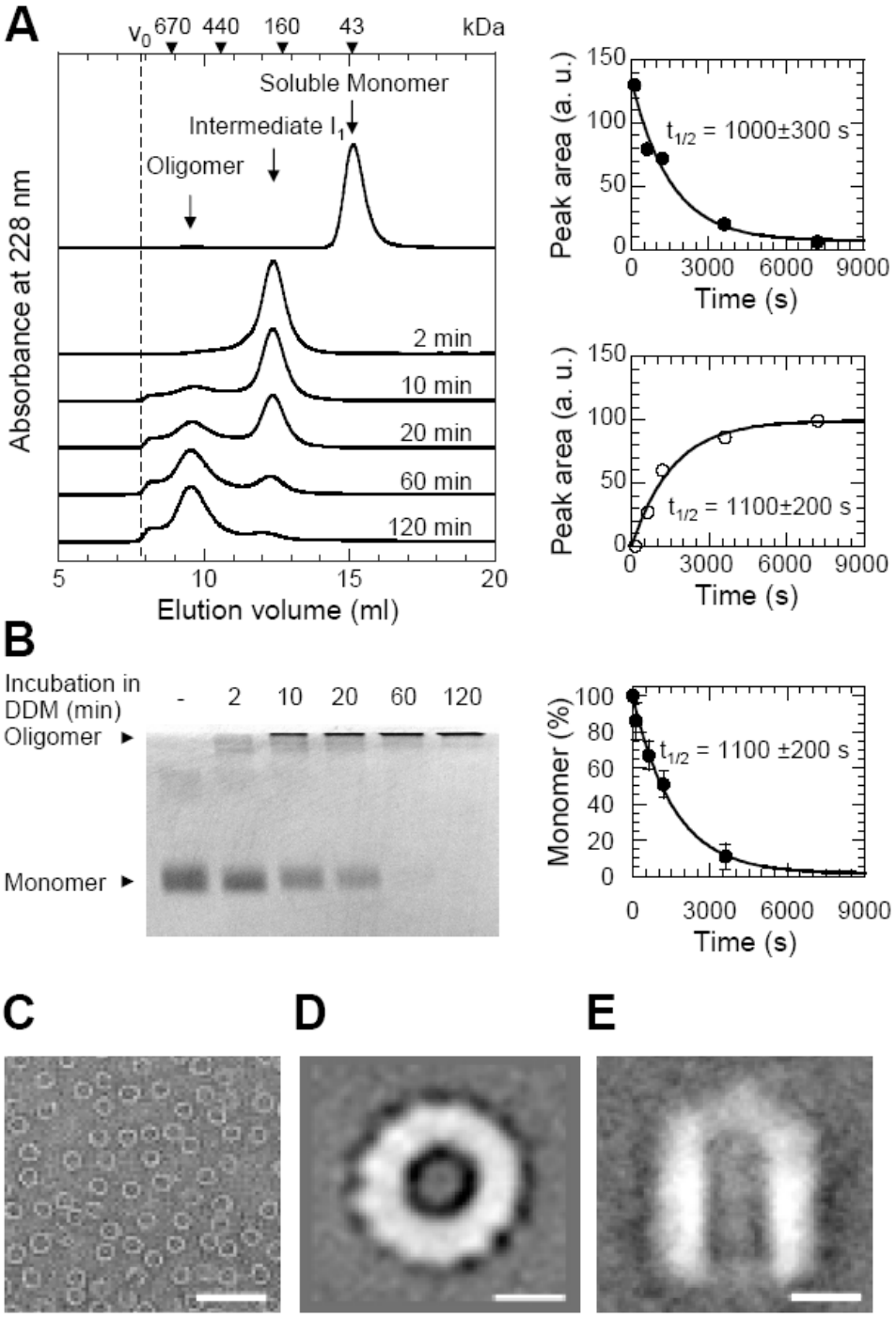

Figure 4.3: **Detergent-induced oligomerization of $ClyA_{red}$.** (A) $ClyA_{red}$ (5 μM) was incubated in 0.1% DDM at 15 °C. Samples were taken at the times indicated and subjected to analytical gel filtration in 0.1% DDM at 4 °C. For comparison, the elution profile of soluble, monomeric ClyA is shown (left panel). Upon addition of DDM, monomeric $ClyA_{red}$ immediately associates with detergent, leading to a shift in the elution volume from 15.1 ml to 12.3 ml. The detergent bound monomer then slowly converts to oligomeric $ClyA_{red}$, eluting at 9.6 ml. Arrows indicate retention volumes of soluble mass standard proteins. v_0, void volume. Peak areas of monomeric $ClyA_{red}$ (right, upper panel) and oligomeric $ClyA_{red}$ (right, lower panel) were plotted against time and fitted with a monoexponential function (black line). (B) Cross-linking analysis of the oligomerization of $ClyA_{red}$. Samples identical to those in (A) were mixed with DSP and incubated for 5 minutes at 25 °C. The reaction was stopped by addition of Tris/HCl, and samples were applied onto a 16% polyacrylamide-SDS gel (left panel). The bands of monomeric $ClyA_{red}$ were quantified by densitometry, the fraction of monomers was plotted against incubation time (right panel), and fitted with a monoexponential function (black line). (C) Electron-micrograph of negatively stained $ClyA_{red}$ particles taken from the peak eluted at 9.6 ml in (A). (D) Top view class average of 145 negatively stained $ClyA_{red}$ particles. (E) Side view class average of 205 negatively stained $ClyA_{red}$ particles. The scale bars correspond to 40 nm in D, and 5 nm in E, F.

of ClyA pores found in isolated OMVs (data not shown). The negative-stain side view average revealed a cylindrical structure that converges to a cap at one end and has a total length of about 160 Å (Figure 4.3E), which stands in contrast to monomeric ClyA, exhibiting a length of only 110 Å (Wallace et al., 2000). Single particle analysis of negatively stained pore complexes was carried out to obtain the fine structural features of the pore complex. 2876 top- and 826 side views were extracted from the micrographs, aligned, and classified by multivariate-statistical analysis to calculate class averages. The negative-stain top view class average of Figure 4.3D shows a cylindrical pore complex with an inner structure. Angular periodicity analysis indicated a 13-fold symmetry (Supplementary Figure 4.11). Rotational power spectra of some class averages additionally suggest a minor possibility for an 11-fold symmetry (Supplementary Figure 4.11), however, from mass data of the $ClyA_{red}$ complex obtained with the STEM (Figure 4.4A) an 11-fold symmetry can be definitely excluded. Moreover, the peaks at the 11-fold and 13-fold rotational component in Supplementary Figure 4.11 argue against a 12-fold symmetry, because they emphasize an odd-numbered assembly of the subunits. To compare the structures of pores formed by either reduced or oxidized ClyA, pores formed by $ClyA_{ox}$were also examined by negative stain electron microscopy. Class averages of these $ClyA_{ox}$ pores revealed a cylindrical structure with 13-fold symmetry and the same dimensions as $ClyA_{red}$ (Supplementary Figure 4.12).

4.3.3 STEM mass measurements of ClyA indicate a 13-mer

Freeze-dried detergent solubilized ClyA complexes revealed three distinct populations: Single complexes, as well as double and triple forms, where two or three single complexes were associated (Figure 4.4, galleries). According to sequence the mass of the $ClyA_{red}$ monomer is 34.45 kDa. In comparison, the mass of the complex determined by STEM analysis was 475 ± 86 kDa ($n = 184$; standard error (SE) = 6 kDa; overall uncertainty ± 25 kDa considering the 5% uncertainty of the STEM calibration) for the single complex, 947 ± 140 kDa ($n = 114$; SE = 13 kDa; overall uncertainty ± 49 kDa) for the double form and 1357 ± 108 kDa ($n = 114$; SE = 20 kDa; overall uncertainty ± 71 kDa) for the triple form (Figure 4.4A). Considering the overall uncertainty of the measurement and the presence of associated DDM, these data indicate that the oligomeric ClyA complex comprises 13 ClyA monomers (mass expected without detergent, 448 kDa), consistent with the symmetry of negative stain top view averages (Figure 4.3D, Supplementary Figure 4.12).

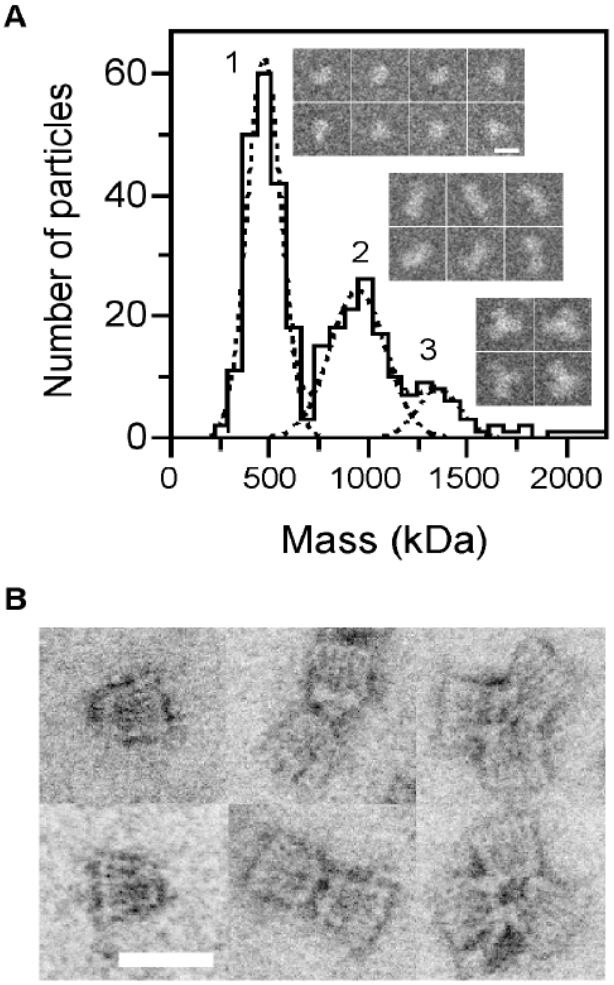

Figure 4.4: **STEM analysis of the ClyA complex.** (A) As shown by the histogram the masses measured for the unstained ClyA preparation fell into three distinct classes (1, 2, and 3) that on visual inspection of the particles (galleries) could be assigned to single complexes with a mass of 475 ± 86 kDa ($n = 184$; overall uncertainty = 25 kDa), two associated complexes, mass 974 ± 140 kDa ($n = 114$; overall uncertainty = 49 kDa) and three associated complexes, mass 1357 ± 108 kDa ($n = 30$; overall uncertainty = 71 kDa). (B) Dark-field STEM images of the measured ClyA preparation after negative staining. Left, side views of the single complex. Centre, two complexes associated at their tips. Right, three complexes associated at their tips. The high contrast of the STEM allows the individual monomers making up the complex to be distinguished. Either six or seven subunits can be counted on the side views, consistent with 13-fold symmetry. The scale bar corresponds to 20 nm in A, B.

Images recorded by STEM from the same ClyA sample after negative staining showed that the single complexes associate at their pointed ends (Figure 4.4B), implying that the cap is the main hydrophobic region. In agreement, the difference between the measured and the calculated mass was smaller in these forms, because the individual complexes could not bind as much detergent when associated (Figure 4.4A). Together, this suggests that the cap is a hydrophobic structure that potentially facilitates interaction with the lipid bilayer. The side views also frequently exhibited 6 or 7 longitudinal striations compatible with the presence of 13 ClyA monomers in the complex (Figure 4.4B).

4.3.4 3D Model of oligomeric ClyA

Cryo-EM was used to establish the global three-dimensional (3D) structure of the $ClyA_{red}$ complex, since quick-freezing of particle suspensions ensures the preservation of the undistorted, native structure (Dubochet et al., 1988). In all, 2699 images of top- and 3620 images of side views selected from cryo-electron micrographs taken in plane (Figure 4.5A) and 2132 particles at 15° tilt angle were used to reconstruct the 3D structure. Class averages of the particles were calculated as described above (Figure 4.5A, insets). A starting 3D model was calculated from selected top and side views using the EMAN software (Ludtke et al., 1999). A 13-fold cyclic symmetry was imposed, since both negative stain EM and STEM indicated that the complex has 13 ClyA subunits. Refinement of the alignment by projection matching in SPIDER (Frank et al., 1996) and omitting projections with low correlation coefficients compared to respective back-projections resulted in a final 3D model containing 8429 particles. The 0.5 Fourier shell correlation criterion indicated a resolution of 12 Å (Supplementary Figure 4.13). Figure 4.5B displays the surface rendered 3D map of the ClyA complex with characteristic bottom and top features, while the central cross-section through the 3D map is contoured in Figure 4.5C. The model shows that the ClyA complex is a cylindrical channel that converges into a cap at one end. It has a length of 160 Å, a maximum outer diameter of 120 Å and a widest inner diameter of about 70 Å. The outer diameter of the cylindrical cap is 40 Å, and its height is 20 Å.

The apparent hydrophobicity of the cap region (see above) suggests that this cap may be critical for membrane insertion. The observed cap may correspond to a 26-stranded β-barrel (Figure 4.5D) to which each protomer contributes two strands. The observed diameter of the cap agrees well with the calculated diameter of a 26-stranded barrel with vertically oriented β-strands. The two-stranded β-tongue in the structure of monomeric ClyA (Figure 4.5) provides an attractive candidate for formation of such a barrel for the following reasons: The β-tongue is hydrophobic, approximately 20 Å long, located at one end of ClyA, and sensitive to mutations that abolish the hemolytic activity of ClyA (Wallace et al., 2000).

4.3.5 Cryo-EM of lipid-embedded ClyA

To determine the position of the ClyA pore complex with respect to the lipid bilayer proteoliposomes were prepared by adding monomeric ClyA to brain lipid vesicles. Figures 4.6A and 4.6B show cryo-EM images of membrane bound oligomers associated with a mixture of spherical liposomes and continuous bilayers. Projections of membrane incorporated ClyA range from top views over different side view angles to tangential views through the edges of the three-dimensional liposomes. 1101 side views and 431 top views were selected and analyzed as described above. Density maxima in the gallery of side view averages (Figure 4.6D-G) allow the detergent-induced pore complex (Figure 4.6H) to be aligned with respect to the bilayer, indicating that ClyA inserts via its cap region into the membrane. The CTF corrected top view average of reconstituted complexes exhibits a central mass density (Figure 4.6C). Side view averages have a length of 140 - 150 Å, depending on the projection angle, and a diameter of 120 Å. The cap seen in the detergent-induced pore complex is not visible in the averages of lipid embedded ClyA (Figure 4.6D-G), resulting in a 10-20 Å shorter length than the ClyA complex in detergent (Figure 4.6H). Although the cap is not visible in side view averages of lipid embedded ClyA complexes, this feature is occasionally seen in single complexes (white arrowheads in Figure 4.6A), together with cap-free conformations (black arrowheads in Figure 4.6A). Proteoliposomes generated by Biobeads-driven reconstitution of detergent-induced pores (data not shown) exhibited the same morphology as the proteoliposomes in Figure 4.6, suggesting that the conformation of the detergent-induced pore complex may be a precursor of the lipid bound form.

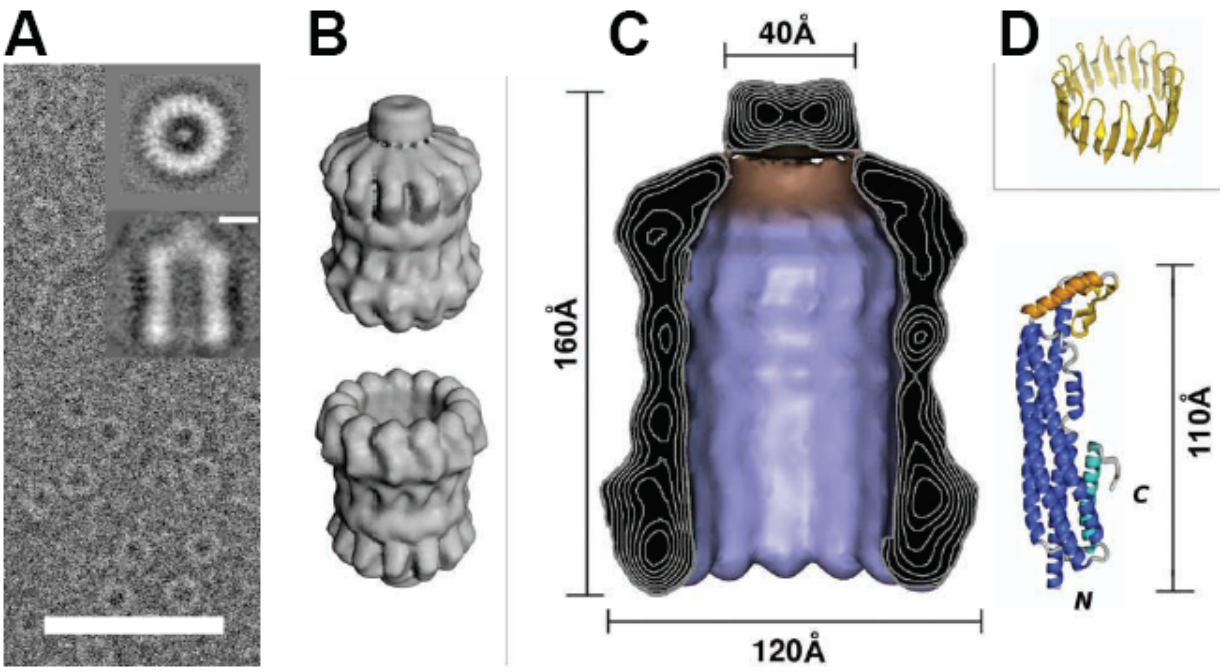

Figure 4.5: **Cryo-electron microscopy of vitrified ClyA complexes and model of the ClyA oligomer.** (A) Overview image of frozen hydrated particles. The scale bar corresponds to 50 nm. Top and side view class averages, containing 302 and 796 particles each, are shown in the insets. The top view reveals some structure in the channel center whereas the cap at one end of the pore complex is seen in the side view. The scale bar in the insets corresponds to 5 nm. (B) Isocontour representations of the reconstructed single particle density, showing the prominent cap region as well as the open end of the pore. (C) Side by side comparison of the 3D EM reconstruction of the pore with the X-ray structure of monomeric ClyA. The 3D EM isosurface representation is cut open to expose the cavity as well as the inner contour lines of the protein density. (D) Model of a 26-stranded β-barrel, the suggested cap structure. The barrel is formed by the β-tongues of each of the 13 monomers.

4.3.6 Spectroscopic analysis of structural changes during ClyA assembly

As shown above, rapid insertion of monomeric $ClyA_{red}$ into detergent micelles precedes the comparably slow assembly of ClyA pore complexes (Figure 4.3). We used fluorescence and far-UV circular dichroism (CD) spectroscopy to explore the kinetics of the structural changes involved. The tryptophan fluorescence emission of $ClyA_{red}$ increases 1.5-fold upon assembly in DDM (Figure 4.7A). The signal difference at 330 nm was used to follow the time-course of detergent-induced assembly of $ClyA_{red}$ under conditions identical to those in Figure 4.3A. The kinetic trace is characterized by a very fast and a slow phase with positive and negative amplitudes, respectively (Figure 4.7B). The fast phase reflects the formation of a hyperfluorescent intermediate (intermediate I_1 in Figure 4.7A) upon association of monomeric $ClyA_{red}$ with detergent. The slower kinetic phase is described by a monoexponential function with a half-life of 940 s. This half-life agrees with that measured for the disappearance of the monomer and the appearance of the oligomer (Figure 4.3A, B), suggesting that the observed slow phase reflects a conformational change in $ClyA_{red}$ that coincides with association of the individual subunits.

Figure 4.7C shows far-UV CD spectra of monomeric and oligomeric $ClyA_{red}$. Both spectra display minima at 208 nm and 222 nm, typical for proteins with a high content of α helical secondary structure. Oligomeric $ClyA_{red}$ exhibits increased signal intensity, indicating a conformational change during assembly. As the overall shape of the spectrum is retained, we conclude that no large α to β transition occurs during oligomerization of ClyA. Similar to the above fluorescence kinetics we exploited the signal difference at 225 nm to follow the time-course of detergent-induced $ClyA_{red}$ assembly (Figure 4.7D, upper panel). The trace is also characterized by a very fast phase with positive amplitude and a slow phase with negative amplitude. As in the fluorescence kinetics, the slower phase is described by a monoexponential function, yielding a half-life of 1000 s. This process thus coincides again with the disappearance of the monomer and the appearance of the oligomer (Figure 4.3A, B). The fact that a monoexponential function accurately describes

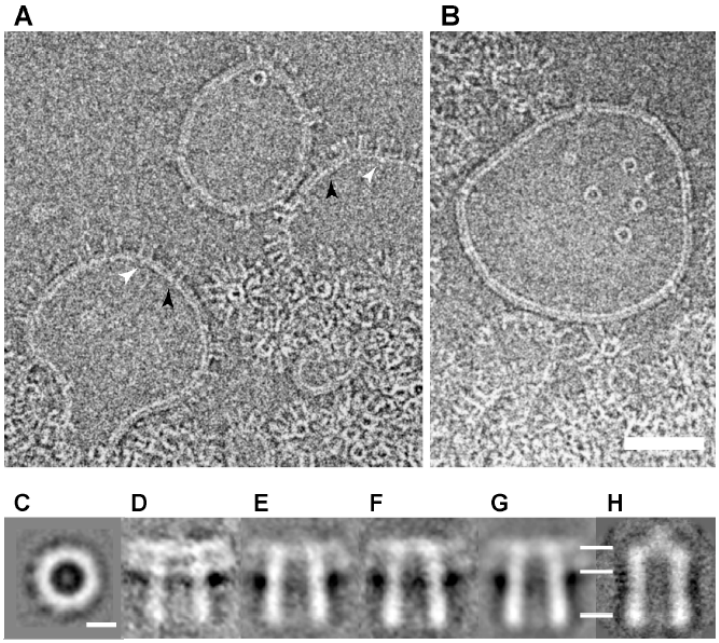

Figure 4.6: **Cryo-EM images of ClyA in lipid vesicles.** (A) and (B) High-resolution micrographs of ClyA incorporated in lipid vesicles in the absence of detergent. Upon contact with brain lipid vesicles monomeric ClyA forms pore assemblies appearing as ring-like structures with a central density in top view and as spikes protruding from the lipid bilayer in side view. The scale bar corresponds to 50 nm. (C) CTF corrected top view class average of lipid induced ClyA pore assemblies. The scale bar is valid for all averages and corresponds to 5 nm. (D)-(G) Gallery of side view averages of lipid induced ClyA pore complexes. Each average contains between 25 and 140 projections. The different orientations of the particles with respect to the spherical vesicles result in variations of the particle's length in projection (140 - 150 Å). Each image shows three distinct spots of higher density (marked with bars in (G)). (H) Side view average of the detergent induced ClyA complex aligned with respect to the membrane bound pore in (G).

oligomerization shows that the rate-limiting step for assembly is uni-molecular under the chosen conditions. To test this model, we repeated the assembly reaction at different initial protein concentrations (Supplementary Figure 4.14). The half-life of the slow phase was indeed independent of the concentration of $ClyA_{red}$. Consequently, a slow conformational change converts the monomeric intermediate I_1 to an assembly-competent intermediate I_2, and this conformational change is rate-limiting for the assembly of the complex. It should, however, be noted that association of assembly-competent subunits is per definition concentration-dependent. Therefore, at very low protein concentrations, assembly itself will become rate-limiting.

To test whether similar structural changes take place upon insertion of $ClyA_{red}$ into erythrocyte membranes, we repeated the CD measurements after addition of erythrocyte membranes to monomeric $ClyA_{red}$ (Figure 4.7D, lower panel; Supplementary Figure 4.15). The kinetic trace was very similar to that observed after addition of DDM. Again, a fast phase and a slow phase were detected with positive and negative amplitudes, respectively. Fitting the slower phase yields half-lives of 80 s at 15 °C and of 45 s at 37 °C. Assembly of $ClyA_{red}$ in erythrocyte membranes is thus about 10-fold faster compared to assembly in DDM. Nevertheless, the assembly kinetics in erythrocyte membranes are slower than the kinetics of hemolysis (Figure 4.2C). This can be well explained by the fact that a small fraction of functional pores is sufficient to attain full cell lysis at the chosen hemolysin to cell ratio (Figure 2B).

4.4 Discussion

4.4.1 Role of the Redox State of ClyA for Activity and Assembly

Atkins et al. (2000) reported that $ClyA_{ox}$ has no hemolytic activity whereas Wai et al. (2003a) detected activity of $ClyA_{ox}$, albeit 16-fold weaker compared to $ClyA_{red}$. Controversial results were also obtained on the oligomeric state of ClyA in solution. Whereas $ClyA_{ox}$ is consistently found to be monomeric, $ClyA_{red}$ has been described to be monomeric (Wallace et al., 2000), partially

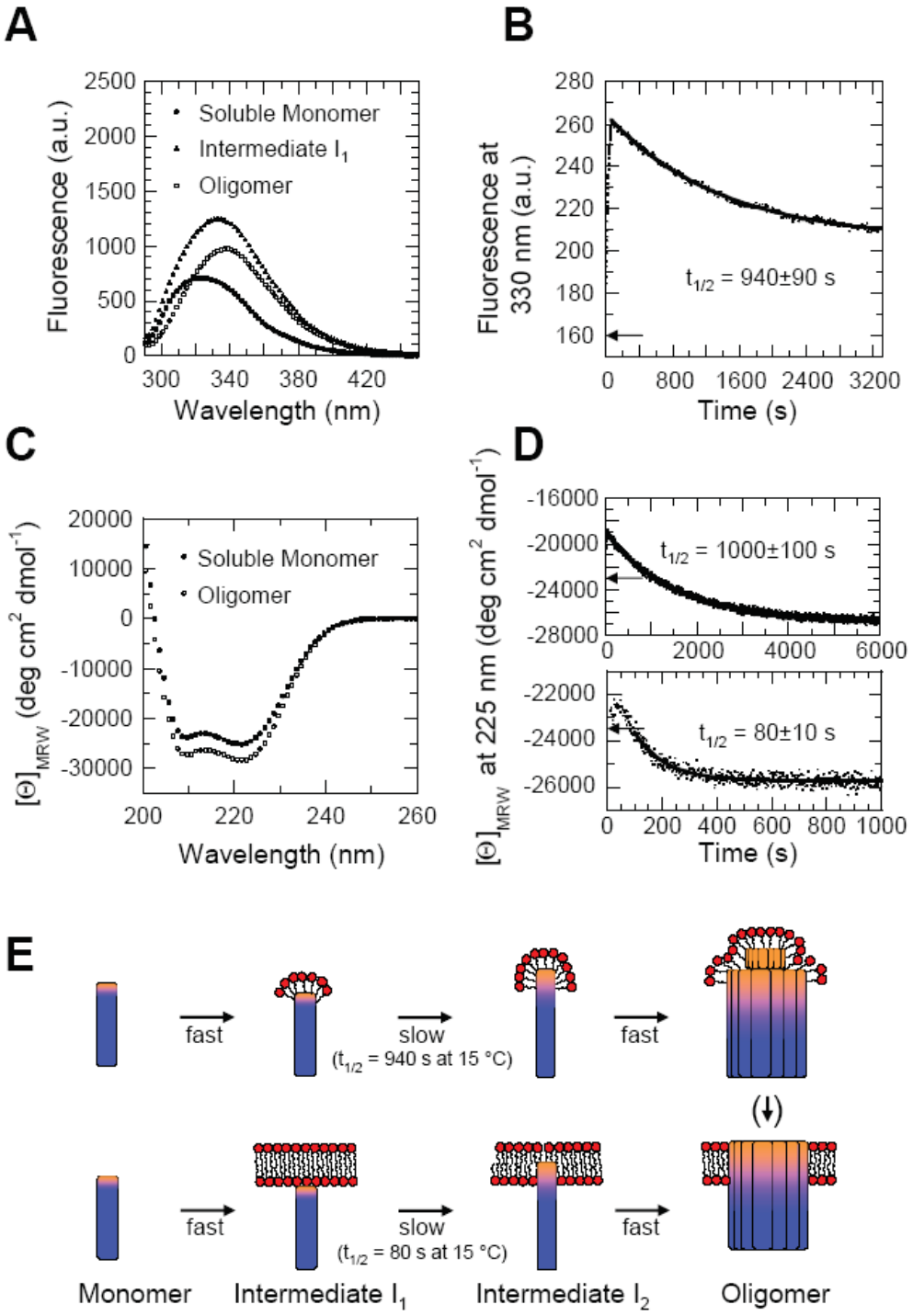

Figure 4.7: **Conformational changes during assembly of $ClyA_{red}$ followed by fluorescence and CD spectroscopy.** (A) Fluorescence emission spectra of $ClyA_{red}$. Spectra of the soluble monomer (in PBS), the monomeric intermediate I_1 (in PBS, 0.1% DDM), and oligomeric $ClyA_{red}$ (in PBS, 0.1% DDM) are shown. (B) Kinetics of assembly of $ClyA_{red}$ in DDM monitored by fluorescence. Oligomerization of $ClyA_{red}$ (5 μM) induced by 0.1% DDM was followed at 330 nm (15 °C). The line shows the fit of a monoexponential function omitting the first 100 s. The arrow indicates the signal of monomeric $ClyA_{red}$ in PBS at 330 nm. (C) Far-UV CD-spectra of monomeric and oligomeric $ClyA_{red}$. Spectra of the soluble monomer (in PBS), and oligomeric $ClyA_{red}$ (in PBS, 0.1(D) Kinetics of assembly of $ClyA_{red}$ in detergent and in erythrocyte membranes monitored by far-UV CD. Oligomerization of $ClyA_{red}$ induced by 0.1% DDM (upper panel) or erythrocyte membranes (lower panel) was followed at 225 nm (15 °C). The lines show the fit of monoexponential functions omitting the first 100 s. The arrows indicate the signal of monomeric $ClyA_{red}$ in PBS at 225 nm. (E) Proposed mechanism of assembly of ClyA. Monomeric ClyA quickly associates with detergent (upper row) or the membrane (lower row) and undergoes a structural change leading to the monomeric intermediate I_1. A second and much slower conversion yields the monomeric and assembly-competent intermediate I_2, which rapidly assembles into the oligomeric pore complex. The detergent-induced pore complex (with cap) converts to the membrane-embedded pore complex (without cap) upon detergent removal in the presence of lipids.

oligomeric (Atkins et al., 2000), or homogeneously oligomeric (Wai et al., 2003a). Our data confirm the observation of Wallace et al. (2000) that both $ClyA_{red}$ and $ClyA_{ox}$ are monomeric in solution. Furthermore, we find that $ClyA_{red}$ and $ClyA_{ox}$ oligomerize quickly upon contact with lipid or detergent and that both proteins display equal activity. From these results and the activity measurements of $ClyA_{ox}$ by Wai et al. (2003a and 2003b), we conclude that a movement of helix G away from the main body of the molecule is not required for assembly of ClyA into functional pore complexes as suggested by Atkins et al. (2000). The fact that we have obtained results that differ strikingly from those of other groups can be explained by the previously unknown high tendency of $ClyA_{ox}$ to form inactive aggregates (Supplementary Figure 4.9). If this phenomenon is not taken into account, the concentration of monomeric $ClyA_{ox}$ cannot be reliably determined, which in turn leads to large errors in activity assays.

We did not observe a role of the disulfide bond in the intrinsic ability of ClyA to assemble in target membranes *in vitro*. However, it seems likely that the disulfide bond plays a crucial role during export of ClyA from the bacterial cell, because Wai et al. (2003a) observed that *E. coli dsbA*$^-$ and *dsbB*$^-$ strains display a ClyA-dependent hemolytic phenotype on blood agar plates. DsbA and DsbB are required for efficient disulfide bond formation in the periplasm and could influence the vesicle-mediated export of ClyA by directly oxidizing ClyA and/or introducing disulfide bonds into components that participate in the formation of OMVs. In this context it should also be considered that integrity of the outer membrane may depend on proteins containing disulfide bonds (Braun and Silhavy, 2002; Wu et al., 2005). Absence of DsbA or DsbB could thus lead to destabilization of the outer membrane, which in turn could facilitate the release of OMVs.

4.4.2 Structure and assembly of the ClyA complex

The increase in total length upon transformation from soluble monomer (110 Å) to detergent induced ClyA complex (160 Å) and the significant changes observed in tryptophan fluorescence indicate that large structural transitions take place in the helix bundle of ClyA, as seen for many other PFTs (Czajkowsky et al., 2004; Song et al., 1996; Tilley et al., 2005; Zakharov and Cramer, 2002) As both tryptophans, W37 and W86, are located within the bundle and shielded from solvent in the structure of the monomer ($<$6% and $<$1% solvent accessible, respectively), the change in tryptophan fluorescence reflects a transition in tertiary structure, rather than surface contacts with detergent or neighbouring protomers. Far-UV CD spectra show that the high content in helical secondary structure is retained during assembly, suggesting that the final membrane channel is built mainly from α-helices.

While the overall structure of the ClyA pore complex is the same in detergent and in the lipid bilayer, the cap region appears to be sensitive to changes in the environment of the pore complex. The cap may emerge as the hydrophilic edges of the β-tongues of different subunits face each other to form one large 26-stranded β-barrel during membrane association and insertion. Concomitant with the conformational change of the β-tongue, adjacent amphipathic helices might rotate to expose their hydrophobic surface and to facilitate complete insertion of the pore complex in the bilayer. This conformational change might in turn induce register shifts in the four-helix bundle, leading to markedly elongated protomers. A similar mechanism is known for other α-helical toxins such as colicins and diphtheria toxin, where amphipathic helices are packed around a central hydrophobic helical hairpin that is thought to mediate the insertion into the membrane (Choe et al., 1992; Parker and Pattus, 1993). The distinct cap region is barely visible in membrane-embedded ClyA pores, suggesting further conformational changes upon formation of the final pore. However, individual top views often show a central mass density and occasionally side views exhibit a distinct cap. Therefore, the possibility should be considered that the cap functions as a flexible domain of the molecule that can be everted and exposed again to mediate docking of OMVs to the target cell membrane.

Based on our data we propose a simple model for ClyA assembly (Figure 4.7E). Monomeric ClyA associates in a very fast step with the lipid bilayer or the detergent molecules, and undergoes a first conformational change to intermediate I_1 (fast phase in Figures 4.7B, 7D). The rate-limiting step for assembly is the second, uni-molecular conformational transition, which generates assembly-competent monomers (intermediate I_2) that rapidly associate to the oligomeric complex. It remains elusive at which stage the marked elongation of

the protomer from 110 to 140 Å occurs and what the molecular basis for the increase in length is. The detailed elucidation of the large conformational changes during assembly will require a high-resolution structure of the pore complex.

4.5 Experimental procedures

4.5.1 Expression and purification of ClyA

The genetic sequence of ClyA was amplified by PCR from genomic DNA of *E. coli* W3110, and introduced into pET11a (Novagen). This plasmid was used to create the $(His)_6$-tagged ClyA variant (QuikChange, Stratagene), yielding plasmid pClyA. This plasmid promotes cytoplasmic expression of N-terminally $(His)_6$-tagged ClyA.
ClyA was expressed in the cytoplasm of *E. coli* Tuner (DE3) (Novagen) harboring plasmid pClyA, and purified by chromatography on Ni-NTA agarose and hydroxyapatite. The protein was fully reduced as shown by modification with Ellman's reagent (5,5'-dithio-bis(2'-nitrobenzoic acid)). Edman Sequencing and MALDI-TOF mass spectrometry confirmed the integrity of the protein. For preparation of $ClyA_{ox}$, 22 μM $ClyA_{red}$ were incubated in 50 mM Tris/HCl, 1 mM $CuCl_2$, pH 8.0 for 3 hours at 25 °C. Aggregated $ClyA_{ox}$ was removed by size exclusion chromatography in PBS (Dulbecco's phosphate buffered saline, pH 7.3) at 4 °C. Protein concentrations were determined by the extinction coefficients at 280 nm ($ClyA_{red}$ in PBS: 30300 $M^{-1}cm^{-1}$, $ClyA_{ox}$ in PBS: 30400 $M^{-1}cm^{-1}$).

4.5.2 Analytical gel filtration

Gel filtration was performed at 4 °C in PBS or PBS, 0.1% DDM using a Superdex 200 10/300 gel filtration column (GE Healthcare). To initiate assembly, ClyA (5 μM) was mixed with DDM and incubated in PBS, 0.1% DDM at 15 °C. At different times samples were withdrawn and subjected to chromatography.

4.5.3 Analysis of the redox state of ClyA in the membrane-bound form

For analysis of the redox state in the membrane-bound form, 250 nM ClyA were first incubated with a suspension of 1% (v/v) horse erythrocytes for 30 min at 37 °C, then treated with IAEDANS and finally analyzed by SDS-PAGE as described in Supplementary Figure 4.8 for the soluble protein.

4.5.4 Cross-linking

$ClyA_{red}$ (5 μM) was incubated in PBS, 0.1% DDM at 15 °C. After different incubation times (2-120 min) samples were mixed with DSP (final concentration 3 mM) and incubated for 5 min at 25 °C. The reaction was stopped by addition of TrisHCl, pH 8.0 (final concentration 100 mM). The samples were applied onto a 16% polyacrylamide-SDS gel. The areas of the monomeric $ClyA_{red}$ bands were quantified using densitometric analysis with the AlphaEase®Imaging System (AlphaInnotech).

4.5.5 Hemolysis assay

Hemolysis of defibrinated horse erythrocytes (Oxoid AG) was measured according to Rowe and Welch (1994). Briefly, 800 μl of a 1% solution ($2.19 \cdot 10^7$ cells/ml) of erythrocytes were mixed with 200 μl of various dilutions of ClyA in PBS (final concentrations 0.01-1000 nM), and incubated for 120 min under shaking at 37 °C. After centrifugation, the absorbance of the supernatant was determined at 540 nm. The kinetics of hemolysis were measured by monitoring the decrease in turbidity of a 0.1%suspension of erythrocytes upon addition of ClyA (final concentration 250 nM). The optical density at 650 nm was followed in a stirred cuvette at 37 °C.

4.5.6 Scanning transmission electron microscopy

A Vacuum Generators (East Grinstead) HB-5 STEM, interfaced to a modular computer system (Tietz Video and Image Processing Systems), was used. Samples were preparedon 200 mesh, gold-plated copper grids (Müller, 1992). Grids were washed to remove detergent and either negatively stained (2% uranyl acetate) for structural examination or plunge frozen and freeze-dried for mass measurement. Grids were imaged at recording doses between 500 and 600 electrons/nm^2 for the mass measurements (pixel size 0.85 nm) and between 3450 and 10250 electrons/nm^2 for the negative stain microscopy (pixel size 0.33 nm). Beam-induced mass-loss was corrected as detailed in Müller (1992), and tobacco mosaic virus (kindly provided by R. Diaz Avalos) was used for absolute mass calibration. Mass analysis was achieved

with the IMPSYS program package (Müller, 1992). Mass values were binned into a histogram and multiple Gauss curves were fitted. The overall experimental uncertainty of the results was estimated from the corresponding SE (SE = SD/$\sqrt{n}$) and the $\approx$ 5% uncertainty in the calibration of the instrument.

4.5.7 Transmission electron microscopy

Oligomerization of monomeric ClyA (5 μM) was induced by the addition of 0.1% DDM. The sample was incubated at 15 °C for 2 hours. ClyA particles were examined by adsorbing the sample on glow discharged 400 mesh carbon-coated Parlodion grids and negative-staining with 2% (w/v) uranyl acetate. Images were recorded at 50kx on Kodak SO-163 film using a Hitachi H-8000 microscope operating at an acceleration voltage of 200 kV. For cryo-EM the same sample was applied to 400 mesh copper grids with a thin continuous carbon film and quick frozen in liquid ethane. Grids were transferred into a Philipps CM200 FEG electron microscope operating at 200 kV. Cryo-electron micrographs were recorded on Kodak SO-163 film in plane and at a tilt angle of 15 °C.

4.5.8 Image processing

Negatives were digitized on a Heidelberg Primescan D 7100 drum scanner at a resolution of 4 Å/px for negatively stained samples and 2 Å/px for vitrified samples at the specimen level. The EMAN boxer program (Ludtke et al., 1999) was used to select 2699 images of top and 3620 images of side views as well as a total of 8451 particles from electron micrographs including all orientations present on tilted and untilted images. Projections negatively stained preparations were subjected to reference-free alignment (Penczek et al., 1992) and classification by multivariate statistical analysis (Frank et al., 1982) in SPIDER (Frank et al., 1996). Rotational power spectra of top view class averages were calculated with the Xmipp software (Sorzano et al., 2004) to determine the particle symmetry. EMAN was used to generate a starting volume from top and side views of the frozen-hydrated sample and for an initial refinement enforcing C13 symmetry. For further refinement by projection matching the SPIDER package was employed. The CTF was estimated using the ctffind and ctftilt programs (Mindell and Grigorieff, 2003) and corrected for phases and amplitudes applying a Wiener filter in SPIDER. The resolution of the refined volume containing 8429 particles was estimated by Fourier-shell correlation. All visualization was performed with DINO (http://www.dino3d.org), a structural biology visualization program developed by one of the authors (AP).

4.5.9 Formation of proteoliposomes

Brain lipids (Avanti Polar Lipids) were solubilized at a concentration of 5 mg/ml in PBS (Sigma) containing 1% n-octyl-β-D-glucopyranoside (OG) The mixture was dialyzed against PBS to remove all detergent from the lipid vesicles. Monomeric ClyA was added to the vesicles to give a final lipid-to-protein weight ratio of 5 and incubated at 4°C for 2 hours. Samples were then adsorbed to EM grids and analyzed with negative stain and cryo-EM. Alternatively, the detergent-induced pore complexes were reconstituted by mixing them with solubilized lipids and removing the detergent with Biobeads.

4.5.10 CD- and fluorescence spectroscopy

The ClyA concentration (monomer) was 5 μM in all experiments. Emission spectra were recorded on a Hitachi F-4500 fluorescence spectrometer at 22 °C, using an excitation wavelength of 280 nm. Spectra of oligomerized $ClyA_{red}$ were recorded after incubation in PBS, 0.1% DDM for 2 hours at 15 °C. A spectrum of the monomeric intermediate I_1 was recorded after 100 s of exposure to DDM at 15 °C. For fluorescence kinetics, the signal change at 330 nm upon addition of 0.1% DDM to $ClyA_{red}$ was followed at 15 °C. Far-UV CD spectra were recorded at 22 °C using a Jasco J-810 spectropolarimeter. For Far-UV CD kinetics, the signal change at 225 nm upon addition of DDM (0.1%) or erythrocyte membranes to $ClyA_{red}$ was followed at 15 °C. Erythrocyte membranes were prepared as described by van Leengoed and Dickerson (1992). Membranes from approx. $9{\cdot}10^7$ erythrocytes were used for each experiment (400 μl total volume). Spectra and kinetic traces were corrected for buffer contributions and converted to mean residue ellipticity.

4.6 Acknowledgements

We would like to thank Francoise Erne-Brand for recording the STEM data, René Brunisholz for Edman Sequencing and MALDI-TOF mass spectrometry, and Thomas Braun, Stefan Schauer, and Eilika Weber-Ban for inspiring discussions. This project was supported by the Schweizerische Nationalfonds (SNF) within the framework of the National Center of Competence in Research (NCCR) program in Structural Biology, the Maurice E. Müller Foundation of Switzerland, the NoE 3D-EM, EU project (LSHG-CT-2004-502828), and the SNF grant 3100-059415 to AE.

4.7 References

Atkins, A., Wyborn, N.R., Wallace, A.J., Stillman, T.J., Black, L.K., Fielding, A.B., Hisakado, M., Artymiuk, P.J. and Green, J. (2000) Structure-function relationships of a novel bacterial toxin, hemolysin E. The role of alpha G. J Biol Chem, 275, 41150-41155.

Braun, M. and Silhavy, T.J. (2002) Imp/OstA is required for cell envelope biogenesis in *Escherichia coli*. Mol Microbiol, 45, 1289-1302.

Choe, S., Bennett, M.J., Fujii, G., Curmi, P.M., Kantardjieff, K.A., Collier, R.J. and Eisenberg, D. (1992) The crystal structure of diphtheria toxin. Nature, 357, 216-222.

Czajkowsky, D.M., Hotze, E.M., Shao, Z. and Tweten, R.K. (2004) Vertical collapse of a cytolysin prepore moves its transmembrane beta-hairpins to the membrane. Embo J, 23, 3206-3215.

del Castillo, F.J., Leal, S.C., Moreno, F. and del Castillo, I. (1997) The *Escherichia coli* K-12 sheA gene encodes a 34-kDa secreted haemolysin. Mol Microbiol, 25, 107-115.

del Castillo, F.J., Moreno, F. and del Castillo, I. (2001) Secretion of the *Escherichia coli* K-12 SheA hemolysin is independent of its cytolytic activity. FEMS Microbiol Lett, 204, 281-285.

Dubochet, J., Adrian, M., Chang, J.J., Homo, J.C., Lepault, J., McDowall, A.W. and Schultz, P. (1988) Cryo-electron microscopy of vitrified specimens. Q Rev Biophys, 21, 129-228.

Frank, J., Radermacher, M., Penczek, P., Zhu, J., Li, Y., Ladjadj, M. and Leith, A. (1996) SPIDER and WEB: processing and visualization of images in 3D electron microscopy and related fields. J Struct Biol, 116, 190-199.

Frank, J., Verschoor, A. and Boublik, M. (1982) Multivariate statistical analysis of ribosome electron micrographs. L and R lateral views of the 40 S subunit from HeLa cells. J Mol Biol, 161, 107-133.

Gouaux, E. (1997) Channel-forming toxins: tales of transformation. Curr Opin Struct Biol, 7, 566-573.

Kerenyi, M., Allison, H.E., Batai, I., Sonnevend, A., Emody, L., Plaveczky, N. and Pal, T. (2005) Occurrence of hlyA and sheA genes in extraintestinal *Escherichia coli strains*. J Clin Microbiol, 43, 2965-2968.

Lai, X.H., Arencibia, I., Johansson, A., Wai, S.N., Oscarsson, J., Kalfas, S., Sundqvist, K.G., Mizunoe, Y., Sjostedt, A. and Uhlin, B.E. (2000) Cytocidal and apoptotic effects of the ClyA protein from *Escherichia coli* on primary and cultured monocytes and macrophages. Infect Immun, 68, 4363-4367.

Ludtke, S.J., Baldwin, P.R. and Chiu, W. (1999) EMAN: semiautomated software for high-resolution single-particle reconstructions. J Struct Biol, 128, 82-97.

Ludwig, A., Bauer, S., Benz, R., Bergmann, B. and Goebel, W. (1999) Analysis of the SlyA-controlled expression, subcellular localization and pore-forming activity of a 34 kDa haemolysin (ClyA) from *Escherichia coli* K-12. Mol Microbiol, 31, 557-567.

Ludwig, A., Tengel, C., Bauer, S., Bubert, A., Benz, R., Mollenkopf, H.J. and Goebel, W. (1995) SlyA, a regulatory protein from *Salmonella typhimurium*, induces a haemolytic and pore-forming protein in *Escherichia coli*. Mol Gen Genet, 249, 474-486.

Ludwig, A., von Rhein, C., Bauer, S., Huttinger, C. and Goebel, W. (2004) Molecular analysis of cytolysin A (ClyA) in pathogenic *Escherichia coli* strains. J Bacteriol, 186, 5311-5320.

Mindell, J.A. and Grigorieff, N. (2003) Accurate determination of local defocus and specimen tilt in electron microscopy. J Struct Biol, 142, 334-347.

Müller, S.A., Goldie, K. N., Bürki, R., Häring, R., and Engel, A. (1992) Ultramicroscopy.

Oscarsson, J., Mizunoe, Y., Li, L., Lai, X.H., Wieslander, A. and Uhlin, B.E. (1999) Molecular analysis of the cytolytic protein ClyA (SheA) from *Escherichia coli*. Mol Microbiol, 32, 1226-1238.

Oscarsson, J., Mizunoe, Y., Uhlin, B.E. and Haydon, D.J. (1996) Induction of haemolytic activity in *Escherichia coli* by the slyA gene product. Mol Microbiol, 20, 191-199.

Oscarsson, J., Westermark, M., Lofdahl, S., Olsen, B., Palmgren, H., Mizunoe, Y., Wai, S.N. and Uhlin, B.E. (2002) Characterization of a pore-forming cytotoxin expressed by *Salmonella enterica serovars typhi* and *paratyphi* A. Infect Immun, 70, 5759-5769.

Parker, M.W., Buckley, J.T., Postma, J.P., Tucker, A.D., Leonard, K., Pattus, F. and Tsernoglou, D. (1994) Structure of the Aeromonas toxin proaerolysin in its water-soluble and membrane-channel states. Nature, 367, 292-295.

Parker, M.W. and Feil, S.C. (2005) Pore-forming protein toxins: from structure to function. Prog Biophys Mol Biol, 88, 91-142.

Parker, M.W. and Pattus, F. (1993) Rendering a membrane protein soluble in water: a common packing motif in bacterial protein toxins. Trends Biochem Sci, 18, 391-395.

Penczek, P., Radermacher, M. and Frank, J. (1992) Three-dimensional reconstruction of single particles embedded in ice. Ultramicroscopy, 40, 33-53.

Riddles, P.W., Blakeley, R.L. and Zerner, B. (1983) Reassessment of Ellman's reagent. Methods Enzymol, 91, 49-60.

Rowe, G.E. and Welch, R.A. (1994) Assays of hemolytic toxins. Methods Enzymol, 235, 657-667.

Saxton, W.O. and Baumeister, W. (1982) The correlation averaging of a regularly arranged bacterial cell envelope protein. J Microsc, 127 (Pt 2), 127-138.

Soderblom, T., Oxhamre, C., Wai, S.N., Uhlen, P., Aperia, A., Uhlin, B.E. and Richter-Dahlfors, A. (2005) Effects of the *Escherichia coli* toxin cytolysin A on mucosal immunostimulation via epithelial Ca^{2+} signalling and Toll-like receptor 4. Cell Microbiol, 7, 779-788.

Song, L., Hobaugh, M.R., Shustak, C., Cheley, S., Bayley, H. and Gouaux, J.E. (1996) Structure of staphylococcal alpha-hemolysin, a heptameric transmembrane pore. Science, 274, 1859-1866.

Sorzano, C.O., Marabini, R., Velazquez-Muriel, J., Bilbao-Castro, J.R., Scheres, S.H., Carazo, J.M. and Pascual-Montano, A. (2004) XMIPP: a new generation of an open-source image processing package for electron microscopy. J Struct Biol, 148, 194-204.

Tilley, S.J., Orlova, E.V., Gilbert, R.J., Andrew, P.W. and Saibil, H.R. (2005) Structural basis of pore formation by the bacterial toxin pneumolysin. Cell, 121, 247-256.

Tweten, R.K., Parker, M.W. and Johnson, A.E. (2001) The cholesterol-dependent cytolysins. Curr Top Microbiol Immunol, 257, 15-33.

van Leengoed, L.A. and Dickerson, H.W. (1992) Influence of calcium on secretion and activity of the cytolysins of Actinobacillus pleuropneumoniae. Infect Immun, 60, 353-359.

Wai, S.N., Lindmark, B., Soderblom, T., Takade, A., Westermark, M., Oscarsson, J., Jass, J., Richter-Dahlfors, A., Mizunoe, Y. and Uhlin, B.E. (2003a) Vesicle-mediated export and assembly of pore-forming oligomers of the enterobacterial ClyA cytotoxin. Cell, 115, 25-35.

Wai, S.N., Westermark, M., Oscarsson, J., Jass, J., Maier, E., Benz, R. and Uhlin, B.E. (2003b) Characterization of dominantly negative mutant ClyA cytotoxin proteins in *Escherichia coli*. J Bacteriol, 185, 5491-5499.

Wallace, A.J., Stillman, T.J., Atkins, A., Jamieson, S.J., Bullough, P.A., Green, J. and Artymiuk, P.J. (2000) *E. coli* hemolysin E (HlyE, ClyA, SheA): X-ray crystal structure of the toxin and observation of membrane pores by electron microscopy. Cell, 100, 265-276.

Wu, T., Malinverni, J., Ruiz, N., Kim, S., Silhavy, T.J. and Kahne, D. (2005) Identification of a multicomponent complex required for outer membrane biogenesis in *Escherichia coli*. Cell, 121, 235-245.

Zakharov, S.D. and Cramer, W.A. (2002) Colicin crystal structures: pathways and mechanisms for colicin insertion into membranes. Biochim Biophys Acta, 1565, 333-346.

4.8 Supplementary information

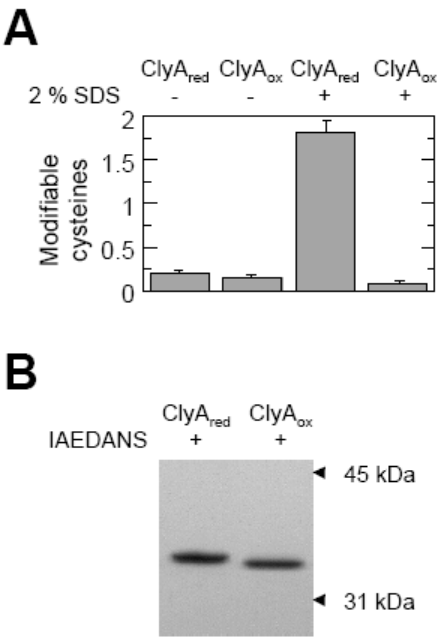

Figure 4.8: Supplementary Figure. **Analysis of the redox state of the two cysteines of ClyA.** The redox state of $ClyA_{ox}$ and $ClyA_{red}$ was verified with Ellman's reagent in (A) under native conditions in 50 mM Tris/HCl, pH 8.0, and under denaturing conditions in 50 mM Tris/HCl, 2% SDS, pH 8.0 according to Riddles et al. (1983). Error bars represent the mean standard deviations resulting from triplicate samples. Interestingly, the two cysteine thiols of $ClyA_{red}$ reacted quantitatively with Ellman's reagent only under denaturing conditions (Figure A, lanes 1 and 3). This implies that the cysteines of ClyA in solution are buried. (B) visualizes the redox state of $ClyA_{red}$ and $ClyA_{ox}$ by SDS-PAGE after labeling of free cysteines under denaturing conditions with 5-((((2-iodoacetyl)amino)ethyl)-amino)naphthalene-1-sulfonic acid (IAEDANS), which adds a mass of 850 Da to $ClyA_{red}$, but not to $ClyA_{ox}$. For SDS-PAGE analysis ClyA was incubated in 100 mMTris/HCl, 1.5% SDS, 5% glycerol, 0.5 mM EDTA, 0.0025% bromphenol blue, 50 mM IAEDANS, pH 6.8 for 5 min at 95°C and applied onto a 12% polyacrylamide-SDS gel.

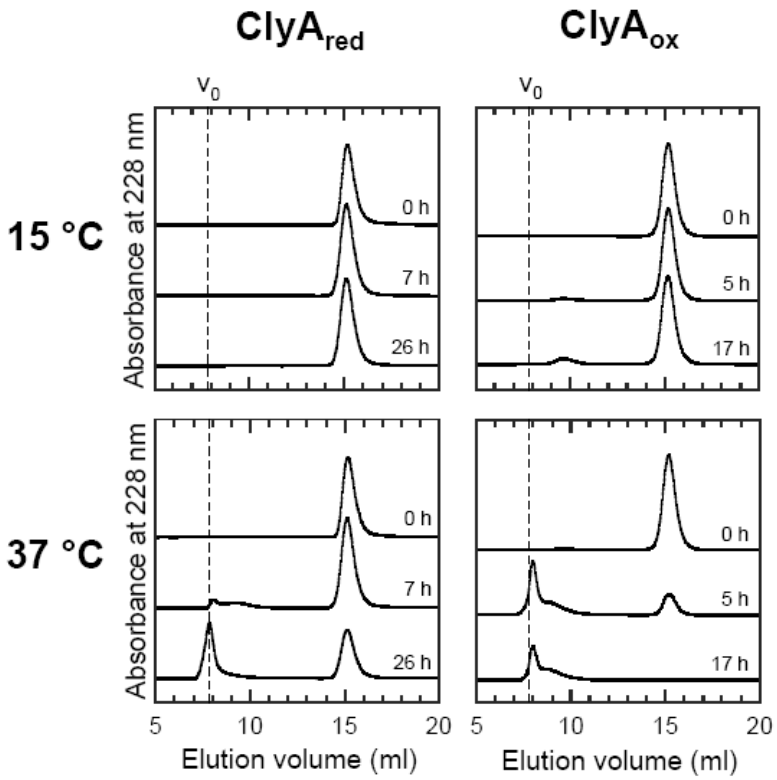

Figure 4.9: Supplementary Figure. **Unspecific aggregation of reduced and oxidized ClyA in PBS.** Analytical size exclusion chromatography with $ClyA_{red}$ and $ClyA_{ox}$. Samples (5 μM each) were incubated in PBS at different temperatures during the indicated times prior to analysis. Both $ClyA_{red}$ and $ClyA_{ox}$ are stable at 15 °C but are prone to aggregation at elevated temperature. $ClyA_{ox}$ aggregates faster than $ClyA_{red}$ at 37 °C.

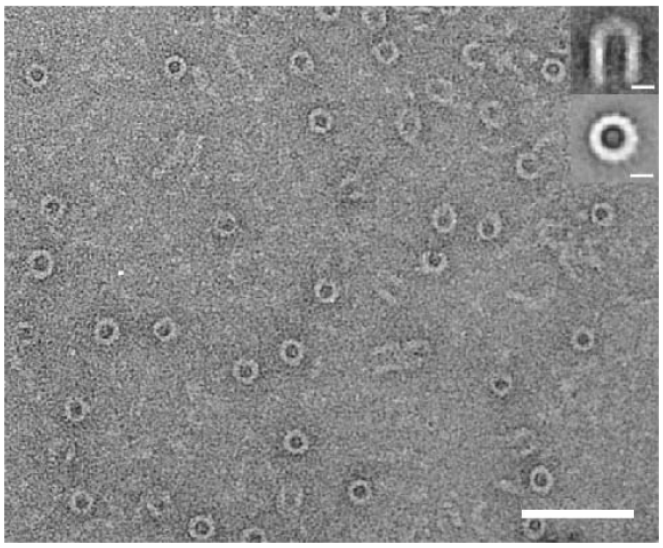

Figure 4.12: Supplementary Figure. **Detergent-induced oligomerization of $ClyA_{ox}$.** Electron-micrograph of negatively stained $ClyA_{ox}$particles. Monomeric $ClyA_{ox}$was oligomerizedby adding 0.1 % DDM and examined in the electron microscope. The scale bar corresponds to 50 nm. The insets show top and side view class averages, comprising 157 selected top views and 73 selected side views which were reference free aligned. The scale bars in the insets correspond to 5 nm.

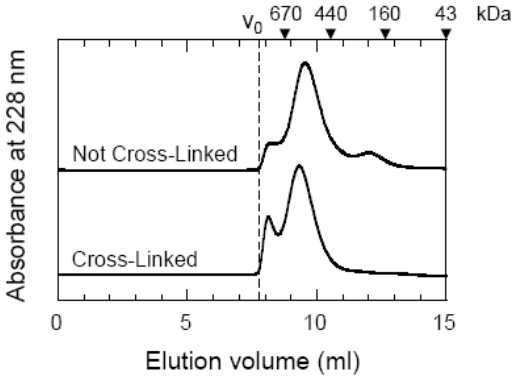

Figure 4.10: Supplementary Figure. **Analytical gel filtration profiles of cross-linked $ClyA_{red}$ pores and untreated pore complexes.** As shown in Figure 4.3B, SDS-PAGE was used to analyze the cross-linking products during DDM-induced oligomerization. Resolution of high molecular masses in SDS-PAGE is however very limited. Thus, the band on top of the gel could in principle represent either cross-linked soluble oligomers or unspecifically aggregated protein. In order to distinguish between these possibilities, a sample identical to that in Figure 4.3B, lane 6,was analyzed by size exclusion chromatography in PBS, 0.1% DDM (lower elution profile) and compared to an equivalent sample that had not been cross-linked (upper elution profile). Arrows denote the retention volumes of soluble marker proteins with indicated masses. v_0, void volume.

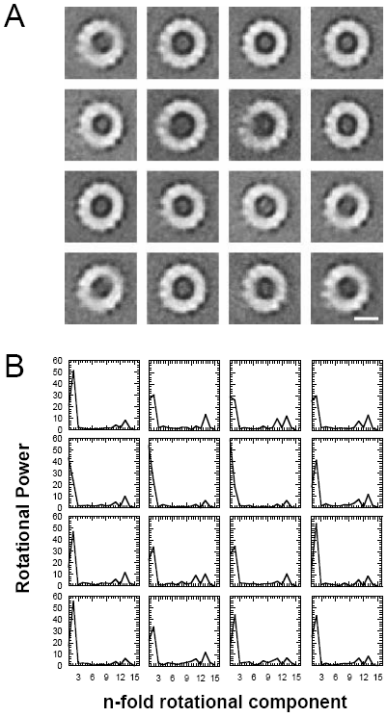

Figure 4.11: Supplementary Figure. **Oligomeric state of $ClyA_{red}$.** (A) Correspondence Analysis with SPIDER of 2876 negatively stained top views yielded 16 class averages containing between 82 and 260 particles. The scale bar corresponds to 5 nm. (B) Rotational power spectra of top view class averages were calculated with the Xmipp software (Sorzano et al., 2004) indicating a 13-fold symmetry for all averages.

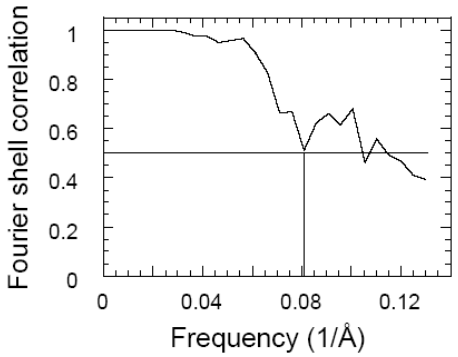

Figure 4.13: Supplementary Figure. **Fourier shell correlation plot.** To assess the resolution of the 3D map of the $ClyA_{red}$ pore, a Fourier shell correlation was calculated (Saxton and Baumeister, 1982) employing the SPIDER software. The correlation cutoff at 0.5 yielded a resolution of 12 Å.

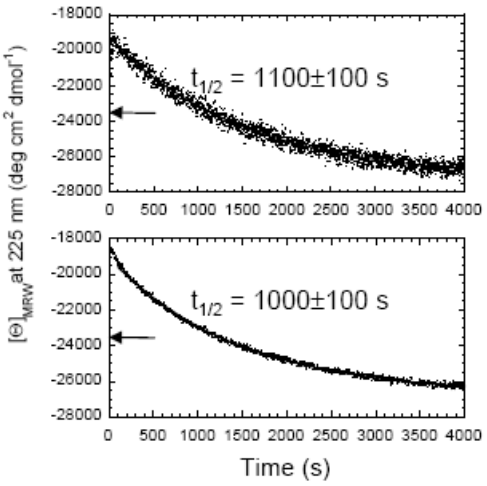

Figure 4.14: Supplementary Figure. **Kinetics of $ClyA_{red}$ assembly in detergent at different protein concentrations.** Oligomerization of 2.5 μM (upper panel) and 10 μM $ClyA_{red}$ (lower panel) induced by 0.1% DDM was monitored at 15°C by far-UV CD at 225 nm. The lines show fits to mono-exponential functions omitting the first 100 s. The arrows indicate the CD signal of monomeric $ClyA_{red}$ in PBS.

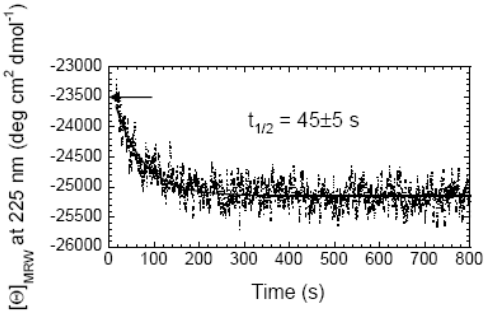

Figure 4.15: Supplementary Figure. **Kinetics of assembly of $ClyA_{red}$ in erythrocyte membranes at 37 °C.** Oligomerization of $ClyA_{red}$(5 μM) induced by erythrocyte membranes was followed by far-UV CD at 225 nm. The line shows a fit to a mono-exponential function. The arrow indicates the CD signal of monomeric $ClyA_{red}$in PBS.

Chapter 5

Oligomeric structure of the Bacillus subtilis cell division protein DivIVA determined by transmission electron microscopy

Henning Stahlberg[1,4,5], Eva Kutejova[2,5], Karina Muchova [2], **Marco Gregorini**[1], Ariel Lustig[1], Shirley A. Müller[1], Vesna Olivieri[1], Andreas Engel[1], Anthony J. Wilkinson[3], Imrich Barák[2]

5.1 Abstract

DivIVA from *Bacillus subtilis* is a bifunctional protein with distinct roles in cell division and sporulation. During vegetative growth, DivIVA regulates the activity of the MinCD complex thus helping to direct cell division to the correct mid-cell position. DivIVA fulfills quite a different role during sporulation in *B. subtilis* when it directs the *oriC* region of the chromosome to the cell pole prior to the asymmetric cell division. DivIVA is a 19.5 kDa protein with a large part of its structure predicted to form a tropomyosin-like α helical coiled-coil. Here we present a model for the quaternary structure of DivIVA, based on cryo-negative stain transmission electron microscopy images. The purified protein appears as an elongated particle with lateral expansions at both ends producing a form that resembles a 'doggy-bone'. The particle mass estimated from these images agrees with the value of 145 kDa measured by analytical ultracentrifugation suggesting 6-8 mers. These DivIVA oligomers serve as building blocks in the formation of higher order assemblies giving rise to 'strings', 'wires' and finally two-dimensional lattices in a time-dependent manner.

5.2 Introduction

The molecular mechanisms of cell division have been intensively studied for several decades, the best characterized systems being those operating in the rod-shaped bacteria *Escherichia coli* and *Bacillus subtilis*. Despite these efforts, many basic questions remain unanswered. For example the mechanism that ensures the correct placement of the division septum, a key aspect of bacterial cell division, is only partly understood. The protein FtsZ plays a pivotal role in the temporal and spatial control of symmetric division at the mid-cell site in almost all bacteria, as well as division at polar sites in bacteria that divide asymmetrically during their life cycle. FtsZ is homologous to the eukaryotic tubulins, and forms cytokinetic rings (Z-rings) at the sites of cell division (Bi and Lutkenhaus, 1991). Z-ring formation is the earliest known step in bacterial cell division and takes place well before cell membrane invagination and complete nucleoid separation (Bi

[1]M.E.Müller Institute, Biozentrum, University of Basel, Klingelbergstrasse 50/70, CH-4056 Basel, Switzerland

[2]Institute of Molecular Biology, Slovak Academy of Sciences, Dúbravská cesta 21, 845 51 Bratislava 45, Slovakia

[3]Department of Chemistry, University of York, Heslington, York, Y01 50D, U.K

[4]Present address: Molecular & Cellular Biology, UC-Davis, CA 95616, USA

[5]These authors contributed equally.

and Lutkenhaus, 1991).

FtsZ-ring formation, and thus the selection of the site of division, is controlled by at least two mechanisms; nucleoid occlusion and inhibition by the Min system (Harry, 2001). The nucleoid occlusion model states that the nucleoid has a negative effect on division wherever it occupies space in the cell. Thus, the mid-cell site appears and disappears cyclically during vegetative growth with rounds of chromosome replication (Errington et al., 2003). Although the nucleoid occlusion model (Woldringh et al., 1991) is very attractive it is still poorly defined.

A principal function of the Min system is to prevent division at the cell poles. In *E. coli*, it comprises three components, MinC, MinD and MinE. MinC and MinD form a complex that prevents cell division by inhibiting FtsZ polymerization and Z-ring formation. MinE is a topological factor allowing relief of division inhibition in the central region of the cell (de Boer et al., 1992). Recent localization experiments in living cells have revealed that MinD, which is a membrane-associated ATPase (de Boer et al., 1991), oscillates from pole to pole (Raskin and de Boer, 1999a,b). The period of this remarkable oscillation is 10-20 seconds. The division inhibitor MinC is also observed to oscillate from pole to pole, and as it oscillates with the same pattern as MinD, and only does so in the presence of MinD, the proteins probably co-oscillate as a MinC-MinD complex (Raskin and de Boer, 1999a; Hu and Lutkenhaus, 1999). MinE was originally thought to form a mid-cell, ring-like structure, defining the site of subsequent FtsZ ring assembly (Raskin and de Boer, 1997). However, in living cells MinE also undergoes a rapid oscillation coupled to that of MinD and MinC (Fu et al., 2001). The oscillating movements of MinD and MinE are mutually dependent because lack of MinE leads to a uniform distribution of the MinCD complex around the cytoplasmic membrane (Rowland et al., 2000). In addition, it has been shown recently that the three Min proteins are organized into extended membrane-associated coiled structures that wind around within the cell between the two poles (Shih et al., 2003). Thus, the pole-to-pole oscillation of the proteins reflects oscillatory changes in their distribution within the coiled structure.

Although the cell division processes in *E. coli* and *B. subtilis* are fundamentally similar, Bacilli appear to employ a different strategy on initiating mid-cell division. *B. subtilis* has MinCD homologues but lacks a MinE counterpart and the MinCD complex does not oscillate between the cell poles. Instead, MinCD is recruited to the division site by a 19.5 kDa cytoplasmatic protein, DivIVA (Cha and Stewart, 1997; Edwards and Errington, 1997; Marston et al., 1998). DivIVA has no sequence similarity to MinE and the two proteins function differently (Zhang et al., 1998). DivIVA forms large oligomers (Muchova et al., 2002) whereas MinE is a dimer (Zhang et al., 1998).

Comparison of the ways that Gram-negative and Gram-positive bacteria regulate mid-cell site selection during binary fission, reveals that fundamentally different schemes have evolved. Binary fission involves not only identification of the mid-cell and the construction of a septum at this site, but also rejection of other (polar) sites for the assembly of the cell division apparatus. In addition to nucleoid occlusion, which probably pertains in all bacteria, prokaryotes also control division site selection using the Min system. This system seems to have evolved in three basic ways, through MinE oscillation, through DivIVA regulation and by a third uncharacterized mechanism. The latter conclusion is based on the observation that bacterial species such as *Caulobacter*, *Mycoplasma* and *Heamophilus*, lack recognizable Min homologues (Margolin, 2001). However, completed genome sequence data suggest that the problem is more complicated. In *Clostridium acetobutylicum* and *Clostridium difficile*, both *minE* and *divIVA* genes are present (Stragier, 2001) although it is not established whether *minE* is functional in these organisms and how it and *divIVA* contribute to mid-cell site selection.

The *B. subtilis* DivIVA/MinCDdivision system appears to have no direct role in the initiation of FtsZ ring formation at the mid-cell site, rather it inhibits division at the polar sites. DivIVA has another function during endospore formation, a developmental process that begins with an asymmetric septation, giving rise to a larger mother cell and a smaller prespore. In this process the role of DivIVA is not in regulation of division site selection, instead it functions in prespore chromosome segregation (Thomaides et al., 2001). Taken together, the main roles of DivIVA seem to be (i) to direct the MinCD complex to polar sites during vegetative growth and (ii) through direct or indirect interaction with RacA, to help anchor chromosomes to the poles during sporulation (Ben-Yehuda et al., 2003; Yu and Errington, 2003). As DivIVA may interact

with alternative proteins as mentioned above, it is possible that their competition somehow triggers polar division.

In this paper we present the quaternary structure of a biologically active variant of DivIVA (DivIVA9) determined by cryo-negative stain transmission electron microscopy. The experiments demonstrate that elongated protein particles as small as 130 kDa can be imaged individually, using cryo-negative stain TEM. The possible role of observed DivIVA structure for its biological function is discussed with aim to explain the extraordinary manner how this protein recognizes the cell poles.

5.3 Results

5.3.1 DivIVA and its mutant derivatives expression, isolation and purification

All experiments were performed with two different mutant variants of DivIVA, DivIVA9 and DivIVA2, described previously in (Muchova et al., 2002). These point mutations, leading to Glu162Lys and Leu120Pro substitutions respectively, were acquired during attempts to over-express recombinant DivIVA in *E. coli*. The *divIVA9* gene is stable in the *E. coli* expression system in contrast to the wild type *divIVA gene*, which acquires mutations and deletions (Muchova et al., 2002). In *B. subtilis*, the *divIVA9* allele does not cause any detectable defects in cell growth or morphology. Thus, it is reasonable to assume that wild type DivIVA and DivIVA9 are functionally and structurally similar proteins.

DivIVA9 was purified by Q Sepharose Fast Flow, Mono Q and gel filtration chromatography as described in *Experimental procedures*. The retention volume of the protein on the gel filtration column suggests a species with a molecular weight somewhere between those of the 158 kDa and 2 000 kDa standards (Figure 5.1). A very similar gel filtration profile was observed with a hexa-histidine tagged derivative of DivIVA9 (not shown). Purified DivIVA9 precipitates if stored at -20 °C even in 10% glycerol. At high protein concentrations, it also precipitates at 4 °C (Muchova et al., 2002). Indeed, at a concentration of 10 mg/ml, DivIVA9 precipitates from solution over a period of several minutes at 4 °C. At the lower concentration of 4 mg/ml, precipitation is much slower taking place over several days.

The second mutant protein, DivIVA2, which is associated with severe defects in cell division and sporulation (Muchova et al., 2002), was isolated as a hexa-histidine tagged form on a Ni-NTA agarose column. Its retention volume on the Superose 12 column was significantly higher than that of DivIVA9 and its hexa-histidine tagged derivative suggesting a much smaller species. Together the results imply that there is a significant difference between the oligomeric states of DivIVA9 and DivIVA2. This difference in the quaternary structure of the proteins may correlate with the different *in vivo* effects of the *divIVA9* and *divIVA2* alleles.

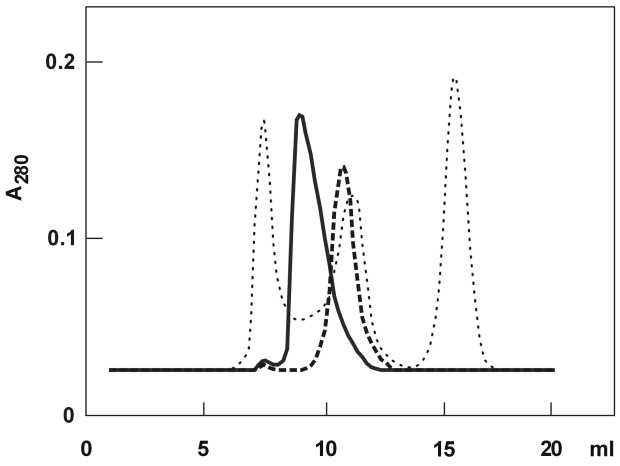

Figure 5.1: **Superose 12 gel filtration chromatograms of DivIVA proteins.** The continuous line represents DivIVA9 and the dashed line His_6-tagged DivIVA2. In each experiment a 0.5 ml sample was loaded containing either DivIVA9 at 2.6 mg/ml or His_6-tagged DivIVA2 at 2.2 mg/ml. The dotted line is the chromatogram of molecular weight standards: Blue dextran (2 000 kDa), aldolase (158 kDa) and cytochrome C (12.5 kDa).

5.3.2 Transmission electron microscopy imaging of DivIVA9 and DivIVA2 mutant proteins

Transmission electron microscopy (TEM) of samples quick-frozen in the presence of an ammonium molybdate stain (Adrian et al., 1998) was employed to analyze DivIVA immediately after purification and at a series of later times. In other TEM experiments, either unstained cryo samples in fenestrated carbon film (Dubochet et al., 1988), or samples negatively stained with uranyl acetate or phosphotungstic acid (PTA), were prepared and examined. Unstained cryo TEM was unable to produce usable images of DivIVA, due to the small size and weight of the complexes. While faint elongated particles could be observed in the negatively

stained TEM samples imaged at room temperature (data not shown), the better resolution and signal-to-noise ratio of images obtained by cryo-negative stain TEM were needed for the oligomeric protein structures to be visualized clearly.

Cryo-negative stain TEM images of freshly purified DivIVA9 samples showed the presence of elongated particles with lateral expansions at both ends, making them resemble in some sense 'doggy-bones'. These particles were observed in all samples imaged within 1-3 days of protein purification (Figure 5.2A-C). The flexible structures have a length of 22.4 $\pm$ 3.0 nm and a width of 2.9 $\pm$ 0.3 nm ($n = 16$). In contrast, TEM images of His-tagged DivIVA2 samples revealed diffuse objects without distinct shape and there was no evidence of aggregation even after the stock had been stored for several days at 8°C (Figure 5.2D). When stored in the same way, DivIVA9 slowly aggregates (see below).

To examine the possibility of further DivIVA9 oligomerization, cryo-negatively stained samples were prepared after storage of the protein for up to 5 days at 8°C. While samples stored for 2 days contained single 'doggy-bone' shaped particles (Figure 5.2), the TEM images of samples prepared at later time points showed higher order structures (Figure 5.3). The end-to-end oligomerization of two 'doggy-bone' shaped particles was frequently observed (Figure 5.3A). The end-to-end contacts of the 'doggy-bones' sometimes had a slight lateral displacement. We also observed 'strings' of linearly associated 'doggy-bone' particles, laterally associated strings forming thin 'wires' (Figure 5.3B), and two-dimensional networks of doggy-bone particles (Figure 5.3C). These exhibit the same contrast as the individual 'doggy-bone' particles, suggesting that the networks are single-layered two-dimensional ribbons rather than three-dimensional bundles. The Fourier transform computed for the marked region of the two-dimensional network shown in (Figure 5.3C) is displayed in the inset. The diffraction spots prove the existence of an ordered real-space lattice in the image, with 2D-crystal dimensions of $u = 24$ nm, $v = 10$ nm and an opening angle, α of 117°. Sometimes two-dimensional networks with neighboring 'doggy-bone' particles displaced along the longer crystal axis were observed. In these instances the ends of some DivIVA particles establish contact not with the ends but the centers of others (Figure 5.4C). Older samples frequently showed mixtures of different oligomeric forms, and the incidence of the higher order oligomers was higher than before storage. This higher order oligomerization could be reversed by the addition of 200 mM $(NH_4)_2SO_4$ and incubation for 1 hour at 8°C, prior to sample preparation. Subsequent TEM imaging then again revealed mostly individual 'doggy-bone' shaped particles. In the presence of 200 mM $(NH_4)_2SO_4$, the non-aggregated 'doggy-bone' complex was stable for several days at 8°C (Figure 5.2B).

5.3.3 Estimation of oligomerization state of DivIVA9 by analytical ultracentrifugation

To determine the oligomerization state of the DivIVA9 'doggy-bones', sedimentation measurements were made in the analytical ultracentrifuge (AUC). The experiments were carried out in ammonium sulphate buffer as described in *Experimental procedures*. A single sedimentation velocity (SV) run at a protein concentration of 0.4 mg/ml revealed a single boundary with an $S_{20,W}$ value of 2.7. Several sedimentation equilibrium (SE) runs at 10 000 and 14 000 rpm made over a protein concentration range of 0.4 mg/ml to 0.1 mg/ml showed a strong concentration dependence of the measured mass, which varied from 104 kDa to 134 kDa. The extrapolated molecular weight at a concentration of zero mg/ml was 145 $\pm$ 10 kDa. The ratio of the frictional coefficient (f) calculated for the protein concentration of 0.4 mg/ml (M=104 kDa, s=2.7 S) to that of a rigid sphere (f_0) was 2.95 with a hydrodynamic radius of 9.2 nm. A value of f/f_0 of 1 corresponds to an ideal spherically shaped protein. The extremely high f/f_0 value obtained for DivIVA9 indicates that the particle shape has a high aspect ratio. The AUC results suggest that the DivIVA9 protein forms elongated 6-8 mers under the conditions employed. This observation is in contrast to our previous analytical ultracentrifugation results, which suggested that the mass of DivIVA9 increases from that expected for a dimer to one corresponding to a 12-mer (Muchova et al., 2002). The possible explanation for the observed discrepancy might be the use of different buffers in the two experiments. As documented by the TEM experiments, ammonium sulfate disrupts the end-to-end contact of pairs of 'doggy-bone' particles, which would lead to the 10-12 mer previously observed in AUC experiments (Muchova et al., 2002).

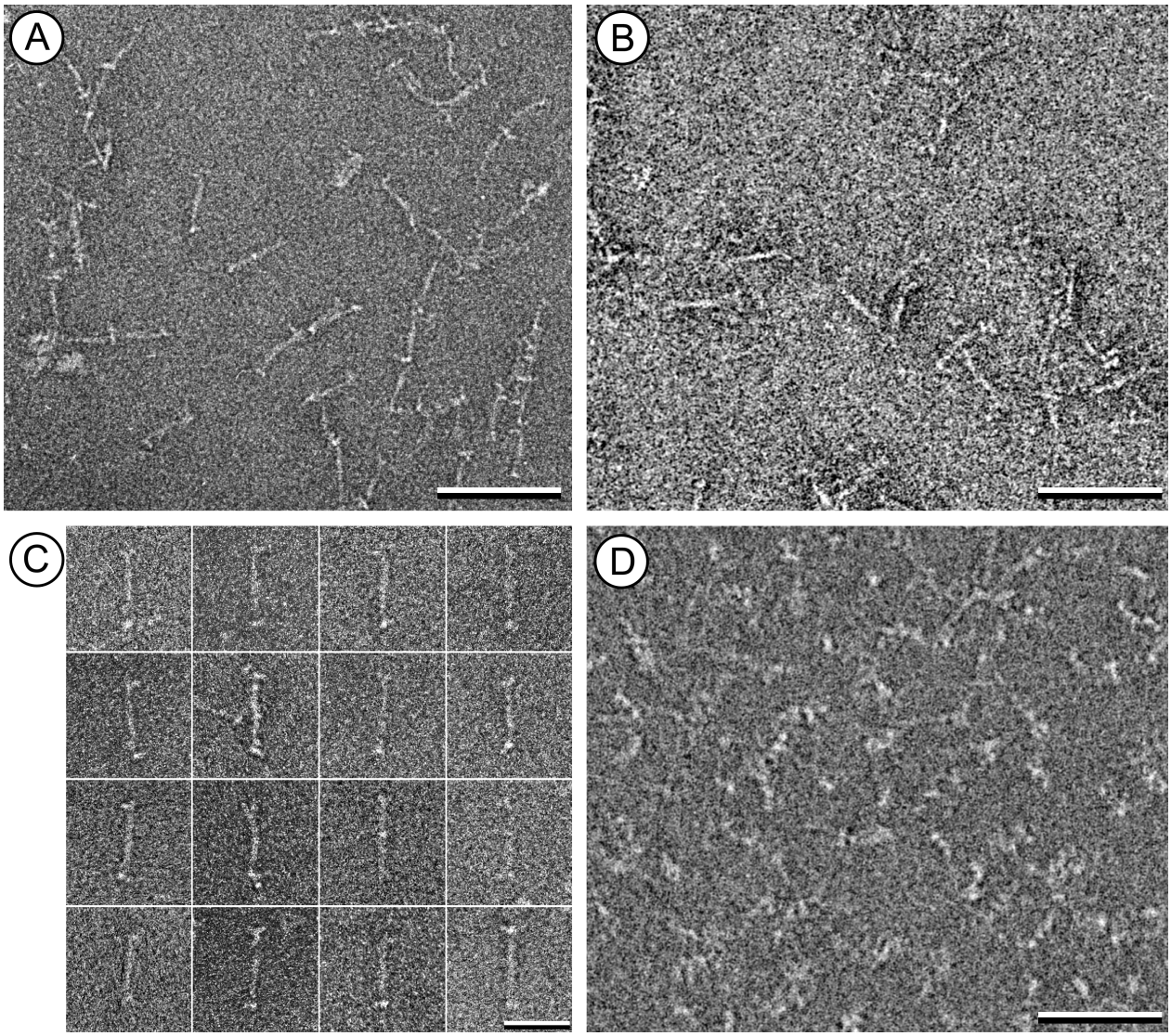

Figure 5.2: **Cryo-negative stain TEM images of DivIVA.** (A) DivIVA9, freshly purified and imaged within two days. (B) DivIVA9, purified and stored for 3 days at 8°C in 200 mM $(NH_4)_2SO_4$. (C) Examples of 'doggy-bone' shaped particles, as found in (A) and (B) (D) Cryo-negative stain image of His_6-tagged DivIVA2 that had been purified and subsequently stored for 5 days at 8°C. Scale bar for (A), (B) and (D) is 50 nm, for (C) is 20 nm.

5.3.4 Oligomerization state of the 'doggy-bone' structures indicated by microscopy

As noted above, the 'doggy-bone' complexes evident on TEM images recorded from purified DivIVA9 samples were 22.4 $\pm$ 3.0 nm long and 2.9 $\pm$ 0.3 nm wide. A cylindrical rod of the same length and diameter would have a volume of 145 $\pm$ 31 nm^3. Taking the average density of protein to be 810 Da/nm^3, this would correspond to a mass of 117 $\pm$ 24 kDa. Taking into account the lateral expansions at both ends, this is in agreement with the 'doggy-bone' being a DivIVA9 6-8 mer (monomer mass of 19.5 kDa). It is probable that the DivIVA9 protomers are in extended conformations, spanning the length of the 'doggy-bone'. DivIVA9 has 164 amino acid residues. If these take up the anticipated extended α helical structure they would have a length 24.6 nm, in good agreement with the length of the long axis of the 'doggy-bone'. The scanning transmission electron microscope (STEM) was employed in a further series of experiments aimed at directly measuring the mass of the 'doggy-bone' complexes. The microscopy grids were prepared using material that had been stored for a period of weeks in the presence of 200 mM $(NH_4)_2SO_4$ at 8°C. Images recorded from negatively stained (PTA) samples using the STEM, documented the continued presence of elongated particles (data not shown). In the absence of stain,

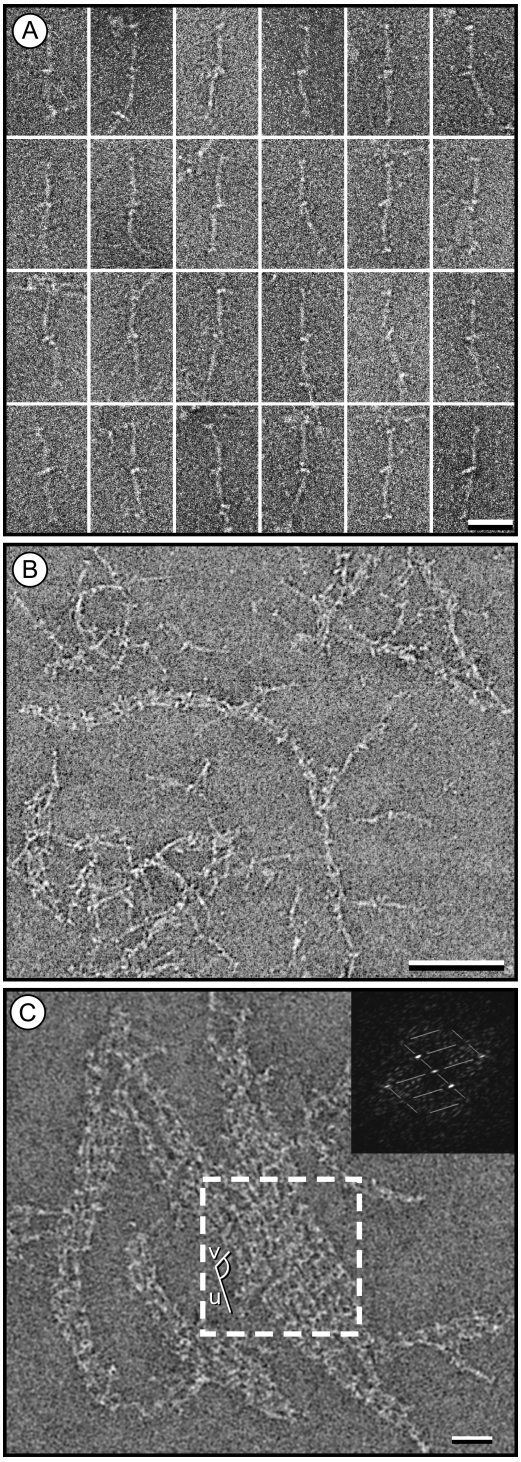

Figure 5.3: **Cryo-negative stain TEM images of DivIVA9, stored at 8°C in the absence of $(NH_4)_2SO_4$.** (A) Examples of 'doggy-bone' pairs, that can frequently be observed two days after purification, (B) 3 days after purification; the 'doggy-bone' shaped particles arrange in 'strings', (C) After 5 days; two-dimensional networks are formed. The indicated area of the two-dimensional network shown was computationally Fourier transformed. The corresponding power-spectrum is reproduced in the inset (top right), revealing the presence of a real-space lattice with dimensions u = 24 nm, v = 10 nm, $\alpha = 117°$. These real-space lattice vectors are indicated in the image. Scale bar for (A) is 20 nm, for (B) is 50 nm, and for (C) is 20 nm.

the elongated structures could only rarely be distinguished with certainty and attempts to measure their mass failed to give a statistically representative result. Nevertheless, the mass of 63 elongated particles less than 26 nm long could be roughly estimated and was 133 ± 62 kDa. The mass-per-length (MPL) could also be determined for 42 of these, being 3.6 ± 1.7 kDa/nm ($n = 41$) and 9.6 kDa/nm ($n = 1$). Although of little statistical significance, the results imply that the approximately 22 nm long 'doggy-bone' particles imaged by TEM were not DivIVA dodecamers, as indicated earlier by AUC experiments made in the absence of $(NH_4)_2SO_4$ (Muchova et al., 2002). Further, the MPL of approximately 4 kDa/nm measured for some of the elongated particles supports a hexameric stoichometry (expected value 4.8 kDa/nm assuming the above conformation).

5.4 Discussion

In this study, TEM images of DivIVA9 revealed 'doggy-bone' shaped oligomers that further assemble into two-dimensional networks. Since the divIVA9 allele has no effect on cell division and sporulation (Muchova et al., 2002), it is reasonable to propose that wild type DivIVA forms the same oligomers and networks as DivIVA9. In contrast, the His_6-tagged DivIVA2 protein, which fails to form 'doggy-bone' shaped oligomers, has great impact on these processes in *B. subtilis*. The His_6-tagged form of DivIVA9 showed the same behavior in gel filtration experiments as the untagged protein (Figure 5.1), indicating the formation of similarly elongated particles as observed for DivIVA9. These experiments as well as previous characterization of DivIVA2 protein without His_6-tag (Muchova et al., 2002), are suggesting that in DivIVA2 the failure to oligomerize the way as DivIVA9 does, is not due to the presence of the His_6-tag. According to the AUC results, the 'doggy-bone' complexes are formed by 6-8 copies of the 19.5 kDa DivIVA9 protein.

The elongated shape of the 'doggy-bone' complex (22.4 ± 3.0 nm long and 2.9 ± 0.3 nm wide) explains the discrepancy between the molecular mass estimated from the gel filtration experiments and that measured by AUC. Being an elongated particle, DivIVA9 elutes at a much lower volume than a spherical particle of equivalent mass (Figure 5.1).

A scheme for the oligomerization of DivIVA is presented in (Figure 5.4), in which masked parti-

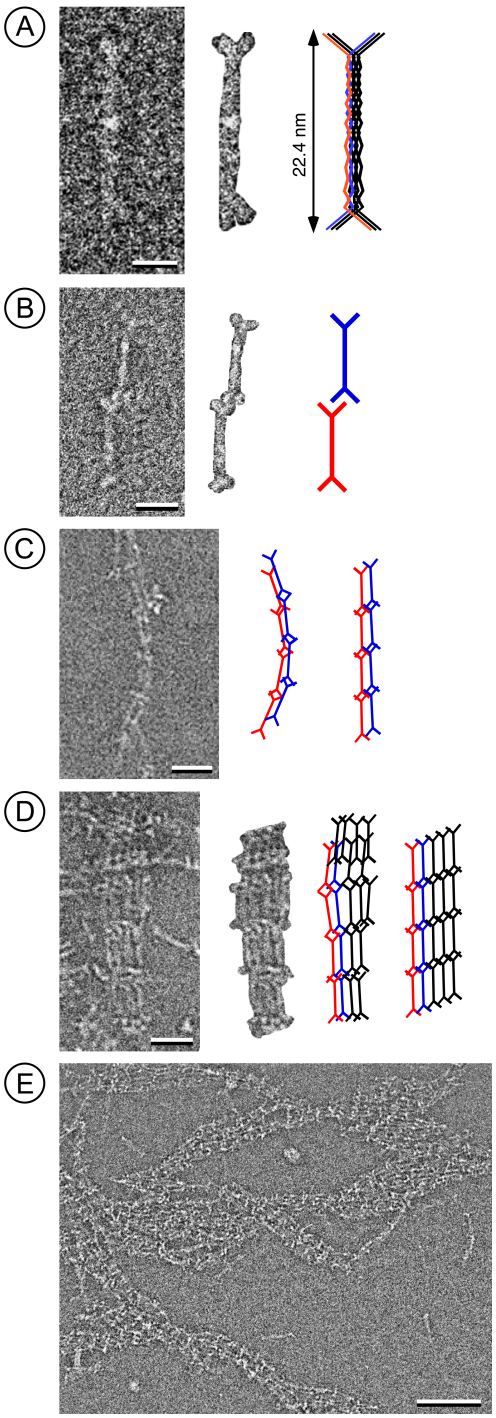

Figure 5.4: **Tentative scheme of DivIVA9 oligomerization.** (A) Freshly purified DivIVA9 appears as 'doggy-bone' shaped particles 22.4 ± 3 nm long and 2.0 ± 0.4 nm wide (left). A masked particle is reproduced to guide the reader's eyes (centre). A tentative model for the hexameric oligomer (right). (B) 'Doggy-bone' particles oligomerize end-to-end, to form pairs. A lateral displacement was sometimes observed, as in the example shown (left). Masked particle (center). Model (right). (C) Further end-to-end oligomerization gives rise to 'strings' (D) Several strings attach laterally in a plane to form thin 'wires' (left). Models (center and right). (E) Further aggregation leads to two-dimensional network formation. Scale bar for (A) is 5 nm, for (B) is 10 nm, for (C) and (D) is 20 nm, and for (E) is 50 nm.

cles from the cryo-negative stain TEM images are shown alongside tentative models of the 'doggy-bone' oligomer and its assemblies. Our data indicate that 'doggy-bone' aggregation starts with the formation of end-to-end dimers, (Figure 5.4B). This would account for the 10-12 mers, seen previously in analytical ultracentrifugation experiments run in the absence of ammonium sulphate (Muchova et al., 2002). Oligomerization continues with the formation of 'strings', thin 'wires' (Figure 5.3C), and two-dimensional 'networks' (Figures 5.4D and 5.4E). As indicated at the upper end of the model in (Figure 5.4D), DivIVA 'doggy-bones' occasionally establish end-to-centre contacts, giving rise to staggered two-dimensional networks where neighboring oligomers are displaced along their long crystal axis.

The observed oligomerization is unlikely to have been influenced by the cryo-negative stain sample preparation method, since network formation is time dependent. Further, since the 'doggy-bone' shaped DivIVA9 particles are building blocks for the higher aggregates, this conformation must exist in solution and cannot be an artifact of the 30 seconds exposure to ammonium molybdate during the staining procedure.

The oligomerization, and lattice forming properties exhibited by DivIVA9 in this study may be significant for the biological function of the wild type protein. Other cell division proteins form two-dimensional or three-dimensional networks, the best known example being FtsZ. FtsZ forms Z rings at sites of septation (Bi and Lutkenhaus, 1991), though in *B. subtilis* it can also appear in the form of spirals as the Z-ring migrates from the mid-cell site to the two polar positions at the beginning of sporulation (Ben-Yehuda and Losick, 2002). FtsZ has a strong propensity to polymerize in a GTP-dependent manner in vitro, forming structures that include sheets and filaments (Bramhill and Thompson, 1994). FtsZ is a weak homologue of tubulin, which forms micro-filamentous structures that provide either a track along which proteins can be translocated or an anchor to which proteins of the cytoskeleton of eukaryotic cells can attach. Interestingly, DivIVA is a homologue of tropomyosin, an actin-binding protein that forms coiled-coil filaments (Whitby et al., 1992). The highly ordered oligomeric structures formed by DivIVA may be crucial for anchoring different proteins enabling DivIVA to control complex processes such as cell division and sporulation in Gram-positive bacteria.

The ability of DivIVA to form 6-8 mers and two-dimensional networks may be crucial for both vegetative and asymmetric cell division. Lewis and Harry (2003) and Hamoen and Errington (2003) have shown that DivIVA localization to the poles is independent on FtsZ localization. However, a dependence of DivIVA localization on the mid-cell localization of FtsZ and other division proteins including DivIB, DivIC (Marston et al., 1998) and PBP 2B (Daniel et al., 2000; Hamoen and Errington, 2003) has been reported previously. How DivIVA oligomers become sequestered to the polar sites is not yet known. The requirement of FtsZ and PBP 2B for polar targeting of DivIVA during vegetative growth seems to be indirect and probably only arises because of their role in the formation of the new cell pole. The polar localization of DivIVA is also independent of the cytoskeletal proteins Mbl and MreB (Hamoen and Errington, 2003). Taken together, it seems that in contrast to mid-cell localization, polar localization of DivIVA does not need any known cell division or cytoskeletal protein. Similarly, the DivIVA homologue from *Streptomyces coelicolor* specifically recognizes hyphal tips in a septation independent manner enabling it to either establish or maintain the cell polarity that is needed for tip extension (Flärdh, 2003). It is possible that DivIVA can recognize some general feature of cell poles as *B. subtilis* DivIVA can target poles in both *E. coli* and *Schizosaccharomyces pombe*, neither of which have DivIVA-like proteins (Edwards et al., 2000). These observations suggest an intriguing function for DivIVA-like proteins as morphogenes capable of creating the cell polarity needed for sporulation in *B. subtilis*, tip extension in *S. coelicolor* and/or polar growth in many actinomycetes.

Our results suggest tentative structural explanations for how DivIVA recognizes the cell poles. One possibility is that the two-dimensional DivIVA networks specifically recognize some characteristic of the cell's morphology, for example by developing a curvature that precisely matches that of the cell poles. Another possibility is that DivIVA oligomers are directed to the poles by recently proposed 'activity-based structures', or hyperstructures, in which a various types of molecule are brought together to perform a function at a specific part of the membrane (Norris et al., 2002a; Norris et al., 2002b). Such hyperstructures may be responsible for differentiating the membrane at the cell pole from the rest of the cell membrane, so providing a means to control cell processes such as DNA replication and cell division. Subsequently, DivIVA sequesters other specific proteins to these sites. These hypotheses may have a great impact on our understanding of how bacterial proteins can be targeted to specific sites by recognizing physical characteristics of cell shape.

5.5 Experimental procedures

5.5.1 Bacterial strains and plasmids

Escherichia coli MM294 (Backman et al., 1976), BL21(DE3) (Novagen), IB706 (Muchova et al., 2002), IB884 (this work) and IB886 (this work) strains were grown in Luria-Bertani LB rich medium supplemented with 100 mg/ml ampicillin or 30 mg/ml kanamycin where appropriate. pET15IVA2 and pET15IVA9 plasmids were constructed by ligating the *divIVA2* and *divIVA9* coding sequences from pETIVA2 and pETIVA9, respectively (Muchova et al., 2002) into pET-15b (Novagen) at the *Nde*I and *Bam*HI sites. The resulting recombinant plasmids were used to transform *E. coli* BL21 (DE3) to create strains IB884 and IB886, respectively.

5.5.2 Isolation and purification of DivIVA9 protein

The isolation and purification of DivIVA9 was carried out essentially as reported previously (Muchova et al., 2002). Briefly, 3.5 g IB706 cells in 10 ml buffer A (50 mM Tris/HCl pH 8.0, 100 mM NaCl, 1 mM EDTA, 1 mM DTT, 1 mM AEBSF) were lysed by sonication and the cell debris was removed by centrifugation at 100 000 g for 30 min. The supernatant was applied to a 13 ml Q Sepharose Fast Flow column (Pharmacia Biotech) and DivIVA9 was eluted with a 91 ml 0.1 - 0.4 M NaCl linear gradient in buffer A. Fractions containing DivIVA9 were diluted fivefold with buffer A and loaded on to an FPLC Mono Q HR 10/16 column (Pharmacia Biotech) which was developed with a 70 ml 0.1 - 0.3 M NaCl gradient in buffer A. DivIVA9 fractions were concentrated by Centricon K10 filtration and loaded (500ml) onto a Superose 12 column (Pharmacia Biotech). Pure DivIVA9 fractions were then either used directly for electron microscopy studies or concentrated to 0.4 mg/ml. For the AUC and for some TEM experiments, $(NH_4)_2SO_4$ (pH 8.0)

was added to a final concentration 0.2 M. All procedures were carried out at 4°C. DivIVA9 protein with a His_6 tag at its N-terminus was isolated as for the His-tagged DivIVA2 (see below).

5.5.3 Isolation and purification of DivIVA2 protein

Because of the instability of DivIVA2, this mutant was isolated with a His_6-tag at the N-terminus using Ni-NTA agarose chromatography. 3.5 g induced IB884 cells in 10 ml buffer A were lysed by sonication and the soluble fraction was collected after centrifugation at 200 000 g for 12 min. The supernatant was applied to a 1 ml Ni-NTA agarose (QIAGEN) column. After washing the column with 5 ml 40 mM imidazole in buffer B (20 mM Tris/HCl pH 8.0, 150 mM NaCl, 20% glycerol), His_6-tagged DivIVA2 was eluted with 0.3 M imidazole in buffer B and desalted on a NAP5 column (Pharmacia Biotech) into buffer A. All procedures were carried out at 4°C.

5.5.4 Analytical ultracentrifugation

Analytical ultracentrifugation analysis was performed on purified DivIVA9 samples in 20 mM Tris/HCl pH 8.0, 200 mM $(NH_4)_2SO_4$, 100 mM NaCl. Sedimentation velocity (SV) and sedimentation equilibrium (SE) runs were carried out in a Beckman XLA analytical ultracentrifuge, equipped with absorption optics. The SV runs were performed at 54 000 rpm and 20°C using a 12 mm double sector cell. The SE runs were made at 10 000 and 14 000 rpm, 20°C and scanned at two wavelengths, 278 nm and 230 nm. The SE results were analyzed using a floating baseline computer program that adjusts the baseline absorbance to obtain lnA versus r^2, where A is the absorbance and r the radial distance. A partial specific volume of 0.73 cm^3/g and a solution density of ρ=1.012 g/cm^3 was used. A solution viscosity of 1.02 centipoise was taken for the conversion of S to $S_{20,W}$. The total conversion factor including the solution density was 1.05.

5.5.5 Transmission electron microscopy

The purified DivIVA sample was prepared for cryo-negative stain TEM as described (Adrian et al., 1998). A 3 μl drop of the sample was put on a TEM grid that had been coated with a fenestrated carbon film. This grid was then placed face down on a drop of 100 μl saturated ammonium molybdate solution, pH 7.5 for 30 seconds. The grid was then blotted, quick-frozen in liquid ethane cooled liquid nitrogen, and transferred with a Gatan-626 cryo-holder into a Philips CM200FEG microscope operated at 120 kV or 200 kV. Images were recorded at nominal magnifications of 50 kx to 115 kx on Kodak SO-163 photographic film, which was subsequently developed for 12 minutes in full strength developer. The negatives were scanned into a computer with a Heidelberg Primescan 7100 for further processing.

5.5.6 Scanning transmission electron microscopy

The mass measurements were made on a DivIVA9 sample that had been stored in the presence of 200 mM ammonium sulphate for several weeks at 8°C. The sample was diluted 1:3 with quartz double-distilled water, after which a 7 ml aliquot was adsorbed to a STEM microscopy grid; gold coated copper grid covered by a thick fenestrated carbon film and finally a thin carbon layer. The grid was then washed on 4 drops of quartz double-distilled water and freeze-dried overnight in the microscope. The sample was diluted by the same amount for the negative stain STEM and the grid similarly prepared except that the water washes were omitted. Instead the grid was negatively stained on 2 droplets of 2% uranyl acetate and air-dried.

A Vacuum Generators STEM HB-5 interfaced to a modular computer system (Tietz Video and Image Processing Systems GmbH, D-8035 Gauting) was employed. The dark-field images required for mass measurement were recorded from the unstained sample at an accelerating voltage of 80 kV. The nominal magnification was 200 kx. Recording doses were in the range of 1000 electrons/nm^2. The 512 x 512 pixel digital images were evaluated using the program package IMPSYS as outlined previously (Lupas et al., 1995; Müller et al., 1992). The mass-per-length evaluated from images recorded on the same day from tobacco mosaic virus (kindly supplied by Dr. R. Diaz-Avalos, Institute of Molecular Biophysics, Florida State University, Tallahassee, FL 32306) adsorbed to a separate grid, served as a calibration standard. Further, the DivIVA9 data were corrected for beam induced mass-loss based on the behavior of 4 proteins with an average mass of 159 $\pm$ 32 kDa. Subsequently, the mass val-

ues were displayed in histograms and described by Gauss curves. Images were recorded from the negatively stained sample at the nominal magnification of 200 kx and 80 kV accelerating voltage.

5.6 Acknowledgements

This work was supported by a Wellcome Trust Grants (grant numbers 066732/Z/01/Z to IB and AJW and 057339/Z/99/Z to AJW), a grant from the Slovak Academy of Sciences (grant number 2/1004/21 to IB), by the Swiss National Foundation (grant number NF 31-59415.99 to AE), the M. E. Müller-Foundation of Switzerland and the European Union-Quality of Life and Management of Living Resources Project (grant number QLRT-2000-00778 to AE).

5.7 References

Adrian, M., Dubochet ,J., Fuller, S.D. and Harris, J.R. (1998) Cryo-negative staining. Micron 29: 145-160.

Backman, K., Ptashne, M. and Gilbert, A.W. (1976) Construction of plasmids carrying the cI gene of bacteriophage lambda. Proc Natl Acad Sci USA 73: 4174-4178.

Ben-Yehuda, S. and Losick, R. (2002) Asymmetric cell division in B. subtilis involves a spiral-like intermediate of the cytokinetic protein FtsZ. Cell 109: 257-266.

Ben-Yehuda, S., Rudner, D.Z. and Losick, R. (2003) RacA, a bacterial protein that anchors chromosomes to the cell poles. Science 299: 532-536.

Bi, E.F. and Lutkenhaus, J. (1991) FtsZ ring structure associated with division in *Escherichia coli*. Nature 354: 161-164.

Bramhill, D. and Thompson, C.M. (1994) GTP-dependent polymerization of *Escherichia coli* FtsZ protein to form tubules. Proc Natl Acad Sci USA 91: 5813-5817.

Cha, J.H. and Stewart, G.C. (1997) The divIVA minicell locus of *Bacillus subtilis*. J Bacteriol 179: 1671-1683.

Daniel, R.A., Harry, E.J. and Errington, J. (2000) Role of penicillin-binding protein PBP 2B in assembly and functioning of the division machinery of *Bacillus subtilis*. Mol Microbiol 35: 299-311.

de Boer, P.A., Crossley, R.E., Hand, A.R. and Rothfield, L.I. (1991) The MinD protein is a membrane ATPase required for the correct placement of the *Escherichia coli* division site. EMBO J 10: 4371-4380.

de Boer, P.A., Crossley, R.E. and Rothfield, L.I. (1992) Roles of MinC and MinD in the site-specific septation block mediated by the MinCDE system of *Escherichia coli*. J Bacteriol 174: 63-70.

Dubochet, J., Adrian, M., Chang, J.-J., Homo, J.-C., Lepault, J., McDowall, A.W. and Schultz, P. (1988) Cryo-electron microscopy of vitrified specimens. Quat Rev Biophys 21: 129-228.

Edwards, D.H. and Errington, J. (1997) The *Bacillus subtilis* DivIVA protein targets to the division septum and controls the site specificity of cell division. Mol Microbiol 24: 905-915.

Edwards, D.H., Thomaides, H.B. and Errington, J. (2000) Promiscuous targeting of *Bacillus subtilis* cell division protein DivIVA to division sites in *Escherichia coli* and fission yeast. EMBO J 19: 2719-2727.

Errington, J., Daniel, R.A. and Scheffers, D.J. (2003) Cytokinesis in bacteria. Microbiol. Mol Biol Rev 67: 52-65.

Flärdh, K. (2003) Essential role of DivIVA in polar growth and morphogenesis in *Streptomyces coelicolor* A3(2). Mol Microbiol 49: 1523-1536.

Fu, X., Shih, Y.L., Zhang, Y. and Rothfield, L.I. (2001) The MinE ring required for proper placement of the division site is a mobile structure that changes its cellular location during the *Escherichia coli* division cycle. Proc Natl Acad Sci USA 98: 980-985.

Hamoen, L.W. and Errington, J. (2003) Polar targeting of DivIVA in *Bacillus subtilis* is not directly dependent on FtsZ or PBP 2B. J Bacteriol 185: 693-697.

Harry, E.J. (2001) Bacterial cell division: Regulating Z-ring formation. Mol Microbiol 40: 795-803.

Harry, E.J. and Lewis, P.J. (2003) Early targeting of Min proteins to the cell poles in germinated spores of *Bacillus subtilis*: Evidence for division apparatus-independent recruitment of Min proteins to the division site. Mol Microbiol 47: 37-48.

Hu, Z. and Lutkenhaus, J. (1999) Topological regulation of cell division in *Escherichia coli* involves rapid pole to pole oscillation of the division inhibitor MinC under the control of MinD and MinE. Mol Microbiol 34: 82-90.

Lupas, A., Müller, S., Goldie, K., Engel, A.M., Engel, A. and Baumeister, W. (1995) Model structure of the Omp alpha rod, a parallel four-stranded coiled coil from the hyperthermophilic eubacterium *Thermotoga maritima*. J Mol Biol 248: 180-189.

Margolin, W. (2001) Spatial regulation of cytokinesis in bacteria. Curr Opin Microbiol 4: 647-652.

Marston, A.L., Thomaides, H.B., Edwards, D.H., Sharpe, M.E. and Errington, J. (1998) Polar localization of the MinD protein of *Bacillus subtilis* and its role in selection of the mid-cell division site. Genes Dev 12: 3419-3430.

Muchova, K., Kutejova, E., Scott, D.J., Brannigan,

J.A., Lewis, R.J., Wilkinson, A.J. and Barak, I. (2002) Oligomerization of the *Bacillus subtilis* division protein DivIVA. Microbiol 148: 807-813.

Müller, S., Goldie, K.N., Bürki, R., Häring, R. and Engel, A. (1992) Factors influencing the precision of quantitative scanning transmission electron microscopy. Ultramicroscopy 46: 317-334.

Norris, V., Demarty, M., Raine, D., Cabin-Flaman, A. and Le Sceller, L. (2002a) Hypothesis: Hyperstructures regulate initiation in *Escherichia coli* and other bacteria. Biochimie 84: 341-347.

Norris, V., Misevic, G., Delosme, J.M. and Oshima, A.(2002) Hypothesis: A phospholipid translocase couples lateral and transverse bilayer asymmetries in dividing bacteria. J Mol Biol 318: 455-462.

Raskin, D.M. and de Boer, P.A. (1997) The MinE ring: an FtsZ-independent cell structure required for selection of the correct division site in *E. coli*. Cell 91: 685-694.

Raskin, D.M. and de Boer, P.A. (1999a) MinDE-dependent pole-to-pole oscillation of division inhibitor MinC in *Escherichia coli*. J Bacteriol 181: 6419-6424.

Raskin, D.M. and de Boer, P.A. (1999b) Rapid pole-to-pole oscillation of a protein required for directing division to the middle of *Escherichia coli*. Proc Natl Acad Sci USA 96: 4971-4976.

Rowland, S.L., Fu, X., Sayed, M.A., Zhang, Y., Cook, W.R. and Rothfield, L.I. (2000) Membrane redistribution of the *Escherichia coli* MinD protein induced by MinE. J Bacteriol 182: 613-619.

Shih, Y-L., Le, T. and Rothfield, L. (2003) Division site selection in *Escherichia coli* involves dynamic redistribution of Min proteins within coiled structures that extend between the two cell poles. Proc Natl Acad Sci USA 100: 7865-7870.

Stragier, P. (2001) A gene odyssey: Exploring the genomes of endospore-forming bacteria. In *Bacillus subtilis* and its Relatives: from Genes to Cell.

Sonenshein, A.L., Losick, R. and Hoch, J.A. (eds.). Washington, DC: American Society for Microbiology, pp. 519-525.

Thomaides, H.B., Freeman, M., El Karoui, M. and Errington, J. (2001) Division site selection protein DivIVA of *Bacillus subtilis* has a second distinct function in chromosome segregation during sporulation. Genes Dev 15: 1662-1673.

Whitby, F.G., Kent, H., Stewart, F., Stewart, M., Xie, X., Hatch, V., Cohen, C. and Phillips, G.N., Jr. (1992) Structure of tropomyosin at 9 Ångstroms resolution. J Mol Biol 227: 441-452.

Woldringh, C.L., Mulder, E., Huls, P.G. and Vischer, N. (1991) Toporegulation of bacterial division according to the nucleoid occlusion model. Res Microbiol 142: 309-320.

Wu, L.J. and Errington, J. (2003) RacA and the Soj-Spo0J system combine to effect polar chromosome segregation in sporulating *Bacillus subtilis*. Mol Microbiol 49: 1463-1475.

Zhang, Y., Rowland, S., King, G., Braswell, E. and Rothfield, L. (1998) The relationship between hetero-oligomer formation and function of the topological specificity domain of the *Escherichia coli* MinE protein. Mol Microbiol 30: 265-273.

Chapter 6

Immunogenicity and structural characterisation of an in vitro folded meningococcal siderophore receptor (FrpB, FetA)

Jeroen Kortekaas[1], Shirley A. Müller[2], Philippe Ringler [2], **Marco Gregorini**[2], Vincent E. Weynants[3], Lucy Rutten[4], Martine P. Bos[1], Jan Tommassen[1]

6.1 Abstract

The iron-limitation-inducible protein FrpB of *Neisseria meningitidis* is an outer-membrane-localized siderophore receptor. Because of its abundance and its capacity to elicit bactericidal antibodies, it is considered a vaccine candidate. Bactericidal antibodies against FrpB are, however, type-specific. Hence, an FrpB-based vaccine should comprise several FrpB variants to be capable of providing broad protection. To facilitate the development of a meningococcal subunit vaccine, we have established a procedure to obtain large quantities of the protein in a native-like conformation. The protein was expressed without its signal sequence in *Escherichia coli*, where it accumulated in inclusion bodies. After *in vitro* folding, the protein was biochemically, biophysically and immunologically characterized. Our results show that *in vitro* folded FrpB assembles into oligomers, presumably dimers, and that it induces high levels of bactericidal antibodies in laboratory animals.

Keywords: *In vitro* folding, outer membrane protein, vaccine

Abbreviations used: CFU, colony-forming units; EDDHA, ethylenediamine di-o-hydroxyphenylacetic acid; FrpB, Ferric-repressed protein B; FetA, Ferric enterobactin transport protein A; HBSS, Hank's balanced salt solution; HPI, hexagonally packed intermediate; IPTG, isopropyl-b-D-thiogalactopyranoside; MH, Mueller Hinton; OD, optical density; OMP, outer membrane protein; OMV, outer membrane vesicle; PMSF, phenylmethylsulfonyl fluoride; RT, room temperature; SB-12, n-dodecyl-N,N-dimethyl-1-ammonio-3-propanesulfonate; STEM, scanning transmission electron microscopy; TEM, transmission electron microscopy; TSB, tryptic soy broth.

[1]Department of Molecular Microbiology, Institute of Biomembranes, Utrecht University, Padualaan 8, 3584 CH Utrecht, The Netherlands

[2]M.E.Müller Institute, Biozentrum, University of Basel, Klingelbergstrasse 50/70, CH-4056 Basel, Switzerland

[3]GlaxoSmithKline Biologicals, 89 Rue de l'Institut, B-1330 Rixensart, Belgium

[4]Department of Crystal and Structural Chemistry, Bijvoet Center for Biomolecular Research, Utrecht University, Padualaan 8, 3584 CH Utrecht, The Netherlands

6.2 Introduction

Neisseria meningitidis (meningococcus) is a Gram-negative bacterium that is capable of causing life-threatening septicaemia and meningitis. Effective vaccines based on the capsular polysaccharides of the majority of pathogenic serogroups have been developed (Mitka, 2005). However, a vaccine against serogroup B meningococci, which is responsible for most disease cases in North America and Europe, is not available. Development of a polysaccharide-based vaccine against serogroup B meningococci is a cumbersome task, since the type B capsule resembles human self-antigens (Finne et al., 1983). Therefore, vaccine development against this serogroup predominantly focuses on using outer membrane proteins (OMPs) as vaccine components.

Due to its abundance and its capacity to induce bactericidal antibodies, the general diffusion porin PorA is the most extensively studied OMP with regard to its vaccine potential. PorA induces high levels of bactericidal antibodies, which is believed to be the best correlate for protection against serogroup-B meningococci (van der Voort et al., 1996). Unfortunately, however, the PorA protein shows extensive antigenic variation among strains, which complicates the development of a broad-spectrum vaccine. In the search for antigenically more conserved OMPs, proteins involved in iron acquisition are under investigation.

The meningococcus is remarkably efficient in scavenging iron from its host by using a wide variety of OMP receptors, the expression of which is regulated by the availability of iron. Together, these receptors enable the meningococcus to use various human iron-loaded proteins, such as lactoferrin, transferrin and haemoglobin (Perkins-Balding et al., 2004). Furthermore, although the meningococcus does not appear to produce its own siderophores, it has the ability to use siderophores secreted by other bacteria (Rutz et al., 1991).

The major iron-limitation-induced OMP of *N. meningitidis* is a ~70-kDa protein designated FrpB (Ferric-repressed protein B) (Petterson et al., 1995). The FrpB protein of *Neisseria gonorrhoeae* was shown to be involved in the transport of enterobactin, a siderophore produced by *Escherichia coli*, and it was, therefore, renamed FetA (Ferric enterobactin transport protein A). Enterobactin transport by FrpB is specific and dependent on the energy-coupling protein TonB (Carson et al., 1999). However, as the affinity of FrpB for enterobactin is relatively low, the possibility exists that another, enterobactin-related siderophore is the actual ligand of this protein *in vivo*.

FrpB is considered a promising vaccine candidate to protect against meningococcal disease. Although FrpB, like PorA, shows significant antigenic variation among strains (Thompson et al., 2003), its ability to induce relatively high levels of bactericidal antibodies justifies a further analysis of this protein (Ala'Aldeen et al., 1994; Petterson et al., 1990). Here, we describe the production of large quantities of FrpB, which were used for structural and immunological analysis. It was suggested recently that a vaccine comprising five FrpB (FetA) variants and six variants of PorA should afford protection against a large panel of hyperinvasive meningococcal isolates (Urwin et al., 2004). Together with our previously developed method to obtain large amounts of correctly folded PorA (Jansen, Kuipers et al., 2000; Jansen, Wiese et al., 2000), the current work enables the development of such a multivalent meningococcal subunit vaccine.

6.3 Results

6.3.1 Expression and purification of FrpB

The *frpB* gene without the signal-sequence-encoding region was cloned behind the T7 promoter on pET11a, and the construct was introduced into *E. coli* strain BL21(DE3), which contains the gene for T7 polymerase under an IPTG-inducible promoter. Upon induction, expression of the recombinant *frpB* gene resulted in large amounts of FrpB (Figure 6.1A, lane 2). The majority of FrpB was present in inclusion bodies, which were isolated and solubilized in a chaotropic agent. The protein yield was estimated as 500 mg/l of bacterial culture. SDS-PAGE analysis demonstrated the high purity of the solubilized protein (Figure 6.1A, lane 3), rendering additional purification steps unnecessary. Although FrpB has a calculated M_r of 77348 based on its amino acid sequence, the protein migrated as a 70000-M_r protein.

6.3.2 In vitro folding of FrpB

Correctly folded β-barrel OMPs exhibit deviant electrophoretic mobility on semi-native SDS-PAGE. Due to their compact conformation the folded monomeric proteins usually migrate faster on gels

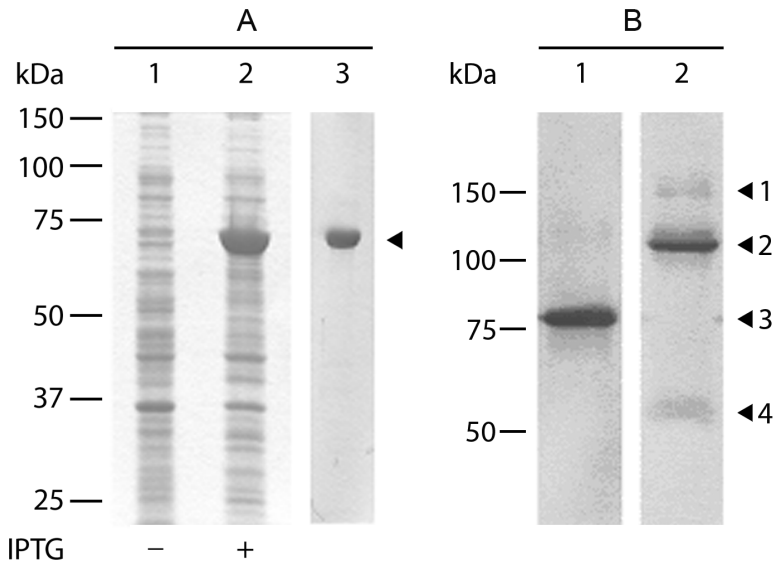

Figure 6.1: **Expression, purification and in vitro folding of recombinant FrpB.** (A) Whole cell lysates of *E. coli* BL21(DE3) containing pET11a-*frpB* before (lane 1) and after (lane 2) induction with 1 mM IPTG. Lane 3 shows FrpB (arrowhead) after isolation of the inclusion bodies and solubilization in 8 M urea. Samples were incubated at 100 °C in loading buffer containing 2 % SDS prior to electrophoresis. (B) *In vitro* folded FrpB was heat denatured by boiling for 2 min in loading buffer containing 2 % SDS (lane 1) or incubated at RT in loading buffer containing 0.075 % SDS (lane 2) and analysed by semi-native SDS-PAGE. The positions of different heat modifiable forms (arrowheads 1, 2 and 4) and the denatured form (arrowhead 3) of FrpB are indicated. The positions of the molecular-weight standard proteins are indicated on the left of both panels.

than the heat-denatured form, whereas oligomers migrate slower (Jansen, Wiese et al., 2000). This so-called heat modifiability of OMPs can be used to monitor their folding *in vitro* (Dekker et al., 1995; Jansen, Wiese et al., 2000).

To identify appropriate folding conditions, stock solutions of FrpB in 6 M guanidium hydrochloride were diluted in a range of buffers, containing different detergents and salts and having various pHs, to a series of final protein and denaturant concentrations. Initially, analysis of FrpB using routine semi-native SDS-PAGE did not reveal any differences in electrophoretic mobility. However, since native FrpB from cell envelopes appeared to be rather sensitive to SDS (data not shown), the amount of SDS normally applied in semi-native SDS-PAGE was lowered. Eventually, folded forms of FrpB were visualized and optimal folding conditions could be determined.

After dilution of guanidium hydrochloride-solubilized FrpB in 27 mM ethanolamine (pH 10.8), 0.5 % (w/v) SB-12, semi-native SDS-PAGE revealed a major band migrating with an M_r of 110000 (Figure 6.1B, lane 2). Furthermore, two minor bands with M_rs of 155000 and 55000 were detected. The 55000-M_r band probably corresponds to a folded monomeric form of FrpB, and the 110000-M_r band to a dimer of two folded monomers, whereas the 155000-M_r band suggests that some trimers might also be present. Although *in vitro* folding was always very efficient, the ratio of these folded forms varied between experiments. Only a single band, representing the unfolded protein, was detected after heat treatment (Figure 6.1B, lane 1). Strikingly, the unfolded protein migrated slower on semi-native SDS-PAGE gels than on normal SDS-PAGE gels (Figure 6.1A, lane 3). This discrepancy is most likely the result of the limiting amounts of SDS present in the electrode buffer during semi-native SDS-PAGE, since analysis of the same samples by regular SDS-PAGE revealed the expected 70000-M_r band (data not shown).

6.3.3 Semi-native 2D electrophoresis

The detection of both monomers and oligomers of FrpB in semi-native SDS-PAGE suggested that these forms might be in equilibrium. This possibility was tested by semi-native 2-D SDS-PAGE, in which the electrophoretic conditions applied were identical in both directions. In these experiments, folded monomers detected after migration in the first dimension revealed oligomers after migration in the second dimension and vice versa, consistent with an equilibrium state (Figure 6.2).

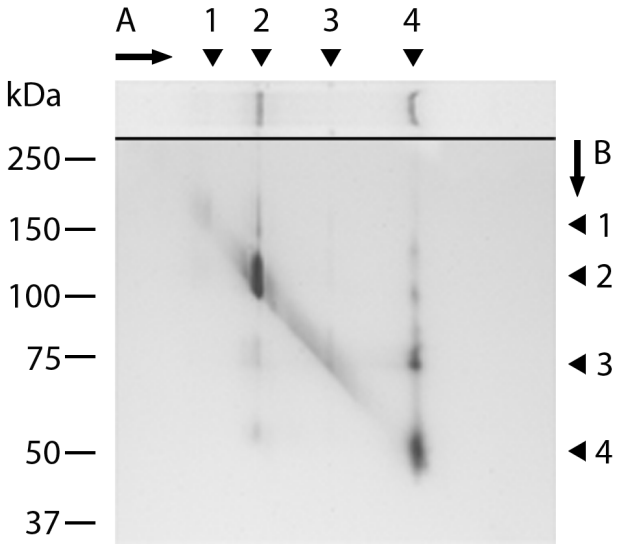

Figure 6.2: **Semi-native 2-D SDS-PAGE analysis.** *In vitro* folded FrpB was analysed in the first (arrow A) and the second (arrow B) dimension by semi-native SDS-PAGE. The positions of different heat-modifiable forms (arrowheads 1, 2 and 4) and the denatured form (arrowhead 3) of FrpB are indicated. Proteins were visualized by Coomassie staining (first dimension) or silver staining (second dimension). The positions of the molecular-weight standard proteins are indicated on the left.

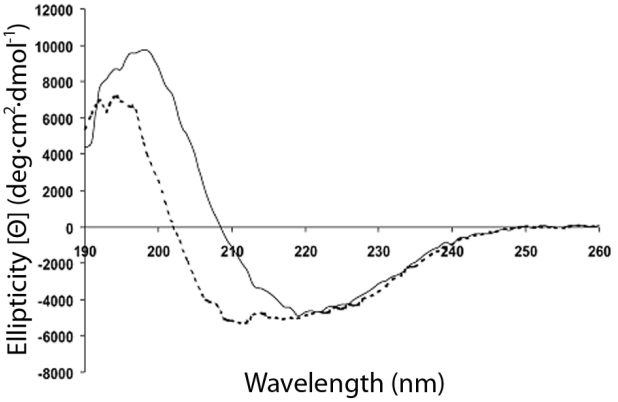

Figure 6.3: **CD spectra of in vitro folded FrpB (solid line) and FrpB denatured by boiling in 0.1 % SDS (dotted line).**

6.3.4 CD analysis

In their native conformation, OMPs are barrels with a high β-sheet content. The secondary structure of *in vitro* folded FrpB was evaluated by CD measurements. The CD spectrum had a minimum at 217 nm, consistent with the presence of β-sheet secondary structure (Figure 6.3, solid line). The spectrum of a sample that had been denatured by boiling in the presence of 0.1 % (w/v) SDS (Figure 6.3, dotted line) showed much more α-helical content, consistent with results reported for other SDS-denatured OMPs (e.g. ref. 15).

6.3.5 Trypsin digestion

Trypsin-digestion experiments were performed to confirm that FrpB was folded in a native-like conformation. Folded proteins are usually more resistant to proteases than the unfolded protein or folding intermediates. Denatured FrpB was completely degraded with 10 μg/ml trypsin (Figure 6.4A). In contrast, when folded FrpB was treated with the same amount of trypsin, two distinct tryptic fragments were detected one of which migrated slightly faster than the untreated protein (Figure 6.4B, T1). N-terminal sequencing of this fragment revealed the amino acid sequence VVLDT, indicating that trypsin cleaved the protein after Lys-6. N-terminal sequencing of the second tryptic fragment, with an M_r of 50000 (Figure 6.4B, T2), revealed the amino acid sequence INIDR, which resulted from cleavage after Arg-249. According to a proposed topology model of FrpB (unpublished), both of these trypsin-sensitive sites correspond to exposed regions in the native structure, i.e. the periplasm-exposed N terminus and the cell-surface-exposed loop L3, respectively. Strikingly, the large tryptic fragment T1, was unaffected when the trypsin concentration was increased to 100 μg/ml, whereas the 50000-M_r fragment was no longer detected (Figure 6.4B, lane 3). Apparently, a proportion of the *in vitro* folded protein is susceptible to trypsin cleavage in loop L3 and, subsequently, to further degradation, whereas the other proportion is not. This finding suggests that at least two structurally distinct forms of FrpB were formed during the *in vitro* folding procedure. Besides T1 and T2, two additional tryptic fragments of FrpB were detected on Western blots (T3 and T4, Figure 6.4C, lane 1). Similar fragments obtained after digestion of *in vitro* folded FrpB were also obtained upon trypsin treatment of cell envelopes (Figure 6.4C, lane 2). These results confirm that FrpB adopted a native-like structure upon *in vitro* folding.

6.3.6 Electron microscopic evaluation of the FrpB conformation

To study the conformation of *in vitro* folded FrpB in further detail, the protein was diluted 50 x, adsorbed to thin carbon films and imaged by STEM for mass measurement (see Materials and methods). In spite of this large dilution some particles

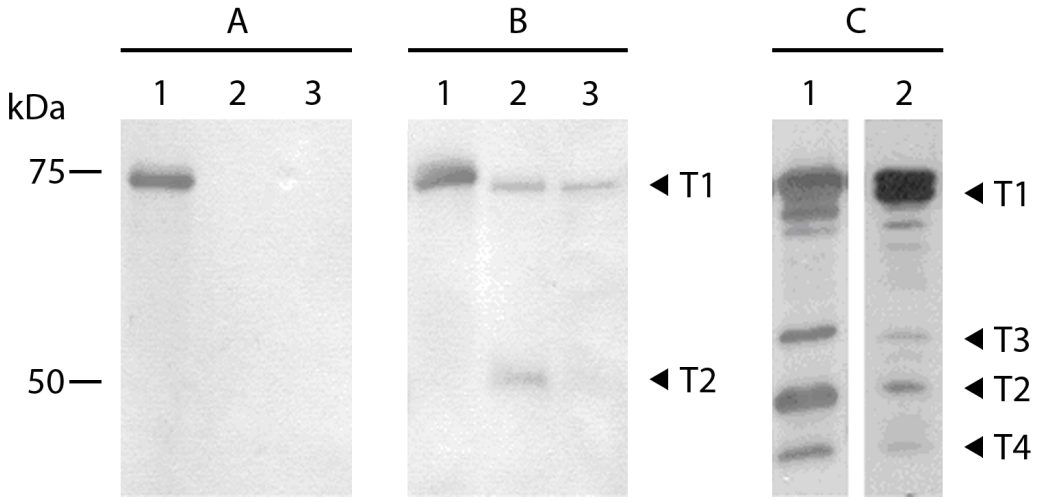

Figure 6.4: **Trypsin digestion of FrpB.** (A) denatured and (B) *in vitro* folded FrpB were treated with 0 (lane 1), 10 (lane 2) or 100 (lane 3) μg/ml trypsin and the tryptic fragments were separated by SDS-PAGE and stained with Coomassie brilliant blue. T1 and T2 indicate the major tryptic fragments of FrpB. (C) Tryptic fragments of FrpB present after incubation of *in vitro* folded FrpB with 10 μg/ml trypsin (lane 1) and cell envelopes with 10 mg/ml trypsin (lane 2) were detected on Western blots. Arrowheads indicate tryptic fragments. The positions of the molecular-weight standard proteins are indicated on the left.

were still too close to neighbours prohibiting evaluation. Nevertheless, over 3800 projections were selected from the images, sorted according to their dimensions into a main class and a minor class, and analysed. The mass histogram from the main class (n = 3326) displayed a single major peak with a distinct high-mass sidearm (Figure 6.5A). Over 86 % of the particles had a mass of 149000 $\pm$ 53000 (n$\sim$2894). The siderophore receptor FhuA of *E. coli*, which may have a similar structure to FrpB, is reported to associate with 185 molecules of the detergent dodecyl maltoside (Boulanger et al., 1996). Assuming that a similar number of detergent molecules associates with FrpB (mass predicted from the sequence 77348 Da), the contribution of SB-12 (monomer mass 335.5 Da) would be around 62000 Da, resulting in a theoretical total mass of 139348 Da for the FrpB-detergent complex. Thus, the mass calculated from the images strongly implies the presence of a large population of FrpB monomers. The high-mass asymmetry of the histogram (Figure 6.5A) reflects the presence of FrpB dimers (n$\sim$433), as confirmed by the Gaussian fitted to this region that falls at a mass of 263000 $\pm$ 53000. The calculated mass indicates that there is less detergent associated per monomer in the dimer, which can be explained by the absence of detergent at the site where the two monomers are in contact. The minor second class of particles (n = 505) was comprised of particles that were visibly larger than those in the main class and had masses in the range of dimers and above (data not shown). Accordingly, all together, 75 % of all the particles selected were monomers.

An overview of the FrpB sample after negative staining with 2 % uranyl acetate is shown in Figure 6.5B; various orientations of the protein can be distinguished. A total of 1791 projections were automatically selected from the images and manually refined; projections too close to neighbours or clearly arising from larger particles were removed. The remaining 880 projections were then subjected to reference-free alignment and classification. Figure 6.5C shows class averages of tilted top-views and side-views of the FrpB monomer. The side-view averages have diameters of $\sim$6 nm and $\sim$8 nm, which is in the range expected from the crystal structures of the *E. coli* siderophore receptors FepA (Buchanan et al., 1999) and FhuA (Ferguson et al., 1998). Some of the tilted top-view projections show signs of a pore (Figure 6.5C).

6.3.7 Immune response against in vitro folded FrpB

Mice were immunized to evaluate whether antibodies can be raised against *in vitro* folded FrpB that recognize FrpB expressed *in vivo* at the bacterial cell surface. The sera obtained 7 days after the third injection were pooled and evaluated in ELISAs using *in vitro* folded FrpB as the coating antigen. The mean mid-point titre of 4837 in-

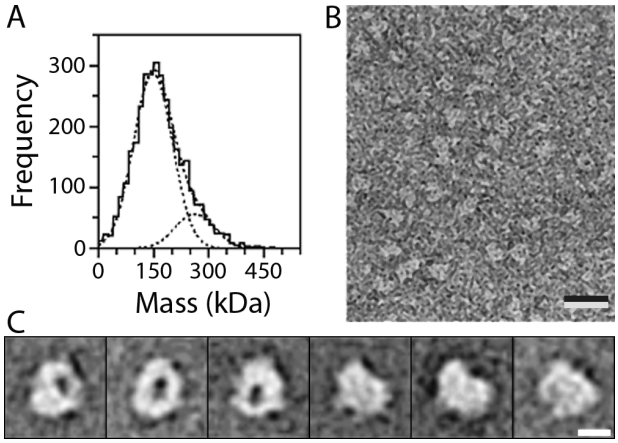

Figure 6.5: **Analysis of in vitro folded FrpB by electron microscopy.** (A) STEM mass analysis of detergent solubilized, *in vitro* folded FrpB. The histogram of mass values can be described by two Gaussian curves falling at 149000 ± 53000 Da (n∼2894; standard error, SE = ± 1000; overall uncertainty ± 8000, considering the SE and the 5 % calibration uncertainty of the instrument) and 263000 ± 53000 Da (n∼433; SE = ± 3000; overall uncertainty ± 13000) respectively. (B) Overview image of the FrpB sample recorded by TEM after negative staining with 2 % uranyl acetate. (C) Average projections showing tilted top-views (first three panels) and various side-views of the negatively stained, detergent solubilized FrpB monomer. The top-views indicate a stain-filled cavity implying the presence of a pore. The scale bar is 20 nm in (B) and 5 nm in (C).

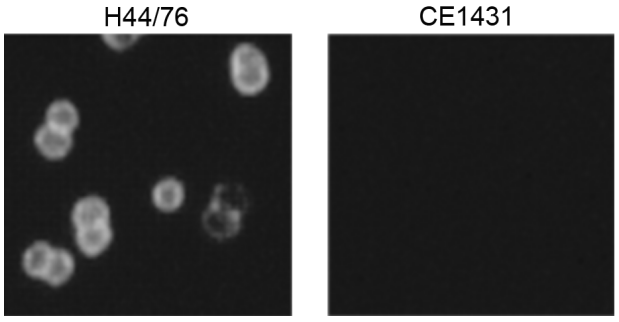

Figure 6.6: **Immunofluorescence microscopy.** Immunofluorescence micrographs of *N. meningitidis* strain H44/76 and its *frpB* mutant derivative CE1431 with antiserum raised against *in vitro* folded FrpB.

dicated good responses. Immunofluorescence microscopy was used to determine whether the antibodies recognized FrpB on the cell surface of living meningococci. These experiments showed that wild-type meningococci grown under iron-limitation were labelled, whereas an *frpB* mutant was not (Figure 6.6). The bactericidal activity of the antibodies was also evaluated. The assays showed that the serum was bactericidal against strain H44/76 (50 % killing at a serum dilution of 1:912). The bactericidal response was specific for FrpB, since the *frpB* mutant was not killed. Hence, these results show that native epitopes are present after folding FrpB *in vitro* and that bactericidal antibodies can be raised with the *in vitro* folded protein.

6.4 Discussion

FrpB of *N. meningitidis* is considered an important vaccine candidate. Here, we have developed a procedure to obtain large quantities of FrpB in its native conformation for both immunological and structural analysis. Semi-native SDS-PAGE indicated that the predominant form of *in vitro* folded FrpB is a dimer, which is in equilibrium with folded monomers and, possibly, higher oligomeric forms. In agreement with this observation, SDS-PAGE analysis of FrpB from meningococcal cell envelopes has shown that the protein is present in an oligomeric, probably dimeric, complex in the outer membrane (Prinz and Tommassen, 2000). Accurate comparison of the oligomeric structure of FrpB from meningococcal outer membranes and *in vitro* folded FrpB is however difficult, since *in vivo* the complex interacts with the RmpM protein, which remains associated to FrpB during semi-native SDS-PAGE (Prinz and Tommassen, 2000). Although oligomers of FrpB were also detected by analysis of cell envelopes from an *rmpM* mutant (Prinz and Tommassen, 2000), the fuzziness of these bands prohibited the accurate determination of the M_r. Furthermore, these oligomers might contain associated lipopolysaccharide, which has been shown to increase the observed M_r of OMPs (Bos et al.; Jansen, Heutink et al., 2000).

Support for the assumption that FrpB folded to a native-like structure, was obtained in trypsin sensitivity assays. Four tryptic fragments were detected on Western blots that migrated at the same position as the bands obtained upon digestion of native FrpB in cell envelopes. Two of the four bands were present in sufficient amounts for N-terminal sequencing. One fragment resulted from cleavage after Lys-6 near the N terminus, the other from cleavage after Arg-249, which is located in a predicted surface-exposed loop (unpublished). Lys-6 is located close to the TonB box, which supposedly interacts with the energy-coupling protein TonB. Interestingly, the *E. coli* siderophore receptor FhuA is cleaved by trypsin at Lys-5, which is also in close proximity to the TonB box (Moeck et al., 1996). As it is conceivable that both trypsin-sensitive sites

of *in vitro* folded FrpB are exposed in the native structure, these results strongly indicate that the protein folded correctly during the *in vitro* folding procedure. Strikingly, treatment of FrpB with an increased amount of trypsin only yielded the fragment resulting from cleavage at Lys-6. This result indicates that at least two structurally different FrpB molecules coexist. Since FrpB is also present as a dimer in the preparations, it is tempting to speculate that this dimer is asymmetric.

Although mass analysis by STEM revealed the presence of dimers, it indicated that most of the FrpB protein analysed was monomeric (Figure 6.5A). Thus, the monomer/dimer ratios observed from semi-native SDS-PAGE and STEM do not fully correspond. This is understandable because not every particle imaged by STEM could be measured (see Results). Further, the dilution required may have shifted the monomer-dimer equilibrium towards the monomer.

The current work demonstrates the ability of FrpB to assemble into homo-oligomeric dimers. Interestingly, the crystal structures of other TonB-dependent receptors, such as FhuA (Ferguson et al., 1998; Locher et al., 1998) and FepA (Buchanan et al., 1999), revealed monomeric proteins. Analytical ultracentrifugation also indicated that purified FhuA is monomeric (Locher and Rosenbusch, 1997). However, in the latter study oligomers of FhuA were detected by analytical ultracentrifugation after cross-linking, and a positive co-operativity was observed in siderophore-binding experiments, which is also consistent with an oligomeric state of the receptor. Furthermore, FhuA dimers have been visualized in 2D crystals by electron microscopy (Lambert et al., 1999). It is therefore tempting to speculate that the TonB-dependent receptors in general form dimers, which, however, readily dissociate into monomers when extracted from the membrane with detergents.

The dimensions of FrpB observed by TEM correspond to those expected from the crystal structures of FhuA (Ferguson et al., 1998; Locher et al., 1998) and FepA (Buchanan et al, 1999). Some of the projections showed signs of a pore. These projections probably represent FrpB molecules in the up orientation, since the periplasmic side of the β-barrels of the TonB-dependent receptors is closed by a plug formed by an N-terminal domain of these proteins. Since milligram quantities of folded FrpB can now readily be obtained, future experiments will focus on elucidating its three-dimensional structure.

The *in vitro* folded FrpB protein was capable of inducing high levels of antibodies that recognized FrpB in the outer membrane and were bactericidal, showing that native epitopes are formed during the *in vitro* folding procedure. It was recently reported that a vaccine based on six PorA and five FrpB (FetA) variants should be able to provide protection against a large panel of hyperinvasive meningococcal isolates (Urwin et al., 2004). The current work, together with previously developed methods to fold the PorA protein *in vitro* (Jansen, Kuipers et al., 2000; Jansen, Wiese et al., 2000), thus enables the development of a protein-based meningococcal subunit vaccine.

6.5 Experimental procedures

6.5.1 Expression and isolation of FrpB

The part of *frpB* encoding the mature protein (*i.e.*, FrpB without its signal sequence) was PCR amplified from genomic DNA of *N. meningitidis* strain H44/76 with the primer pair 5'-GCTACATATGGCAGAAAATAATCGGAAGGTC-3' and 5'-GCTAGGATCCTTAGAACTTGTAGTTCACGCC-3' containing *Nde*I and *Bam*HI restriction sites, respectively (underlined). The resulting product was cloned into pCRII-TOPO according to the instructions of the manufacturer (Invitrogen). From there, the *frpB* fragment was obtained by digestion with *Nde*I and *Bam*HI and cloned downstream of the inducible T7 promoter of plasmid pET11a (Novagen), which was digested with the same restriction enzymes. This resulted in the plasmid pET11a-*frpB*. *E. coli* strain BL21(DE3) (Studier and Moffatt, 1986), which contains the gene for T7 RNA polymerase under an isopropyl-β-D-thiogalactopyranoside (IPTG)-inducible promoter, was transformed with the plasmid. An overnight culture of the resulting strain was diluted 1:50 into fresh Luria-Bertani (LB) medium supplemented with 100 μg/ml ampicillin for plasmid maintenance. When an optical density at 550 nm (OD_{550}) of 0.6 was reached, protein expression was induced by the addition of 1 mM IPTG (Sigma). After 2.5 h of growth, the bacteria were harvested by centrifugation and washed with 0.9% (w/v) NaCl. Cell pellets were stored at -20°C. FrpB was present in inclusion bodies, which were isolated as described (Dekker et al., 1995).

6.5.2 In vitro folding of FrpB

Inclusion bodies were solubilized in 20 mM Tris-HCl, 100 mM glycine (pH 8.0) containing either 6 M guanidium hydrochloride or 8 M urea. After incubation on a turning wheel for 1.5 h, residual membrane fragments were removed by centrifugation for 1 h at 356000g. The protein concentration in the supernatant was determined with the Pierce protein assay (Pierce, Rockford, Illinois, USA) using BSA (Sigma) as a standard. *In vitro* folding of FrpB was initiated by 20-fold dilution of fresh solubilized inclusion bodies (50 mg/ml) in 27 mM ethanolamine (pH 10.8) containing 0.5% (w/v) n-dodecyl-N,N-dimethyl-1-ammonio-3-propanesulfonate (SB-12) (Fluka, Buchs, Switzerland). Prior to use, the detergent was dissolved in methanol/chloroform (1:1) and purified by passage over an Al_2O_3 column (Dekker et al., 1995). All *in vitro* folding experiments with FrpB were initiated at room temperature (RT), and the protein was stored at 4°C until analysis. For analysis of trypsin sensitivity, CD spectroscopy, electron microscopy, analytical ultracentrifugation and immunization experiments, the buffer was exchanged using a PD-10 desalting column (Amersham). After exchange, some aggregates were observed, which were removed by filtration through a filter with a pore size of 0.22 μm (Millipore). When required, detergent was exchanged by n-octyl-oligo-oxyethylene (octyl-POE) (Alexis biochemicals) by passage through Centricon YM-100 filters (Amicon).

6.5.3 SDS-PAGE and Western blotting

Proteins were separated by standard sodium dodecyl sulfate-polyacrylamide gel electrophoresis (SDS-PAGE). To detect folded forms of FrpB, an SDS-PAGE system that we refer to as semi-native SDS-PAGE was used (Voulhoux et al., 2003). In this technique, to prevent denaturation of the folded proteins the slab gels are devoid of SDS, while the amount of SDS present in the electrode buffer and loading buffer depend on the SDS-sensitivity of the protein of interest and is empirically determined for each protein. For FrpB, the electrode and loading buffers contained 0.01% and 0.075% (w/v) SDS (end concentration), respectively. The samples were kept at RT before loading. To denature the protein, a loading buffer with 2% (w/v) SDS (end concentration) was used, and these samples were boiled for 2 min before loading. The samples were loaded on polyacrylamide gels composed of a stacking gel with 3% (w/v) acrylamide and a 7% (w/v) resolving gel. Electrophoresis was performed on ice at a constant current of 10 mA. After electrophoresis, proteins were visualized by Coomassie brilliant blue staining.

For two-dimensional (2D) semi-native SDS-PAGE, a lane was cut from a gel run in the first dimension. This gel-slice was then rotated 90° and placed on top of a new polyacrylamide gel. Electrophoresis in the second dimension was performed under the same conditions as the first dimension, after which protein spots were visualized by silver staining (Blum et. al, 1987).

Western blotting was performed as described (van Ulsen et al., 2003), using a polyclonal antiserum raised against *in vitro* folded FrpB and peroxidase-conjugated goat anti-mouse IgG (Southern Biotechnology Associates Inc.) as secondary antibody.

6.5.4 CD spectroscopy

CD spectra of FrpB in 5 mM phosphate buffer [0.775 mM NaH_2PO_4, 4.225 mM Na_2HPO_4 (pH 7.6)] containing 0.3% (w/v) SB-12 were recorded at RT over a wavelength range of 190-260 nm using a 0.5 mm path cell in an Olis CD instrument (Olis, Inc. USA). The monochromator was equipped with a fixed disk and gratings were used with 2400 lines/mm (blaze wavelength 230 nm). The FrpB concentration used for CD measurements was 0.586 mg/ml (A_{280}). The CD spectra shown are the average of ten repeated scans (step resolution 1 nm) from which the corresponding buffer spectrum was subtracted. The measured CD signals were converted to molar ellipticity (θ). For the comparison between folded and denatured protein, a sample, that had been boiled for 3 min in the presence of 0.1% SDS (w/v), was also analyzed.

6.5.5 Isolation of cell envelopes

N. meningitidis strain CE2001 (Tommassen et al., 1990) was grown in TSB supplemented with 20 mg/ml of the iron chelator ethylenediamine di-*o*-hydroxyphenylacetic acid (EDDHA; Sigma). Bacteria were collected by centrifugation, resuspended in 50 mM Tris-HCl, 5 mM EDTA (pH 8.0) containing the protease inhibitor cocktail "Com-

plete" (Roche) and stored overnight at -80°C. After ultrasonic disintegration, unbroken cells were removed by centrifugation (12000g, 15 min) and cell envelopes were collected by ultracentrifugation (170000g, 5 min). The resulting pellet was dissolved in 2 mM Tris-HCl (pH 7.6) and stored at -80°C.

6.5.6 Trypsin digestion

A sample of *in vitro* folded FrpB [0.5 mg/ml in 50 mM HEPES (pH 7.5), 0.3% (w/v) SB-12] was divided between two vials. One sample was denatured by boiling in 0.1% (w/v) SDS for 5 min, the other was left untreated. Both samples were subsequently treated with trypsin (Sigma) for 15 min at RT, after which 1 mM phenylmethylsulfonyl fluoride (PMSF; Sigma) was added and the samples were analyzed by SDS-PAGE. For N-terminal sequencing, the tryptic fragments were blotted from the gels onto polyvinylidene difluoride membranes (Millipore). The blots were stained with Coomassie blue G-250, and appropriate bands were excised. Samples were subjected to 5 steps of Edman degradation at the Protein Sequencing Facility, Utrecht University.
Trypsin sensitivity of FrpB present in cell envelopes was assessed by incubating cell envelopes with 10 mg/ml trypsin for 30 min at RT. Afterwards 1 mM PMSF was added and the samples were analyzed by SDS-PAGE, followed by Western blotting.

6.5.7 Scanning transmission electron microscopy (STEM)

The FrpB sample [10 μg/ml in phosphate buffer (pH 7.6), 0.3% (w/v) SB-12] was diluted 50x with buffer containing detergent. Immediately afterwards, 5 μl aliquots were adsorbed for 60 s to glow-discharged STEM films (thin carbon films that span a thick fenestrated carbon layer covering 200 mesh/inch, gold-plated copper grids). The grids were then blotted, washed on 7 drops of quartz double-distilled water, and freeze-dried at -80°C and $5{\cdot}10^{-8}$ Torr overnight in the microscope. The hexagonally packed intermediate (HPI) surface layer of the archaebacterium *Deinoccus radiodurans* (kindly supplied by Dr. Harald Engelhardt, Max-Planck-Institute for Biochemistry, Martinsried, Germany) served as mass standard. This sample was similarly adsorbed to separate microscopy grids, washed on 4 droplets of quartz double-distilled water, and air-dried.
A Vacuum Generators STEM HB-5 interfaced to a modular computer system (Tietz Video and Image Processing Systems GmbH, Gauting, Germany) was employed. Series of 512 by 512 pixel, dark-field images were recorded from the unstained samples at an accelerating voltage of 80 kV and a nominal magnification of 200kx. The recording dose was ranged from 448 to 855 electrons/nm^2. Further, repetitive low dose scans were made of some grid regions to assess beam-induced mass-loss as outlined in (Müller et al., 1992). The digital images were evaluated using the program package IMPSYS (Müller et al., 1992). Accordingly, the projections were selected in circular boxes, and the total scattering of each region was calculated. The background scattering of the carbon support film was then subtracted and the mass was calculated. The results were scaled according to the mass measured for HPI and corrected for the beam-induced mass-loss, which varied between 8.1% and 15.4% depending on the dose employed. The mass values were then displayed in histograms and described by Gauss curves.

6.5.8 Transmission electron microscopy (TEM)

For TEM analysis, 5 μl aliquots of FrpB [20 μg/ml in phosphate buffer (pH 7.6), 0.3% (w/v) SB-12] were adsorbed for 60 s to a glow-discharged, carbon-coated TEM microscopy grid. The grid was then blotted, washed on 7 droplets of quartz double-distilled water and negatively stained on 2 droplets of 2% (w/v) uranyl acetate (pH 4.5). Bright-field images were recorded on photographic film using a Hitachi 7000 electron microscope at an accelerating voltage of 100 kV and a magnification of 80kx. A Leafscan scanner was employed to digitize two of the negatives at a sampling step size of 0.5 nm/pixel, yielding 24 subimages (512 by 512 pixels). Projections (centered in 32 by 32 pixel regions) were automatically selected from these by cross-correlation with a centered, 20-fold symmetrized circular reference, using the SEMPER image-processing package (Synoptics Ltd., Cambridge, England). Reference-free alignment and classification of the selected particles were done with the SPIDER image processing software (Frank et al., 1996).

6.5.9 Immunization of mice

A group of 10 OF-1 mice (Charles River, Lyon, female, 6-8 weeks of age) received three injections with *in vitro* folded FrpB by intramuscular route on day 0, 21 and 28. With each injection, 5 μg of antigen formulated in $AlPO_4$ plus monophosphoryl lipid A was administered. Blood samples were collected 14 days after the third injection and pooled.

6.5.10 ELISA

ELISA plates were coated with 100 μl of folded FrpB (5 μg/ml) in PBS. After overnight incubation at 4°C, the plates were washed three times with 150 mM NaCl, 0.05% (v/v) Tween-20. Non-specific protein-binding sites were blocked with 200 μl PBS, 1% (w/v) BSA for 30 min at RT under agitation. After washing with 150 mM NaCl, 0.05% (v/v) Tween-20, serum was added to the wells and serially diluted (two-fold dilution steps) in PBS, 0.2% (w/v) BSA, 0.05% (v/v) Tween-20. After 30 min, the plates were washed and subsequently incubated first with goat anti-mouse IgG antibodies conjugated to biotin (Prosan, 1:2000) and then with streptavidine-peroxidase (Amersham, 1:3000) in the same buffer. Incubations were performed for 30 min at 37°C under shaking. Plates were washed and incubated in the dark with 0.1 M citrate buffer (pH 4.5), 0.4% (w/v) *o*-phenylenediamine (Sigma), 2 mM H_2O_2. The reaction was stopped by the addition of 1 M HCl and the absorbance was read at 490 nm.

6.5.11 Serum bactericidal assay

N. meningitidis strain H44/76 and its *frpB* mutant derivative CE1431 (Petterson et al., 1995) were grown overnight on Mueller Hinton (MH) agar (Difco), 1% (v/v) Polyvitex (Biomérieux), 1% (v/v) horse serum (Sigma) at 37°C in a 5% CO_2 atmosphere. The bacteria were inoculated in tryptic soy broth (TSB) (Beckton Dickinson) with 50 μM of the iron chelator desferrioxamine mesylate (Sigma) and grown in shaking flasks for 3 h at 37°C until an OD_{470} of 0.5 was reached. The complement in pooled serum was heat inactivated for 40 min at 56°C. The serum was subsequently diluted 1:100 in Hank's balanced salt solution (HBSS, Gibco), 0.3% (w/v) BSA and then serially diluted (two-fold dilution steps, eight dilutions) in a volume of 50 μl in round-bottom microtiter plates. Bacteria were diluted in HBSS, 0.3% (w/v) BSA to yield 13000 colony- forming units (CFU) per ml. Afterwards, 37.5 μl aliquots of this dilution were added to the serum dilutions and the microtiter plates were incubated for 15 min at 37°C under shaking. Subsequently, 12.5 μl of baby-rabbit complement (Pelfreez) or, as a control for toxicity of the sera, heat-inactivated complement (56°C for 45 min) was added to the wells. After 1 h of incubation at 37°C under shaking, the microtiter plates were placed on ice to stop killing. A 20 μl aliquot was removed from each well and spotted on MH agar plates containing 1% (v/v) Polyvitex, 1% (v/v) horse serum. Plates were tilted to allow the drop to "run" down the plate. After overnight incubation at 37°C in a 5% CO_2 atmosphere, the CFUs were counted, and the percentage of killing was calculated.

6.5.12 Immunofluorescence microscopy

Bacteria were grown in candle jars at 37°C in a humid atmosphere on GC (Oxoid) plates supplemented with Vitox (Oxoid) and with 20 μg/ml EDDHA to impose iron limitation. The next day, the bacteria were suspended in HBSS, 0.5% (w/v) BSA (washing buffer) to an OD_{550} of 1. Bacteria from 300 μl of this suspension were collected by centrifugation and resuspended in 300 μl washing buffer containing serum (1:100). After incubation for 1 h and washing twice, the bacteria were resuspended in 300 μl of washing buffer containing the secondary antibody goat anti-mouse IgG conjugated with Alexa-green (Molecular Probes, Oregon, USA) (1:400). After incubation for 1 h and washing, the bacteria were collected and resuspended in 300 μl HBSS containing 2% (v/v) formaldehyde, immobilized on polylysine-coated coverslips and analyzed by microscopy.

6.6 Acknowledgements

We thank Remco Nagel and Suzanne Hermeling for assistance in the trypsin sensitivity assays and CD analysis, respectively. Furthermore, we thank Mark Doeven and Bert Poolman (Department of Biochemistry, University of Groningen), Andreas Engel (Maurice E. Müller Institute, Biozentrum, University of Basel) and Karel Planken (Van 't Hoff Laboratory for Physical and Colloid Chemistry, University of Utrecht) for helpful discussions. This work was supported by the Netherlands Research Council for Chemical Sciences (CW) with financial aid from

the Netherlands Technology Foundation (STW), the European Community (grant HPRN-CT-2000-00075), the Maurice E. Müller Foundation with financial aid from the Swiss National Foundation grants NF 31-59 415.99 and SNF 501 221 and the National Center of Competence in Research Structural Biology.

6.7 References

Ala'Aldeen, D.A.A., Davies, H.A. and Borriello, S.P. (1994) Vaccine potential of meningococcal FrpB: studies on surface exposure and functional attributes of common epitopes. Vaccine, 12, 535-541.

Blum, H., Beier, H., Gross, H. J. (1987) Improved silver staining of plant proteins, RNA and DNA in polyacrylamide gels. Electrophoresis, 8, 93-99.

Bos, M.P., Tefsen, B., Geurtsen, J. and Tommassen, J. (2004) Identification of an outer membrane protein required for the transport of lipopolysaccharide to the bacterial cell surface. Proc. Natl. Acad. Sci. U S A, 101, 9417-9422.

Boulanger, P., le Maire, M., Bonhivers, M., Dubois, S., Desmadril, M. and Letellier, L. (1996) Purification and structural and functional characterization of FhuA, a transporter of the *Escherichia coli* outer membrane. Biochemistry, 35, 14216-14224.

Buchanan, S.K., Smith, B.S., Venkatramani, L., Xia, D., Esser, L., Palnitkar, M., Chakraborty, R., van der Helm, D. and Deisenhofer, J. (1999) Crystal structure of the outer membrane active transporter FepA from *Escherichia coli*. Nat. Struct. Biol., 6, 56-63.

Carson, S.D.B., Klebba, P.E., Newton, S.M.C. and Sparling, P.F. (1999) Ferric enterobactin binding and utilization by *Neisseria gonorrhoeae*. J Bacteriol, 181, 2895-2901.

Dekker, N., Merck, K., Tommassen, J. and Verheij, H.M. (1995) *In vitro* folding of *Escherichia coli* outer-membrane phospholipase A. Eur J Biochem, 232, 214-219.

Ferguson, A.D., Hofmann, E., Coulton, J.W., Diederichs, K. and Welte, W. (1998) Siderophore-mediated iron transport: crystal structure of FhuA with bound lipopolysaccharide. Science, 282, 2215-2220.

Finne, J., Leinonen, M. and Mäkela, P.H. (1983) Antigenic similarities between brain components and bacteria causing meningitis. Implications for vaccine development and pathogenesis. Lancet, 2, 355-357.

Frank, J., Radermacher, M., Penczek, P., Zhu, J., Li, Y., Ladjadj, M. and Leith, A. (1996) SPIDER and WEB: processing and visualization of images in 3D electron microscopy and related fields. J Struct Biol, 116, 190-199.

Jansen, C., Heutink, M., Tommassen, J. and de Cock, H. (2000a) The assembly pathway of outer membrane protein PhoE of *Escherichia coli*. Eur J Biochem, 267, 3792-3800.

Jansen, C., Kuipers, B., van der Biezen, J., de Cock, H., van der Ley, P. and Tommassen, J. (2000b) Immunogenicity of *in vitro* folded outer membrane protein PorA of *Neisseria meningitidis*. FEMS Immunol Med Microbiol, 27, 227-233.

Jansen, C., Wiese, A., Reubsaet, L., Dekker, N., de Cock, H., Seydel, U. and Tommassen, J. (2000c) Biochemical and biophysical characterization of *in vitro* folded outer membrane porin PorA of *Neisseria meningitidis*. Biochim Biophys Acta, 1464, 284-298.

Lambert, O., Moeck, G.S., Levy, D., Plançon, L., Letellier, L. and Rigaud, J.L. (1999) An 8-Å projected structure of FhuA, a "ligand-gated" channel of the *Escherichia coli* outer membrane. J Struct Biol, 126, 145-155.

Locher, K.P., Rees, B., Koebnik, R., Mitschler, A., Moulinier, L., Rosenbusch, J.P. and Moras, D. (1998) Transmembrane signaling across the ligand-gated FhuA receptor: crystal structures of free and ferrichrome-bound states reveal allosteric changes. Cell, 95, 771-778.

Locher, K.P. and Rosenbusch, J.P. (1997) Oligomeric states and siderophore binding of the ligand-gated FhuA protein that forms channels across *Escherichia coli* outer membranes. Eur J Biochem, 247, 770-775.

Mitka, M. (2005) New vaccine should ease meningitis fears. JAMA, 293, 1433-1434.

Moeck, G.S., Tawa, P., Xiang, H., Ismail, A.A., Turnbull, J.L. and Coulton, J.W. (1996) Ligand-induced conformational change in the ferrichrome-iron receptor of *Escherichia coli* K-12. Mol Microbiol, 22, 459-471.

Müller, S.A., Goldie, K. N., Bürki, R., Häring, R., Engel, A. (1992) Factors influencing the precision of quantitative scanning transmission electron microscopy. Ultramicroscopy, 46, 317-334.

Perkins-Balding, D., Ratliff-Griffin, M. and Stojiljkovic, I. (2004) Iron transport systems in *Neisseria meningitidis*. Microbiol Mol Biol Rev, 68, 154-171.

Pettersson, A., Kuipers, B., Pelzer, M., Verhagen, E., Tiesjema, R.H., Tommassen, J. and Poolman, J.T. (1990) Monoclonal antibodies against the 70-kilodalton iron-regulated protein of *Neisseria meningitidis* are bactericidal and strain specific. Infect Immun, 58, 3036-3041.

Pettersson, A., Maas, A., van Wassenaar, D., van der Ley, P. and Tommassen, J. (1995) Molecular characterization of FrpB, the 70-kilodalton iron-regulated outer membrane protein of *Neisseria meningitidis*. Infect Immun, 63, 4181-4184.

Prinz, T. and Tommassen, J. (2000) Association of iron-regulated outer membrane proteins of *Neisseria meningitidis* with the RmpM (class 4) protein. FEMS Microbiol

Lett, 183, 49-53.

Rutz, J.M., Abdullah, T., Singh, S.P., Kalve, V.I. and Klebba, P.E. (1991) Evolution of the ferric enterobacterin receptor in Gram-negative bacteria. J Bacteriol, 173, 5964-5974.

Studier, F.W. and Moffatt, B.A. (1986) Use of bacteriophage T7 RNA polymerase to direct selective high-level expression of cloned genes. J Mol Biol, 189, 113-130.

Thompson, E.A., Feavers, I.M. and Maiden, M.C.J. (2003) Antigenic diversity of meningococcal enterobactin receptor FetA, a vaccine component. Microbiology, 149, 1849-1858.

Tommassen, J., Vermeij, P., Struyvé, M., Benz, R. and Poolman, J.T. (1990) Isolation of *Neisseria meningitidis* mutants deficient in class 1 (porA) and class 3 (porB) outer membrane proteins. Infect Immun, 58, 1355-1359.

Urwin, R., Russell, J.E., Thompson, E.A.L., Holmes, E.C., Feavers, I.M. and Maiden, M.C.J. (2004) Distribution of surface protein variants among hyperinvasive meningococci: implications for vaccine design. Infect Immun, 72, 5955-5962.

van der Voort, E.R., van der Ley, P., van der Biezen, J., George, S., Tunnela, O., van Dijken, H., Kuipers, B. and Poolman, J. (1996) Specificity of human bactericidal antibodies against PorA P1.7,16 induced with a hexavalent meningococcal outer membrane vesicle vaccine. Infect Immun, 64, 2745-2751.

van Ulsen, P., van Alphen, L., ten Hove, J., Fransen, F., van der Ley, P. and Tommassen, J. (2003) A Neisserial autotransporter NalP modulating the processing of other autotransporters. Mol Microbiol, 50, 1017-1030.

Voulhoux, R., Bos, M.P., Geurtsen, J., Mols, M. and Tommassen, J. (2003) Role of a highly conserved bacterial protein in outer membrane protein assembly. Science, 299, 262-265.

Chapter 7

Outlook

The fields of cryo-Electron microscopy and single particle analysis are rapidly progressing. Only 15 years ago the resolution limit for volume reconstructions obtained by these techniques, was in the range of 30-40 Å, whereas today an increasing number of single particle volumes at sub-nanometer resolution has been published. This trend is likely to continue and the single particle community clearly aims at improving the reconstruction techniques towards atomic resolution. It has been estimated that in order to break the resolution limit of 4 Å, which would allow tracing of the polypeptide backbone, a landmark number of one million particles would have to be involved. To achieve this goal, many laboratories have been working intensively on automated image acquisition, particle pickup and 3D reconstruction algorithms. Considering the fast growth of computational power, it is foreseeable that atomic structures, specifically of icosahedral viruses and particularly stable proteins complexes with lower-symmetric features, will be available in the near future. A major difficulty, however, will consist in calculating very high resolution volumes of flexible proteins and fragile or inhomogeneous protein complexes. Single particle averaging assumes multiple copies of identical molecules, and in the case of inhomogeneous particle populations, classification methods would have to be applied, thus inevitably increasing the number of images required for high resolution. Nevertheless, for many multi-subunit complexes, it is possible to obtain high resolution information by docking the atomic coordinates of single protein components into medium-resolution electron density maps. This technique will become increasingly important in the face of the exponentially incrementing number of atomic structures provided by NMR spectroscopy and high-throughput crystallization methods. Until today, over 35000 structures have been deposited in the RCSB protein data bank (http://www.pdb.org, February 2006). However, to achieve the central objective of structural proteomics, namely solving the atomic structures of entire proteomes, exhaustive efforts in further development of the individual methods and their complementary application will be necessary. Experimental techniques will have to go hand in hand with comparative computational modeling, an emerging discipline with great potential to fill the gaps of structural information left open by proteins withstanding any attempt of crystallization. The question, however, will be: how many structurally diverse templates are required for reliable and accurate modeling of the remainder of the proteomes of interest?

Appendix A

Short Curriculum Vitae

Affiliation

Marco Gregorini
Maurice Müller Institute and
Division of Structural Biology
Biozentrum, University of Basel
Klingelbergstrasse 50/70
4056 Basel - Switzerland
E-mail: Marco.Gregorini@unibas.ch

Education

PhD in Biophysics Biozentrum, University of Basel	May 2006
PhD thesis at the Maurice Müller Institute Biozentrum, University of Basel Laboratory of Prof. Andreas Engel	Nov. 2002 - May 2006
Visiting graduate student at The Scripps Research Institute La Jolla - USA Laboratories of Profs. Ron Milligan and Geoffrey Chang	Jan. 2003 - Dec. 2003
MSc in Biology II (Structural Biology) Biozentrum, University of Basel	Oct. 2002
MSc thesis at the Maurice Müller Institute Biozentrum, University of Basel Laboratory of Prof. Andreas Engel	Sep. 2001 - Oct. 2002
Undergraduate studies in Biology II University of Basel	Oct. 1998 - Oct. 2002

Attended Courses

EMBnet course in molecular modeling — Oct. 2005
Biozentrum, University of Basel - Switzerland

Practical course in molecular microscopy — Nov. 2003
The Scripps Research Institute, La Jolla - USA

Practical course in three- dimensional cryo-electron microscopy of single particles — Aug. 2003
University of Vermont, Burlington - USA

NCCR Structural Biology course in modern protein technologies — Mar. 2002
ETH Zürich - Switzerland

Oral research presentations

3D reconstruction of membrane bound protein complexes by single particle electron microscopy — Dec. 2005
ETH Zürich - Switzerland

The proton translocation mechanism of V-ATPases — Aug. 2003
University of Vermont, Burlington - USA

Electron crystallography of V-type ATPases — Feb. 2003
The Scripps Research Institute, La Jolla - USA

Structure determination by transmission electron microscopy — Jun. 2002
University of Osnabrück - Germany

Single particle studies on the bovine V-ATPase — Mar. 2002
ETH Zürich - Switzerland

Poster presentations

Volume reconstructions of large membrane complexes from cryo-electron microscopy images — Oct. 2005
Biozentrum Symposium Basel - Switzerland

Visualizing the native state of V-type ATPases vitrified in amorphous ice — Jul. 2005
FEBS Congress and IUBMB Conference, Budapest - Hungary

Structure of a bovine V-ATPase by cryo-EM and single particle analysis — Nov. 2003
The Scripps Research Institute, La Jolla - USA

Publications

Gregorini M., Wang J., Xie X.S., Milligan R.A., Engel A. Volume reconstruction of a bovine V-ATPase imaged in native condition by cryo-electron microscopy. *JSB (2007), in press.*

Chami M., Guilvout I., **Gregorini M.**, Rémigy H.W., Müller S.A., Valerio M., Engel A., Pugsley A.P., Bayan N. Structural insights into the secretin PulD and its trypsin-resistant core. *JBC (2005), 280(45) 37732-37741.*

Front cover JBC November 11 2005 issue

Eifler N., Vetsch M., **Gregorini M.**, Ringler P., Chami M., Philippsen A., Fritz A., Müller S.A., Glockshuber R., Engel A., Grauschopf U. Structure and assembly mechanism of the pore forming toxin ClyA. *EMBO J (2006), 25(11) 2652-2661.*

Stahlberg H., Kutejova E., Muchova K., **Gregorini M.**, Lustig A., Müller S.A., Olivieri V., Engel A., Wilkinson A.J., Barak I. Oligomeric structure of the Bacillus subtilis cell division protein DivIVA determined by transmission electron microscopy. *Mol Microbiol (2004), 52(5) 1281-1290.*

Kortekaas J., Müller S.A., Ringler P., **Gregorini M.**, Weynants V.E., Rutten L., Bos M.P., Tomassen J. In vitro folding of the siderophore receptor FrpB (FetA) of Neisseria meningitidis into its oligomeric conformation. *Microbes Infec (2006), 8(8) 2145-2153.*